

1

2 μ/π separation using

3 Convolutional Neural Networks

4 for the MicroBooNE

5 Charged Current Inclusive Cross Section

6 Measurement

Jessica Nicole Esquivel

Bachelor of Science in Electrical Engineering and Applied Physics
St. Mary's University
San Antonio, TX, USA 2011

DISSERTATION

Submitted in partial fulfillment
of the requirements for the degree
Doctor of Philosophy in Physics

- * - DRAFT February 2, 2018 - * -

December, 2017
Syracuse University

19

Syracuse, New York

20

Copyright 2017

21

Jessica Nicole Esquivel

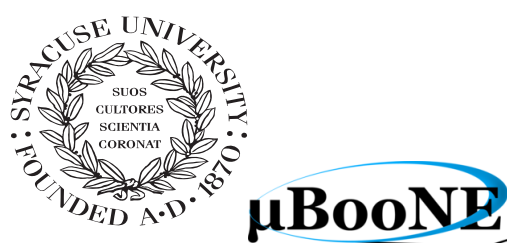
22

All Rights Reserved

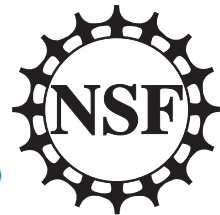
23

Syracuse University

24



μBooNE



26

Abstract

27

The purpose of this thesis was to use Convolutional Neural Networks
28 (CNN) to separate μ' s and π' s for use in increasing the acceptance rate
29 of μ' 's below the implemented 75cm track length cut in the Charged
30 Current Inclusive (CC-Inclusive) event selection for the CC-Inclusive
31 Cross-Section Measurement. In doing this, we increase acceptance
32 rate for CC-Inclusive events below a specific momentum range.

33

Dedication

34

I dedicate this dissertation to the two important women in my life; My
35 wife and my mom. Both have been there cheering me on giving me strength
36 and love as I worked towards the hardest accomplishment I've ever done.

37

Jessica Nicole Esquivel

38

Acknowledgements

39 Of the many people who deserve thanks, some are particularly prominent, such as
40 my supervisor...

Contents

41	List of figures	x
43	List of tables	xx
44	1 Introduction	1
45	2 Neutrinos	2
46	2.1 What are Neutrinos	2
47	2.2 History of Neutrinos	3
48	2.2.1 Solar Oscillations and the Solar Neutrino Problem	4
49	2.2.2 Atmospheric Oscillations and the Atmospheric Neutrino Anomaly	6
50	2.3 Neutrino Oscillations	8
51	2.3.1 Two Flavor Neutrino Oscillation Formulation	8
52	2.3.2 Three Flavor Neutrino Oscillation Formulation	11
53	2.4 Neutrino Interactions	11
54	2.4.1 Weak Interactions	11
55	2.4.2 Neutrino-Nucleon Interactions	11
56	3 The MicroBooNE Experiment	13
57	3.1 Liquid argon time projection chambers	13
58	3.2 The MicroBooNE Time Projection Chamber	14
59	3.3 MicroBooNE’s Physics Goals	16
60	3.3.1 The low-energy excess	16
61	3.3.2 Cross sections	17
62	3.3.3 Liquid argon detector development	18
63	3.4 The Booster Neutrino Beam	18
64	3.4.1 Creating the Booster Neutrino Beam	19
65	3.5 Event Reconstruction	20

66	4 Neutrino Identification: Finding MicroBooNE's first Neutrinos	23
67	4.1 Flash Finding	23
68	4.1.1 Flash Reconstruction	24
69	4.1.2 Beam Timing	25
70	4.1.3 Event Rates	26
71	4.2 TPC Topology Selection	26
72	4.2.1 Cosmic Tagging	27
73	4.2.2 2D Cluster Selection	27
74	4.2.3 3D Tracks and vertices Selection	29
75	4.2.4 TPC Updates	31
76	4.3 Conclusion	32
77	5 CC-Inclusive Cross Section Selection Filter	35
78	5.1 Data and MC Processing Chain	36
79	5.2 Normalization of data and MC	37
80	5.3 Optical Software Trigger and Reconstruction	38
81	5.3.1 Software Trigger	38
82	5.3.2 Flash Reconstruction	39
83	5.3.3 Beam Window	40
84	5.4 TPC Reconstruction	42
85	5.4.1 Hit Reconstruction	43
86	5.4.2 Clustering	43
87	5.4.3 Pandora	44
88	5.4.4 Trackkalmanhit	44
89	5.4.5 Cosmic Hit Removal	44
90	5.4.6 Projection Matching Algorithm	45
91	5.5 Event Selection	45
92	5.5.1 Expected Bakgrounds	46
93	5.5.2 Truth Distributions	49
94	6 Background on Convolutional Neural Networks	56
95	6.1 Image Classification	56
96	6.2 CNN Structure	57
97	6.2.1 Backpropagation	60
98	6.3 Choosing Hyperparameters	61

99	7 Training process of Convolutional Neural Networks	63
100	7.1 Hardware Configurations for Convolutional Neural Network Training	63
101	7.2 Creating images using LArTPC data for training/validation of CNNS	64
102	7.3 Convolutional Neural Network Training	66
103	7.3.1 Training CNN1075	66
104	7.3.2 Training CNN10000	69
105	7.3.3 Training CNN100000	72
106	8 Using Convolutional Neural Networks for ν_μ CC event classification	82
107	8.1 Classification using CNN10000	82
108	8.1.1 Classification of MC data using Selection I CC-Inclusive Filter .	82
109	8.1.2 Conclusions of CNN10000 classification of MC data	90
110	8.2 Classification using CNN100000	91
111	8.2.1 Classification of MC data using Selection I CC-Inclusive Filter .	92
112	8.2.2 Classification of MicroBooNE data using Selection I CC-Inclusive	
113	Filter	101
114	8.2.3 Comparing two CC-Inclusive Cross Section Selection Filters . .	101
115	9 Conclusion	102
116	Bibliography	103

¹¹⁷ List of figures

¹¹⁸	2.1	The Standard Solar Model [?]	4
¹¹⁹	2.2	Solar Neutrino Experiments	6
¹²⁰	2.2a	Ray Davis's Homestake Experiment [?]	6
¹²¹	2.2b	Kamiokande-II Experiment [?]	6
¹²²	2.2c	SNO Experiment [?]	6
¹²³	2.3	The flavor eigenstates are rotated by an angle θ with respect to the mass eigenstates	8
¹²⁵	3.1	Low Energy excess seen in MiniBooNE	17
¹²⁶	3.2	Arial view of the Main Injector and the Booster Neutrino Beam at Fermilab	19
¹²⁷	3.3	Arial view of the Main Injector and the Booster Neutrino Beam at Fermilab	21
¹²⁸	3.4	Energy spectrum of the Booster Neutrino Beam at Fermi National Laboratories	22
¹³⁰	4.1	Efficiency for selecting beam events as a function of minimum total PE cut for all PE cuts as well as zoomed into interesting region.	24
¹³²	4.2a	Predicted distribution of flash times with respect to trigger time for 1 day of data taking at nominal rate and intensity	29
¹³⁴	4.2b	Measured distribution of flash times with a 50 PE threshold cut, with respect to trigger time. Shown as a ratio to the expected cosmic rate from off-beam data. A clear excess from neutrinos is visible between 3- 5 μ s after the trigger time.	29

138	4.3	Percent of good clusters remaining for neutrinos and cosmics after the primary cuts were applied. This is relative to total number of initial clusters.	30
141	4.4	Percent matched cluster pairs remaining for neutrinos and cosmics after secondary cuts applied. This is relative to the number of events that contain clusters which pass the primary cuts.	30
144	4.5	First Neutrino Interaction Candidate Events from MicroBooNE	33
145	4.6	First Neutrino Interaction Candidate Events from MicroBooNE	34
146	5.1	5.1a Track range distribution for selection I. The track range is defined as the 3D distance between the start and end of the muon candidate track. No data is shown below 75 cm due to the track length cut described previously. 5.1b Efficiency of the selected events by process quasi-elastic (QE), resonant (RES), and deep-inelastic (DIS). Statistical uncertainty is shown in the bands and the distributions are a function of true muon momentum. The rise of the efficiency between 0 GeV and 0.5 GeV is due to the minimum track length cut and the decreasing efficiency for higher momentum tracks is caused by the containment requirement.	38
155	5.1a	Track range distribution of selection I	38
156	5.1b	Selection efficiency as a function of the true muon momentum	38
157	5.2	Time distribution of reconstructed optical flashes with a PE value of 50 or more for a sample of BNB unbiased triggered events.	40
159	5.3	Flash time distribution for all flashes (left plot) and flashes > 20PE (right plot). The different curves are as follows: on-beam data (black), off-beam data (red), CORSIKA inTime MC (light blue), BNB only MC (green), and BNB+Cosmic MC (purple). The dashed vertical lines mark the time window that was chosen for each sample	41
164	5.4	Reconstruction chain run on both data and MC. The red stars mean that the algorithm returns reconstructed 3D vertices.	42
166	5.5	Event selection diagram for selection I and selection II. This analysis focused on optimizing selection I. Boxes with the same color across the two selections symbolize similar cuts.	47

169	5.6 MC momentum distributions of the muon originating from a ν_μ CC interaction. Upper left is the momentum distributions of events with a vertex within the FV (green) and the events with a fully contained track (blue) before the selection. The upper right side is the momentum distribution after the selection (red). The lower plot is the selection efficiencies.	50
175	5.7 MC $\cos(\theta)$ distributions of the muon originating from a ν_μ CC interaction. Upper left is the $\cos(\theta)$ distributions of events with a vertex within the FV (green) and the events with a fully contained track (blue) before the selection. The upper right side is the $\cos(\theta)$ distribution after the selection (red). The lower plot is the selection efficiencies.	51
180	5.8 MC ϕ distributions of the muon originating from a ν_μ CC interaction. Upper left is the ϕ distributions of events with a vertex within the FV (green) and the events with a fully contained track (blue) before the selection. The upper right side is the ϕ distribution after the selection (red). The lower plot is the selection efficiencies.	52
185	5.9 MC momentum distributions of the muon originating from a ν_μ CC interaction. Upper left is the momentum distributions of events with a vertex within the FV split up into CCQE (red), CCRES (yellow), and CCDIS (green) before selection. The upper right side is the momentum distribution after the selection with the same color schemes. The lower plot is the selection efficiencies for all three interaction types. The definition of QE, RES, and DIS is based on GENIE.	53
192	5.10 MC $\cos(\theta)$ distributions of the muon originating from a ν_μ CC interaction. Upper left is the $\cos(\theta)$ distributions of events with a vertex within the FV split up into CCQE (red), CCRES (yellow), and CCDIS (green) before selection. The upper right side is the $\cos(\theta)$ distribution after the selection with the same color schemes. The lower plot is the selection efficiencies for all three interaction types. The definition of QE, RES, and DIS is based on GENIE.	54

199	5.11 MC ϕ distributions of the muon originating from a ν_μ CC interaction. Upper left is the ϕ distributions of events with a vertex within the FV split up into CCQE (red), CCRES (yellow), and CCDIS (green) before selection. The upper right side is the ϕ distribution after the selection with the same color schemes. The lower plot is the selection efficiencies for all three interaction types. The definition of QE, RES, and DIS is based on GENIE.	55
206	6.1 Pixel representation and visualization of a curve detector filter. As you can see, in the pixel representation, the weights of this filter are greater along a curve we are trying to find in the input image	58
209	6.2 Visualization of filters found in first layer of a CNN.	58
210	6.3 Applying a feature mask over a set of fashion items to extract necessary information for auto-encoding. Unnecessary information for example color or brand emblems are not saved. This feature map is an edge detec- tion mask that leaves only shape information which helps to distinguish between different types of clothes.	59
215	6.4 Pictorial Representation of Convolutional Neural Networks as well as a visual representation on CNN's complexity of layer feature extraction	59
217	6.5 Pictoral representation of the AlexNet model. The AlexNet model consists of 5 convolution layers and 3 fully connected layers.	62
219	6.6 Pictoral representation of the GoogleNet model. The GoogleNet model consists of 22 layers. The model implements 9 Inception modules which performs covolution and pooling in parallel and strays away from the basis that CNN layers need to be stacked up sequentially. The GoogleNet model also doesn't use fully connected layers, instead it uses average pooling which greatly reduces the amount of parameters. GoogleNet has 12x fewer parameters than AlexNet.	62
226	7.1 Accuracy vs. Loss of AlexNet 2-output μ/π sample consisting of 2,150 images each.	67

228	7.2 Description of confusion matrix variables: False pion rate = $false\pi/total\pi$ True pion rate = $true\pi/total\pi$ Accuracy = $(true\pi rate + true\mu rate)/2$ Pion prediction value = $true\pi/(true\pi + false\pi)$ Muon prediction value = $true\mu/(true\mu + false\mu)$	68
232	7.2a Confusion Matrix showing Accuracy of CNN1075 using training MC data	68
234	7.2b Confusion Matrix showing Accuracy of CNN1075 using testing MC data	68
236	7.3 Accuracy vs. Loss of AlexNet 2-output μ/π sample consisting of 10,000 images each.	70
238	7.4 Description of confusion matrix variables: False pion rate = $false\pi/total\pi$; True pion rate = $true\pi/total\pi$; Accuracy = $(true\pi rate + true\mu rate)/2$; Pion prediction value = $true\pi/(true\pi + false\pi)$; Muon prediction value = $true\mu/(true\mu + false\mu)$	71
242	7.4a Confusion Matrix showing Accuracy of CNN10000 using train- ing MC data	71
244	7.4b Confusion Matrix showing Accuracy of CNN10000 using testing MC data	71
246	7.5 Probability plot of muons and pions from testing set. Images surround- ing histogram are a random event from lowest bin and highest bin for each particle.	72
249	7.6 Training and testing accuracy of CNN trained on 100,000 images of $\mu/\pi/p/\gamma/e$ with 20,000 images of each particle. Each image was a size of 576x576 and the images per particle were split 90% use for training and 10% used for testing the network	73
253	7.7 Training and testing loss of CNN trained on 100,000 images of $\mu/\pi/p/\gamma/e$	73
254	7.8 Confusion Matrix of all five particles	74
255	7.9 t-SNE of CNN	75
256	7.10 Probabilities of different particle classes as well as their contamination from other classes	76

258	7.10a Muon Prob	76
259	7.10b Pion Prob	76
260	7.10c Proton Prob	76
261	7.10d Electron Prob	76
262	7.10e Gamma Prob	76
263	7.11 Muon probability of true muons (blue) versus pions (red), protons (cyan), gammas (green) and electrons (magenta).	77
265	7.12 Kinematic distributions versus muon probability for true muons and true pions.	78
267	7.12a Track range versus muon probability for true muons (blue) and true pions (red).	78
269	7.12b Track range ≤ 75 cm versus muon probability for true muons (blue) and true pions (red).	78
271	7.12c Momentum versus muon probability for true muons (blue) and true pions (red).	78
273	7.13 Kinematic distributions versus muon probability for true muons and true protons.	79
275	7.13a Track range versus muon probability for true muons (blue) and true protons (cyan).	79
277	7.13b Track range ≤ 75 cm versus muon probability for true muons (blue) and true protons (cyan).	79
279	7.13c Momentum versus muon probability for true muons (blue) and true protons (cyan).	79
281	7.14 Kinematic distributions versus muon probability for true muons and true electrons.	80
283	7.14a Track range versus muon probability for true muons (blue) and true electrons (magenta).	80

285	7.14b Track range ≤ 75 cm versus muon probability for true muons (blue) and true electrons (magenta)	80
287	7.14c Momentum versus muon probability for true muons (blue) and true electrons (magenta)	80
289	7.15 Kinematic distributions versus muon probability for true muons and true gammas.	81
291	7.15a Track range versus muon probability for true muons (blue) and true gammas (green).	81
293	7.15b Track range ≤ 75 cm versus muon probability for true muons (blue) and true gammas (green).	81
295	7.15c Momentum versus muon probability for true muons (blue) and true gammas (green).	81
297	8.1 Confusion matrix and probability plot of events passing selection I cc-inclusive cuts right before 75cm track length cut	83
299	8.1a Confusion Matrix for CNN10000 classified events from selection I	83
300	8.1b Probability plot for CNN10000 classified events from selection I	83
301	8.2 CNN10000 distributions of track candidate images output from Selection I cc-inclusive filter	84
303	8.2a Track range distribution of events from Selection I passing CNN with 70% accuracy	84
305	8.2b Stacked signal and background track range distributions from Selection I passing CNN with 70% accuracy	84
307	8.2c Stacked signal and background track range distributions from Selection I passing 75 cm track length cut	84
309	8.2d Stacked signal muons and background muons/pions of track range distributions from Selection I passing CNN with 70% accuracy	84
312	8.2e Stacked signal muons and background muons/pions of track range distributions from Selection I passing 75 cm track length cut	84

314	8.3 CNN10000 stacked signal/background track range distributions of track candidate images output from Selection I cc-inclusive filter	85
315		
316	8.3a Stacked signal muons and background muons/pions of track range distributions from Selection I passing CNN with 75% accuracy	85
317		
318		
319	8.3b Stacked signal muons and background muons/pions of track range distributions from Selection I passing CNN with 80% accuracy	85
320		
321		
322	8.3c Stacked signal muons and background muons/pions of track range distributions from Selection I passing CNN with 85% accuracy	85
323		
324		
325	8.3d Stacked signal muons and background muons/pions of track range distributions from Selection I passing CNN with 90% accuracy	85
326		
327		
328	8.4 CNN10000 momentum distributions of track candidate images output from Selection I cc-inclusive filter	86
329		
330	8.4a Momentum distribution of events from Selection I passing CNN with 70% accuracy	86
331		
332	8.4b Stacked signal and background momentum distributions from Selection I passing CNN with 70% accuracy	86
333		
334	8.4c Stacked signal and background momentum distributions from Selection I passing 75 cm track length cut	86
335		
336	8.5 Track distribution comparisons of true CC muons plotted vs true CC muons and pions plotted	88
337		
338	8.5a Stacked signal μ /background μ and π track range distribution of CNN @ 70%	88
339		
340	8.5b Stacked signal $\mu\&\pi$ /background $\mu\&\pi$ track range distribution of CNN @ 70%	88
341		
342	8.6 Images of true CC events where the pion was the tagged track candidate	88

343	8.6a	Pion reconstructed track range is less than 75 cm and longer than muon track due to dead wires	88
344			
345	8.6b	Pion reconstructed track range is less than 75 cm and larger than muon reconstructed track	88
346			
347	8.6c	Pion reconstructed track range is greater than 75 cm and larger than muon reconstructed track	88
348			
349	8.7	CNN performance of classified muons and pions compared to the already implemented 75 cm track length cut	91
350			
351	8.8	Image making steps used for classifying BNB+Cosmic events using CNN100000	92
352			
353	8.9	Efficiency vs Purity curve for various CNN100000 muon probabilities. At 85% muon probability, the efficiency is 30% and the purity is 70% .	93
354			
355	8.10	Truth kinematic distributions of events passing CNN100000 and Selection I. The red corresponds to the Selection I passing events and blue to the CNN100000 passing events.	94
356			
357			
358	8.10a	Track range distribution for events passing $\text{CNN10000} \geq 85\%$ and the Selection I filter.	94
359			
360	8.10b	$\text{Cos}(\theta)$ distribution for events passing $\text{CNN100000} \geq 85\%$ and the Selection I filter.	94
361			
362	8.10c	ϕ distribution for events passing $\text{CNN100000} \geq 85\%$ and the Selection I filter.	94
363			
364	8.10d	Momentum distribution for events passing $\text{CNN100000} \geq 85\%$ and the Selection I filter.	94
365			
366	8.11	Truth stacked event type track range distribution of events passing Selection I (left) and CNN100000 (right).	95
367			
368	8.11a	Track range distribution for events passing Selection I filter. .	95
369	8.11b	Track range distribution for events passing $\text{CNN100000} \geq 85\%$. .	95
370	8.12	Truth stacked event type momentum distribution of events passing Selection I (left) and CNN100000 (right).	95
371			

372	8.12a Momentum distribution for events passing Selection I	95
373	8.12b Momentum distribution for events passing CNN100000 $\geq 85\%$	95
374	8.13 Truth stacked event type $\cos(\theta)$ distribution of events passing Selection I (left) and CNN100000 (right).	96
375		
376	8.13a $\cos(\theta)$ distribution for events passing Selection I filter.	96
377	8.13b $\cos(\theta)$ distribution for events passing CNN100000 $\geq 85\%$	96
378	8.14 Truth stacked event type phi distribution of events passing Selection I (left) and CNN100000 (right).	96
379		
380	8.14a ϕ distribution for events passing Selection I.	96
381	8.14b ϕ distribution for events passing CNN100000 $\geq 85\%$	96
382	8.15 Vertex position for X, Y and Z of true cc-inclusive events passing CNN100000 and Selection I	97
383		
384	8.15a X Vertex Position	97
385	8.15b Y Vertex Position	97
386	8.15c Z Vertex Position	97
387	8.16 $\cos(\theta)$ distribution at CNN10000 $\geq 85\%$	98
388	8.17 $\cos(\theta)$ distribution at CNN10000 $\geq 85\%$	99
389	8.18 $\cos(\theta)$ distribution at CNN10000 $\geq 85\%$	100

³⁹⁰ List of tables

³⁹¹ 2.1	Measurements of the double ratio for various atmospheric neutrino experiments	³⁹² 7
³⁹³ 2.2	Current world knowledge of neutrino oscillation parameters [?]	³⁹³ 12
³⁹⁴ 4.1	Passing rates for 2D cluster cuts for neutrino on MC set and a cosmic only MC set. First column shows event rates with no cuts applied to both sets. Columns two and three show event rates after primary and secondary cuts are applied. Line three shows the seccond line scaled with the flash finding factor of 0.008. All events are normalized to per day assuming we are running at 5 Hz.	³⁹⁹ 29
⁴⁰⁰ 5.1	Passing rates of Selection I. Numbers are absolute event counts and cosmic background is not scaled. The BNB+Cosmic sample contains all events, not just ν_μ CC inclusive. The numbers in brackets give the passing rate wrt the step before (first percentage) and wrt total generated events (second percentage). The BNB+Cosmic MC-Truth column shows how many true ν_μ CC inclusive events are left in the sample. This number includes mis-identifications where a cosmic track is picked by the selection instead of the neutrino interaction in the same event. The cosmic only sample is used just to illustrate the cut efficiency. The last column Signal:Cosmic only gives an estimate of the ν_μ CC events wrt the cosmic only background at each step. For this number, the cosmic background has been scaled as described in section 5.2.	⁴¹¹ 48

412	5.2	Passing rates for Selection I selection applied to on-beam and off-beam 413 data. THe numbers in brackets give the passing rate wrt the step before 414 (first percentage) and wrt the generated events (second percentage). 415 Off-beam data has been scaled with a factor 1.23 to normalize to the 416 on-beam data stream.	48
417	8.1	Comparing passing rates of CNN at different probabilities versus 75 418 cm track length cut: Numbers are absolute event counts and Cosmic 419 background is not scaled appropriately. The BNB+Cosmic sample con- 420 tains all events. The numbers in brackets give the passing rate wrt 421 the step before (first percentage) and wrt the generated events (second 422 percentage). In the BNB+Cosmic MC Truth column shows how many 423 true ν_μ CC-inclusive events (in FV) are left in the sample. This number 424 includes possible mis-identifications where a cosmic track is picked by 425 the selection instead of the neutrino interaction in the same event.The 426 CNN MC True generated events were scaled wrt the MC True generated 427 events for the 75 cm cut passing rates due to only running over 188,880 428 generated events versus the 191362 generated events. The last column 429 Signal:Cosmic only gives an estimate of the ν_μ CC events wrt the cosmic 430 only background at each step. For this number, the cosmic background 431 has been scaled as described in [?]. Note that these numbers are not a 432 purity, since other backgrounds can't be determined at this step. . .	89
433	8.2	Signal and background event numbers of selection I and selection I 434 with CNN cut estimated from a BNB+Cosmic sample and Cosmic only 435 sample normalized to $5 * 10^{19}$ PoT. The last column gives the fraction 436 of this signal or background type to the total selected events per CNN 437 probability.	89

*"If they don't give you a seat at the table,
bring a folding chair."*

— Shirley Chisholm

440 **Chapter 1**

441 **Introduction**

442 This thesis will be a description of work done to further increase efficiency and purity
443 of the charged current inclusive cross section measurement using the MicroBooNE
444 detector. It will also describe the MicroBooNE detector, what neutrinos are, the
445 charged current inclusive cross section measurement and its importance as well as
446 convolutional neural networks and how they can be used in μ/π separation. Chapter
447 2 will talk about the background of neutrinos and the people and detectors that
448 discovered neutrinos as well as an in depth history of neutrino oscillation and the
449 discovery that neutrinos have mass.

450 Chapter 3 will discuss the MicroBooNE experiment, specifically, how Liquid
451 Argon Time Projection Chambers work, the Light Collection System and the Electronic
452 and Readout Trigger systems. This chapter will also describe the Booster Neutrino
453 Beam sationed at Fermilab.

454 Chapter 4 will discuss the work that was done to detect the first neutrinos seen in
455 the MicroBooNE detector and the software reconstruction efforts required to create an
456 automated neutrino ID filter that was used to find the first neutrinos and then was
457 later expanded on to create the charged current inclusive filter that will be discussed
458 in chapter 5

459 Chapter 6 will give a brief description of what Convolutional Neural Networks are
460 and how it will be used for μ/π separation in this selection. Chapter 7 will discuss
461 the hardware frameworks and training methods used to train multiple Convolutional
462 Neural Networks for use in the charged current inclusive cross section measurement.
463 Chapters 8 and ?? will discuss the results of using Convolutional Neural Networks on
464 monte-carlo and data to sift out charged current inclusive neutrino events.

⁴⁶⁵ **Chapter 2**

⁴⁶⁶ **Neutrinos**

⁴⁶⁷ **2.1 What are Neutrinos**

⁴⁶⁸ Neutrinos are fundamental particles which help make up the universe. They are also
⁴⁶⁹ one of the least understood. Neutrinos are not affected by the electromagnetic force
⁴⁷⁰ because they do not have electric charge. Neutrinos are affected by a weak sub-atomic
⁴⁷¹ force of much shorter range than electromagnetism, and are therefore able to pass
⁴⁷² through great distances in matter without much possibility of being affected by it.
⁴⁷³ Until the late 1990's, neutrinos were thought to have no mass. Neutrinos are created
⁴⁷⁴ by radioactive decay such as the ones that happen in the sun, in nuclear reactors or
⁴⁷⁵ when cosmic rays hit atoms. There are three types of neutrinos, ν_e , ν_μ and ν_τ which
⁴⁷⁶ correspond to their charged lepton pairs.

⁴⁷⁷ As previously stated, neutrinos are very weakly interacting; in fact, neutrinos can
⁴⁷⁸ pass unscathed through a wall of lead several hundred light-years thick. Because
⁴⁷⁹ neutrinos interact so rarely, studying neutrinos requires a massive detector and a
⁴⁸⁰ powerful neutrino source. With that being said, we can only "see" a neutrino when
⁴⁸¹ they interact in a detector. In a collision, distinct charged particles are produced with
⁴⁸² each type of neutrino because of the weak force. An electron neutrino will create an
⁴⁸³ electron, a muon neutrino will create a muon, and a tau neutrino will create a tau. The
⁴⁸⁴ charged lepton track the particle leaves in the detector is how one figures out what
⁴⁸⁵ type of neutrino interaction was "seen". Liquid Argon Time Projection Chambers are
⁴⁸⁶ being used to study neutrinos due to their excellent imaging and particle identification
⁴⁸⁷ capabilities.

488 2.2 History of Neutrinos

489 The neutrino was first postulated by Wolfgang Pauli in 1930 to explain how to resolve
490 the conservation of energy, momentum and angular momentum problem in beta
491 decay. Pauli suggested that this missing energy might be carried off, unseen, by a
492 neutral particle (he called neutron) which was escaping detection. James Chadwick
493 discovered a much heavier nuclear particle in 1932 that he also named neutron, leaving
494 two particles with the same name. Enrico Fermi was the first person to coin the term
495 neutrino (which means little neutral one in italian) in 1933 to fix this confusion.

496 Fermi's paper, which was published in 1934, unified Pauli's neutrino with Paul
497 Dirac's positron and Werner Heisenberg's neutron-proton model and his theory ac-
498 curately explained many experimentally observed results. Wang Ganchang first
499 proposed the use of beta capture to experimentally detect neutrinos and in 1956 Clyde
500 Cowan and Frederick Reines published their work stating that they had detected the
501 neutrino. The experiment called for antineutrinos created in a nuclear reactor by beta
502 decay that reacted with protons producing neutrons and positrons: $\nu_e + p^+ \rightarrow n^0 + e^+$.
503 Once this happens, the positron finds an electron and they annihilate each other and
504 the resulting gamma rays are detectable. The neutron is detected by neutron capture
505 and the releasing of another gamma ray.

506 In 1962 Leon M. Lenderman, Melvin Schwartz and Jack Steinberger were the first
507 to detect interactions of the muon neutrino [?]. The trio received the 1988 Nobel Prize
508 in Physics for their discovery of the muon neutrino. The experiment used a beam
509 of energetic protons from Brookhaven's Alternating Gradient Synchrotron (AGS) to
510 produce a shower of pions. These pions would then travel 70 ft. toward a 5,000
511 ton steel wall. The pions then decayed into muons and neutrinos, the neutrinos
512 being the only particle making it through. These neutrinos would enter a neon-filled
513 detector producing muon spark trails that were detected and photographed, proving
514 the existence of muon neutrinos. The experiment's use of the first ever neutrino beam
515 was pioneering work that scientists around the world still use today.

516 The first detection of the tau neutrino was announced in the summer of 2000 by
517 the DONUT collaboration at Fermilab. The scientists used the Tevatron to produce an
518 intense neutrino beam. The neutrinos then passed through layers of nuclear emulsion.
519 When a neutrino interaction would occur, charged particles would leave visible tracks
520 in the emulsion.

521 2.2.1 Solar Oscillations and the Solar Neutrino Problem

522 In the late 1960s, it was found that the number of electron neutrinos arriving from the
 523 sun was around 1/3 to 1/2 the number predicted by the Standard Solar Model. This
 524 became known as the solar neutrino problem and remained unresolved for around
 525 thirty years. This problem was resolved by the discovery of neutrino oscillation and
 526 mass. [1]

527 The standard solar model (SSM) is a mathematical model developed by John
 528 Bahcall of the sun as a spherical ball of gas with varying states of ionization. The solar
 529 neutrino flux derived from the SSM is shown in figure 2.1 [?]. Nuclear fusion and
 530 decay processes produce an abundant amount of neutrinos. The standard solar model
 531 predicts that these reactions produce several groups of neutrinos, each with differing
 532 fluxes and energy spectra. The figure also shows the ranges of detection of existing
 533 solar neutrino experiments in different shades of blue to illustrate that they sample
 534 different portions of the solar neutrino energy spectrum. Three of these experiments
 535 are discussed below.

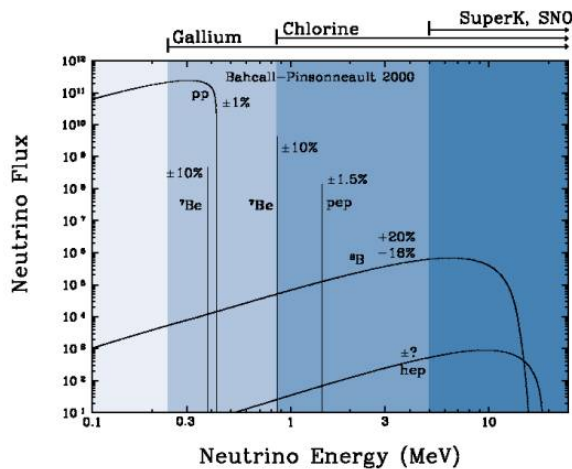
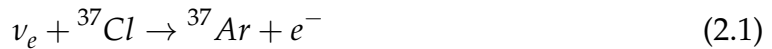


Figure 2.1: The Standard Solar Model [?]

536 The first experiment to detect the effects of neutrino oscillation was the Ray Davis's
 537 Homestake Experiment. The detector was stationed in the Homestake Gold Mine in
 538 Lead, South Dakota. It was 1,478 meters underground and was 380 m^3 . The detector
 539 was filled with perchloroethylene. Perchloroethylene was chosen because of its high
 540 concentrations of chlorine. When an ν_e interacted with a chlorine-37 atom, the atom
 541 would transform to argon-37 which was then extracted and counted. The neutrino

542 capture reaction is shown in equation 2.1. Davis observed a deficit of about 1/3
543 the flux of solar neutrinos that was predicted by Bahcall's Standard Solar Model.
544 The unexplained difference between the measured solar neutrino flux and model
545 predictions led to the Solar Neutrino Problem. [4]



546 While it is now known that the Homestake Experiment results were indicating neu-
547 trino flavor oscillation, some physicists were weary of the results. Conclusive evidence
548 of the Solar Neutrino Problem was provided by the Kamiokande-II experiment, a water
549 cherenkov detector with a low enough energy threshold to detect neutrinos through
550 neutrino-electron elastic scattering. In the elastic scattering interaction the electrons
551 coming out of the point of reaction strongly point in the direction that the neutrino
552 was traveling, away from the sun. While the neutrinos observed in Kamiokande-II
553 were clearly from the sun, there was still a discrepancy between Kamiokande-II and
554 Homestake; The Kamiokande-II experiment measured about 1/2 the predicted flux,
555 rather than the 1/3 that the Homestake Experiment saw.

556 The solution to the solar neutrino problem was finally experimentally determined
557 by the Sudbury Neutrino Observatory(SNO). The Ray Davis's Homestake Experiment
558 was only sensitive to electron neutrinos, and the Kamiokande-II Experiment was
559 dominated by the electron neutrino signal. The SNO experiment had the capability to
560 see all three neutrino flavors. Because of this, it was possible to measure the electron
561 neutrinos and total neutrino flux. The experiment demonstrated that the deficit was
562 due to the MSW effect [5], the conversion of electron neutrinos from their pure flavor
563 state into the second neutrino mass eigenstate as they passed through a resonance
564 due to the changing density of the sun. The resonance is energy dependent, and is
565 visible near 2 MeV. The water cherenkov detectors only detect neutrinos above about 5
566 MeV, while the radiochemical experiments were sensitive to lower energy (0.8 MeV for
567 chlorine, 0.2 MeV for gallium), and this turned out to be the source of the difference
568 in the observed neutrino rates at the two types of experiments. Figure 2.2 shows
569 Homestake, Kamiokande-II and SNO experiments.

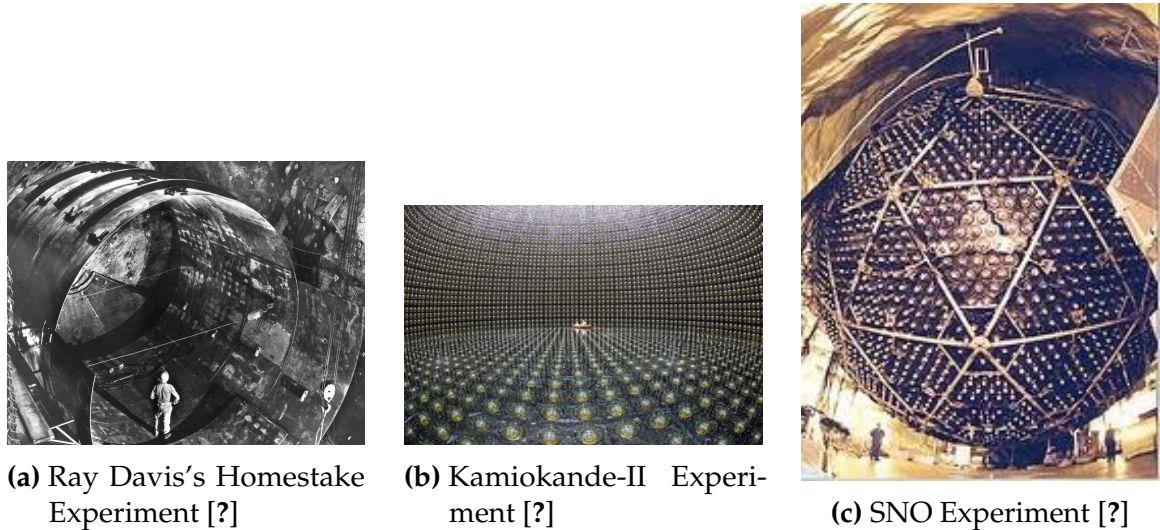


Figure 2.2: Solar Neutrino Experiments

570 2.2.2 Atmospheric Oscillations and the Atmospheric Neutrino 571 Anomaly

572 Atmospheric neutrinos are neutrinos that stem from the decay hadrons coming from
573 primary cosmic rays. The dominant part of the decay chain is shown in equations 2.2
574 and 2.3

$$\pi^+ \rightarrow \mu^+ \nu_\mu \mu^+ \rightarrow e^+ \nu_e \bar{\nu}_\mu \quad (2.2)$$

575

$$\pi^- \rightarrow \mu^- \bar{\nu}_\mu \mu^- \rightarrow e^- \bar{\nu}_e \nu_\mu \quad (2.3)$$

576 In general, these neutrinos have energies from 1 GeV to 100s of GeV and the ratio
577 of ν_μ 's to ν_e 's equals to 2 (see equation 2.4)

$$R = \frac{(\nu_\mu + \bar{\nu}_\mu)}{(\nu_e + \bar{\nu}_e)} \quad (2.4)$$

578 There have been two types of detectors used to study atmospheric neutrinos: Water
579 Cherenkov detectors and tracking calorimeters. Super-Kamiokande is the detector we
580 will focus on. These atmospheric detector experiments measure the ratio of ν_μ to ν_e .

581 They also measure the zenith angle distribution of the neutrinos. These experiments
 582 report a double ratio (shown in equation 2.5). This double ratio is the ratio measured
 583 in the detector to the ratio that's expected which is 2. If the double ratio equals to 1, the
 584 data agrees with the prediction. Various measurements from multiple experiments
 585 are shown in figure 2.1. Except for Frejus, all R measurements are less than 1. This
 586 discrepancy between the predicted R and the measured R became known as the
 587 Atmospheric Neutrino Anomaly.

$$R = \frac{(N_\mu/N_e)_{DATA}}{(N_\mu/N_e)_{SIM}} \quad (2.5)$$

Experiment	Type of experiment	R
Super-Kamiokande	Water Cherenkov	0.675 ± 0.085
Soudan2	Iron Tracking Calorimeter	0.69 ± 0.13
IMB	Water Cherenkov	0.54 ± 0.12
Kamiokande	Water Cherenkov	0.60 ± 0.07
Frejus	Iron Tracking Calorimeter	1.0 ± 0.15

Table 2.1: Measurements of the double ratio for various atmospheric neutrino experiments

588 Kamiokande-II has the capability of measuring the direction of the incoming
 589 neutrinos. The expectation of atmospheric neutrino detection is that the flux will
 590 be isotropic due to the fact that atmospheric neutrinos can reach the detector from
 591 all directions. Kamiokande-II noticed that muon-like data did not agree well with
 592 this expectation. At low energies approximately half of the ν_μ are missing over the
 593 full range of zenith angles. At high energies the number of ν_μ coming down from
 594 above the detector seems to agree with expectation, but half of the same ν_μ coming
 595 up from below the detector are missing. This anomaly can be easily explained by
 596 neutrino flavor oscillations. Due to the fact that the neutrino travels less distance
 597 coming straight down into the detector (about 15 km) than coming up from the bottom
 598 of the detector (13000 km) changes the probability of oscillation. The probability of
 599 oscillation for the muon neutrinos coming down into the detector is roughly zero,
 600 whereas for neutrinos coming up, the oscillation probability is $\sin^2(2\theta)$. Both the solar
 601 and atmospheric neutrino problems can be explained by neutrino oscillation so it's
 602 fitting to derive this phenomenon mathematically. In the next two sections, two flavor
 603 and three flavor neutrino oscillation derivations will be explained.

604 2.3 Neutrino Oscillations

605 Neutrino oscillation was first predicted by Bruno Pontecorvo. It describes the phe-
 606 nomenon of a neutrino created with a specific lepton flavor (electron, muon or tau)
 607 that is later measured to have a different flavor. Neutrino oscillation is important
 608 theoretically and experimentally due to the fact that this observation implies that the
 609 neutrino has a non-zero mass, which is not part of the original Standard Model of
 610 particle physics. [2]

611 2.3.1 Two Flavor Neutrino Oscillation Formulation

612 The flavor eigenstates can oscillate between each other because they are composed
 613 of an add mixture of mass eigenstates(ν_1, ν_2). Figure 2.3 shows the mass and flavor
 614 eigenstates rotated by an angle θ which is the mixing angle.

615 In matrix form the wavefunctions are:

$$\begin{pmatrix} \nu_\mu \\ \nu_e \end{pmatrix} = \begin{pmatrix} \cos\theta & \sin\theta \\ -\sin\theta & \cos\theta \end{pmatrix} * \begin{pmatrix} \nu_1 \\ \nu_2 \end{pmatrix} \quad (2.6)$$

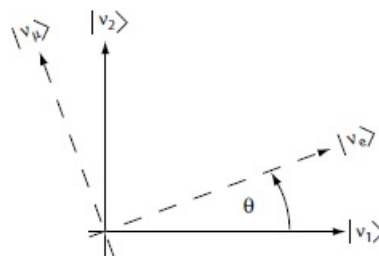


Figure 2.3: The flavor eigenstates are rotated by an angle θ with respect to the mass eigenstates

616 Applying the time evolution operator to ν_μ :

$$|\nu_\mu(t)\rangle = -\sin\theta|\nu_1\rangle e^{-i\frac{E_1 t}{\hbar}} + \cos\theta|\nu_2\rangle e^{-i\frac{E_2 t}{\hbar}} \quad (2.7)$$

₆₁₇ where $E_1 = \sqrt{p^2 c^2 + m_1^2 c^4}$ and $E_2 = \sqrt{p^2 c^2 + m_2^2 c^4}$ and $p_1 = p_2$. For the time
₆₁₈ being, let us assume $\hbar = c = 1$. With this assumption: $E_1 = \sqrt{p^2 + m_1^2}$ and $E_2 =$
₆₁₉ $\sqrt{p^2 + m_2^2}$. The next modifications is to assume neutrinos are relativistic:

$$\gamma = \frac{E}{m_o c^2} = \frac{\sqrt{p^2 c^2 + m_o^2 c^4}}{m_o c^2} \gg 1 \quad (2.8)$$

₆₂₀ because of this,

$$p \gg m_o \quad (2.9)$$

₆₂₁

$$E = \sqrt{p^2 + m_o^2} = p \sqrt{1 + m_o^2/p^2} \simeq p + \frac{1}{2} \frac{m_o^2}{p} \quad (2.10)$$

₆₂₂ where the binomial expansion is used. Now E_1 and E_2 can be written as:

$$E_1 \simeq p + \frac{1}{2} \frac{m_1^2}{p} \text{ and } E_2 \simeq p + \frac{1}{2} \frac{m_2^2}{p} \quad (2.11)$$

₆₂₃ Now applying all these assumptions back into equation 2.7 gives us:

$$|\nu_\mu(t)\rangle = -\sin\theta |\nu_1\rangle e^{-i(p+\frac{1}{2}\frac{m_1^2}{p})t} + \cos\theta |\nu_2\rangle e^{-i(p+\frac{1}{2}\frac{m_2^2}{p})t} \quad (2.12)$$

₆₂₄

$$|\nu_\mu(t)\rangle = e^{-i(p+\frac{1}{2}\frac{m_1^2-m_2^2}{p})t} (-\sin\theta |\nu_1\rangle + \cos\theta |\nu_2\rangle) \quad (2.13)$$

₆₂₅ Substituting $\Delta m^2 = m_1^2 - m_2^2$ and $t = \frac{x}{c} = x$ and $e^{-iz} = e^{-i(p+\frac{1}{2}\frac{m_1^2}{p})t}$ gives us:

$$|\nu_\mu(t)\rangle = e^{-iz} \left(-\sin\theta |\nu_1\rangle + \cos\theta |\nu_2\rangle e^{+ix(\frac{1}{2}\frac{\Delta m^2}{p})} \right) \quad (2.14)$$

₆₂₆ Finding the Probability for a $\nu_\mu \rightarrow \nu_e$:

$$P(\nu_\mu \rightarrow \nu_e) = |<\nu_e|\nu_\mu(t)>|^2 \quad (2.15)$$

⁶²⁷ Remembering that $\langle \nu_i | \nu_j \rangle = \delta_{ij}$

$$\langle \nu_e | \nu_\mu(t) \rangle = e^{-iz} \left(-\sin\theta \cos\theta + \sin\theta \cos\theta e^{\frac{i\Delta m^2 x}{p}} \right) \quad (2.16)$$

⁶²⁸ Taking the absolute value squared gives us:

$$P(\nu_\mu \rightarrow \nu_e) = |\langle \nu_e | \nu_\mu(t) \rangle|^2 = e^{+iz} e^{-iz} \sin^2\theta \cos^2\theta \left(-1 + e^{\frac{i\Delta m^2 x}{p}} \right) \left(-1 + e^{-\frac{i\Delta m^2 x}{p}} \right) \quad (2.17)$$

⁶²⁹ Since the neutrino is relativistic we can set $p = E_\nu$ and change $x = L$. Also
⁶³⁰ recognizing the trigonometric relation $(1 - \cos 2\theta)/2 = \sin^2\theta$ the above equation
⁶³¹ becomes:

$$P(\nu_\mu \rightarrow \nu_e) = \sin^2 2\theta \sin^2 \left(\frac{\Delta m^2 L}{4E_\nu} \right) \quad (2.18)$$

⁶³² All that's left to do now is re-introduce \hbar and c doing this we get:

$$P_{\nu_\mu \rightarrow \nu_e}(L, E) = \sin^2 2\theta \sin^2 \left(1.27 \Delta m^2 \frac{L}{E_\nu} \right) \quad (2.19)$$

⁶³³ This equations has three important variables.

- ⁶³⁴ • The angle θ : This angle, as mentioned before, is called the mixing angle. It defines
⁶³⁵ the difference between the flavor and the mass eigenstates. When $\theta = 0$ the mass
⁶³⁶ and flavor eigenstates are identical and no oscillations occur.
- ⁶³⁷ • The mass squared difference, Δm^2 : Again $\Delta m^2 = m_1^2 - m_2^2$. The reason this is an
⁶³⁸ important variable is because it implies that for neutrinos to oscillate, neutrinos
⁶³⁹ must have mass. Furthermore, the mass squared difference also tells us that the
⁶⁴⁰ neutrino mass eigenstates must be different.
- ⁶⁴¹ • L/E: This is the variable that is of most interest to experimental physicists due to
⁶⁴² the fact that it is the variable that we set. L is the distance between the source and
⁶⁴³ detector and E is the energy of the neutrino. For a given Δm^2 , the probability of
⁶⁴⁴ oscillation changes with respect to L/E.

645 2.3.2 Three Flavor Neutrino Oscillation Formulation

646 Seeing the quantum mechanics involved in deriving the probability of a two flavor
 647 neutrino oscillation, it is now possible to formulate the three flavor neutrino oscillation.
 648 The three flavor neutrino oscillation formulation begins similarly to the two flavor,
 649 but there is the Pontecorvo-Maki-Nakagawa-Sakata matrix (PMNS) instead of the 2X2
 650 matrix in the previous section. The PMNS matrix is show below:

$$\begin{pmatrix} c_{12}c_{13} & s_{12}c_{13} & s_{13}e^{-i\delta} \\ -s_{12}c_{23} - c_{12}s_{23}s_{13}e^{i\delta} & c_{12}c_{23} - s_{12}s_{23}s_{13}e^{i\delta} & s_{23}c_{13} \\ s_{12}s_{23} - c_{12}c_{23}s_{13}e^{i\delta} & -c_{12}s_{23} - s_{12}c_{23}s_{13}e^{i\delta} & c_{23}c_{13} \end{pmatrix} * \begin{pmatrix} e^{i\alpha_1/2} & 0 & 0 \\ 0 & e^{i\alpha_2/2} & 0 \\ 0 & 0 & 1 \end{pmatrix} \quad (2.20)$$

651 where $c_{ij} = \cos\theta_{ij}$ and $s_{ij} = \sin\theta_{ij}$

652 Following the same steps as before we get:

$$P_{\alpha \rightarrow \beta} = \delta_{\alpha\beta} - 4\sum Re(U_{\alpha i}^* U_{\beta i} U_{\alpha j} U_{\beta j}^*) \sin^2\left(\frac{\Delta m_{ij}^2 L}{4E}\right) 2\sum Im(U_{\alpha i}^* U_{\beta i} U_{\alpha j} U_{\beta j}^*) \sin\left(\frac{\Delta m_{ij}^2 L}{2E}\right) \quad (2.21)$$

653 The main things to notice here are δ_{ij} which is the CP violating term and has not
 654 been measured yet, and θ_{13} which has just been measured. CP violation is a violation
 655 of the postulated CP-symmetry. CP-symmetry states that the laws of physics should
 656 be the same if a particle were to be exchanged with its antiparticle and then if the left
 657 hand side of a decay were switched with the right hand side. Table 2.2 shows the
 658 current world knowledge of the values of all the fundamental parameters for neutrino
 659 oscillations [?].

660 2.4 Neutrino Interactions

661 2.4.1 Weak Interactions

662 2.4.2 Neutrino-Nucleon Interactions

Parameter	Value
θ_{12}	$33.9 \pm 1.0^\circ$
θ_{23}	$39^\circ < \theta_{23} < 51^\circ$
θ_{13}	$9.1 \pm 0.6^\circ$
Δm_{21}^2	$(7.50 \pm 0.20) * 10^{-5} \text{ eV}^2$
$ \Delta m_{32}^2 $	$(2.32^{+0.12}_{-0.08}) * 10^{-3} \text{ eV}^2$
δ_{cp}	unknown

Table 2.2: Current world knowledge of neutrino oscillation parameters [?]

663 **Chapter 3**

664 **The MicroBooNE Experiment**

665 The purpose of this chapter is to discuss and understand the details of the MicroBooNE
666 detector. A thorough understanding of MicroBooNE and the technology behind liquid
667 argon time projection chambers is important for understanding results as well as
668 understanding how images were made for use in deep learning efforts that will be
669 outlined in later chapters.

670 **3.1 Liquid argon time projection chambers**

671 Liquid Argon Time Projection Chambers (LArTPCs) are an exciting detector technol-
672 ogy that provide excellent imaging and particle identification, and are now being
673 used to study neutrinos. The Time Projection Chamber (TPC) was first invented by
674 Nygren in 1974 [?] and the proposal for a LArTPC for neutrino physics was made
675 by Rubbia [?] in 1977 with the ICARUS collaboration implementing this concept [?].
676 A LArTPC is a three-dimensional imaging detector that uses planes of wires at the
677 edge of an active volume to read out an interaction. When a neutrino interacts with an
678 argon atom, the charged particles that are produced ionize the LAr as they travel away
679 from the interaction. By placing a uniform electric field throughout the LAr volume,
680 the ionization is made to drift towards a set of anode planes, which consist of wires
681 spaced very closely together collecting the ionized charge, which is subsequently read
682 out by electronics connected to the anode wires. The collected ionization creates a
683 spatial image of what happened in the detector on each anode plane. The position
684 resolution of the interaction along the beam direction (perpendicular to drift direction)
685 relies on the wire pitch, while the resolution in drift direction is dependent on the

686 timing resolution of the electronics used and the longitudinal diffusion in the volume.
687 The drift time of the ionization relative to the time of the original signal allows the
688 signal to be projected back along the drift coordinate, hence the name LArTPC. Having
689 very small distances between each wire within an anode plane allows for very fine
690 granularity and detail to be captured, and having multiple wire planes at different
691 angles provides independent two-dimensional views that can be combined into a
692 three dimensional picture of the interaction. Once the charge signal is created on the
693 anode planes, software analysis packages identify particles in the detector by using
694 deposited energy on the wires along their track length. The 30 year development of the
695 ICARUS detector has led to LArTPCs being used as cosmic ray [?], solar neutrino [?]
696 and accelerator neutrino [?] detectors. The ArgoNeuT experiment at Fermilab was
697 the first United States based liquid argon neutrino program that has since produced
698 short-baseline $\nu - Ar$ cross-section measurements in the NUMI beamline [?]. The
699 MicroBooNE experiment is the second experiment in the US based LArTPC neutrino
700 program and will be discussed thoroughly in the next sections. The next phases of
701 the liquid argon neutrino program are under way and are the Fermilab Short Base-
702 line Neutrino (SBN) program [?] and the Deep Underground Neutrino Experiment
703 (DUNE) [6]. The SBN program will include three LArTPC detectors, including the
704 MicroBooNE detector, on the Booster Neutrino Beam (BNB) to do multiple-baseline
705 oscillation measurements. The detector closest to the beam will be the 40 ton Short
706 Baseline Neutrino Detector (SBND) [?] at 150 m and the detector furthest is the 600 ton
707 ICARUS T600 [?] detector positioned at 600 m. The DUNE collaboration will deliver
708 a 30 GeV neutrino beam 1300 km from Fermilab to a 34 kiloton LArTPC detector
709 at Homestake, SD. DUNE will study the leptonic CP phase, δ_{cp} , as well as measure
710 neutrino and antineutrino oscillations.

711 3.2 The MicroBooNE Time Projection Chamber

712 MicroBooNE (Micro Booster Neutrino Experiment) is a 89 ton active volume (180 ton
713 total mass) LArTPC which is then inserted into a cylindrical cryostat on axis of the
714 Booster Neutrino Beam (BNB) stationed at Fermilab in Batavia, Illinois. Understanding
715 LArTPC technology and detector physics is necessary to build a LArTPC the size of
716 DUNE, and MicroBooNE has made many advances in developing this technology [7]
717 [8].

MicroBooNE's Time Projection Chamber (TPC) is 10.3 m long (beamline direction), 2.3 m high and 2.5 m wide (which corresponds to the drift distance). The TPC is shown in figure ?? . MicroBooNE is the largest LArTPC currently running in the world [9]. This LArTPC has 3 wire planes: 1 plane that collects the ionization in the wires and is 0° to the vertical with 3456 wires spaced 3 mm apart, and 2 planes where the ionization drifts passed and induces a signal at $\pm 60^\circ$ to the vertical each with 2400 wires also spaced 3 mm apart. Each plane has a spacing also of 3 mm from eachother. The first two planes are the induction planes and the last is the collection. The 270 V/cm electric field of the TPC is created using 64 stainless steel tubes shaped into rectangles around the TPC and held in place by G10 to form a field cage. The cathode is charged at a high voltage of -70 kV and this voltage is stepped down across the field cage tubes using a voltage divider chain with an equivalent resistance of $240 \text{ M}\Omega$ between the tubes. The field cage tubes are separated by 4 cm from center to center. The electron drift distance is 2.5 m in the x direction with a drift time of 2.3 ms. Maintaining high charge yield is done by continuously recirculating and purifying the argon. The purity is monitored using MicroBooNE's light collection system. Another use of the light collection system is initial timing and drift coordinate of the interaction.

MicroBooNE's light collection system is a crucial part for 3D reconstruction of all particle interactions in the LArTPC. The initial interaction time, t_0 , and initial drift coordinate, x_0 , are not known from the TPC alone. For beam events, the accelerator clock is used to determine t_0 of the interaction and the x_0 can be inferred using drift time. Non-beam events, however, do not have this capability, which is why scintillation light from an interaction is used. The $\nu - Ar$ interaction produces scintillation light which is collected by photomultiplier tubes (PMTs) which allows the exact time, t_0 of the neutrino interaction to be determined. The scintillation light created propagates within nanoseconds to the light collection system compared to the milliseconds it takes the ionized electrons from the interaction to reach the anode wire planes. Therefore we can precisely know where along the drift direction the particle interaction first took place. The scintillation light is also localized, so combining the PMT information with the wire plane information allows for cosmic background rejection happening outside the beam timing window.

The light collection system is made up of 32 Hamamatsu R5912-02mod cryogenic PMTs with a diameter of 8-inches. The PMTs are located behind the 3 wire anode planes and provides 0.85% photocathode coverage. Each PMT has an acrylic plate mounted in front of it that is coated with a wave-length shifting material called TPB.

753 The acrylic plates take in the scintillation light, at 128 nm, and re-emits it visible
754 wavelengths visible to the PMTs, with a peak at 425 nm.

755 Both the light collection system and the TPC create analog signal that is read out and
756 digitized by the electronics system. The process requires amplification and shaping of
757 the signal which then goes to the data acquisition (DAQ) software for writing of the
758 digitized data to disk. The anode plane wires are connected to detector specific circuit
759 boards (ASICS) that are submerged and operate inside the liquid argon volume. These
760 ASICS send amplified signal to 11 feed-throughs where further amplification of the
761 signal happens outside the cryostat. The signal is received by custom LArTPC readout
762 modules distributed over nine readout crates which do the digitization. The TPC wires
763 are digitized at 16 MHz then downsampled to 2 MHz. The TPC system reads out 4
764 frames of wire signal data per event, 1 frame before a trigger and 2 frames after the
765 triggered frame. The four frames allows for identification of a neutrino interaction as
766 well as cosmic background rejection. The process of digitization is similar for the light
767 collection system. Each PMT signal undergoes a shaping with a 60 ns peaking time
768 for digitization of multiple samples. The digitization occurs at 64 MHz but are not
769 read out continuously during the TPC readout time. Only shaped PMT signal samples
770 above a small threshold are read out and saved. Both the TPC and PMT readouts are
771 initiated via triggers on a separate trigger board located in a warm electronics crate.
772 The timing trigger is created by a timing signal from the BNB accelerator which is
773 shaped and sent to the trigger board. The PMT trigger is generated when the PMT
774 signal multiplicity is greater than 1 and the summed PMT pulse-height is more than 2
775 photo-electrons summed up over all PMT channels. When the trigger board gets both
776 a timing trigger and a PMT trigger in coincidence, at BNB trigger is then generated by
777 the board. This signal is then passed to all readout crates initiating the readout of data.
778 The data is then sent to the DAQ software which then saves the data to disk into one
779 event memory.

780 3.3 MicroBooNE's Physics Goals

781 3.3.1 The low-energy excess

782 The primary goal of the MicroBooNE experiment is to study and investigate the low-
783 energy excess seen in MiniBooNE 3.1. MicroBooNE has the capability of confirming or

denying this excess as electrons or photons due to the detector being in the same beam, having a similar baseline, and lastly the detector being able to clearly distinguish between electrons and photons. LArTPCs use the topology of events as well as energy loss near the vertex to differentiate between single e^- tracks and photon-induced induced pair production $\gamma \rightarrow e^+ e^-$, which wasn't possible in MiniBooNE, a Cherenkov detector. This technique has been shown in the ArogoNeuT detector [?] and a side by side comparison of both event types in a LArTPC can be seen in figure ?? . An excess in electrons would point towards new oscillation physics beyond the standard model, while photons would be within the standard model. MicroBooNE will observe a $4-5\sigma$ signal.

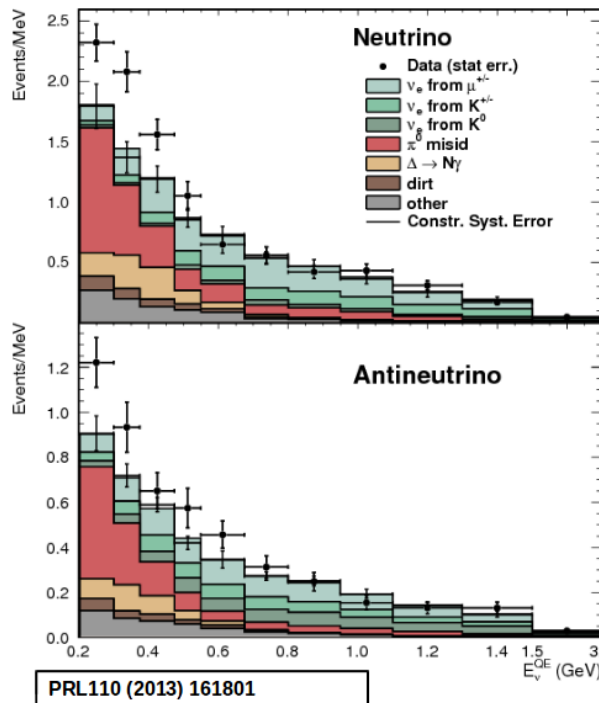


Figure 3.1: Low Energy excess seen in MiniBooNE

3.3.2 Cross sections

MicroBooNE's neutrino cross-section program will be the first $\nu - Ar$ cross-section in the 1 GeV energy range and one of only a few cross-section measurements of $\nu - Ar$ in the world. MicroBooNE is also the first liquid argon detector to collect the highest statistics sample of neutrino interactions. Investigating final-state-interactions in the 1GeV energy range provides information about short range nuclear correlations that affect the interpretations of neutrino oscillation experiment data.

One of the cross-section measurements MicroBooNE can make is an inclusive charged-current cross-section measurement (referred to as CC-inclusive). CC-inclusive events consist of a neutrino exchanging a W^\pm boson with an argon atom, producing a charged lepton and any number of other final state particles. In MicroBooNE's case, a CC-inclusive event will mostly have a defining muon track coming out of the vertex due to our neutrinos being predominately ν_μ s. A cross-section measurement is the energy dependent probability of $\nu - Ar$ interaction in the detector. Cross-sections however are independent of the intensity or focus of the particle beam so they can be compared among different experiments. A background for a CC-inclusive cross-section measurement are the neutral-current events that contain a pion. It is possible to have a neutral current interaction with a $\pi + p$ event signature that looks like a charged current $\mu + p$ event. Reconstruction tools implemented to date don't efficiently separate muons from pions. A common way to separate these two particles species is to implement a track length cut. On average, muons tend to have longer track lengths in LArTPCs so by requiring that the hypothesized lepton be above a threshold track length, it is possible to increase signal to background.

3.3.3 Liquid argon detector development

The last physics goal for the MicroBooNE collaboration is to provide important information regarding LArTPC technology. Being the first in large scare LArTPCs in the US, MicroBooNE will be able to provide improvements to High Voltage (HV) distribution, Noise Characterization [?], and Michel Electron Reconstruction [8].

3.4 The Booster Neutrino Beam

The MicroBooNE detector is stationed at Fermi National Accelerator Laboratory (FNAL) where it receives neutrinos from both the Booster Neutrino Beam (BNB) and Neutrinos from the Main Injector (NuMI) beams. MicroBooNE is on-axis for the BNB and off-axis by 135 mrad for NuMI. For the purpose of this analysis, only data from the BNB was used. This section will discuss how neutrinos are created using the BNB. How these neutrinos are produced as well as their flux through the MicroBooNE detector is necessary for any analysis because of the systematic uncertainties the beam

⁸³⁰ introduces to a measurement. An aerial view of fermilab as well as the BNB is shown
⁸³¹ in figure 3.2

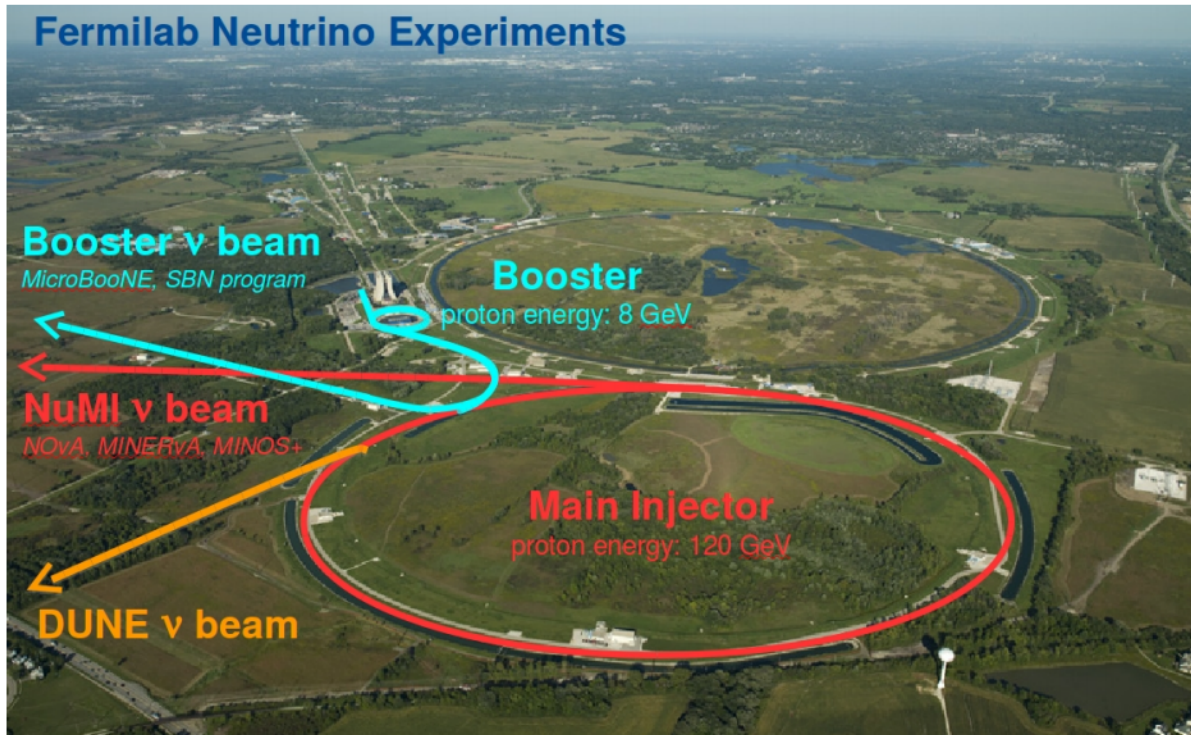


Figure 3.2: Arial view of the Main Injector and the Booster Neutrino Beam at Fermilab

⁸³² 3.4.1 Creating the Booster Neutrino Beam

⁸³³ The BNB is a very pure ν_μ beam, with only 0.6% contamination from ν_e s. The energy
⁸³⁴ also peaks around 700 MeV which is desired based on the probability of oscillation
⁸³⁵ equation which depends on the the value of L/E , where L is the distance of the
⁸³⁶ detector from the neutrino beam and E is the energy of the neutrino beam. L/E was
⁸³⁷ chosen to increase the probability of seeing neutrino oscillations in the MiniBooNE
⁸³⁸ Low Energy Excess (LEE) range based on the probability of oscillation equation, which
⁸³⁹ is $P_{\nu_\mu \rightarrow \nu_e}(L, E) = \sin^2 2\theta \sin^2 \left(1.27 \Delta m^2 \frac{L}{E} \right)$. The BNB collides 8.9 GeV/c momentum
⁸⁴⁰ protons from the FNAL booster synchrotron into a beryllium target which produces a
⁸⁴¹ high flux of neutrinos. The protons originate from H^2 gas molecules that are turned
⁸⁴² into H^- ions by a Cockcroft-Walton generator shown in figure ???. The H^- initially are
⁸⁴³ accelerated to 1MeV kinetic energy and are then passed to a linear accelerator using
⁸⁴⁴ alternating electromagnetic fields to increase their energy to 400MeV. The ions are
⁸⁴⁵ stripped of electrons by passing them through a carbon foil. The protons are bunched

846 into beam spills which contain $4 * 10^{12}$ protons in a $1.6 \mu\text{s}$ time window per spill. It's
847 at this point that the protons are directed towards the beryllium target. The amount
848 of protons directed towards the target (POT) is measured by two toroids upstream of
849 the target with an error of 2%. Beam intensity, timing, width, position, and direction
850 are monitored by beam position monitors, multi-wire chamber and resistive monitors.
851 The beryllium target is 71.1 cm long, 1.7 proton interaction lengths, and is 0.51 cm in
852 radius. The target is located inside a larger focusing electromagnet called the horn.
853 The horn is an aluminum alloy pulsed toroidal electromagnet. The pulsed current
854 peaks at 170 kA with a time-width of $143 \mu\text{s}$ which coincides with the protons arriving
855 on the target. The current flows from the inner conductor to the outer conductor
856 with a maximum magnetic field of 1.5 Tesla. The magnetic field focuses the charged
857 secondary particles produced by the p-Be interactions. The direction of current can be
858 switched to change the polarity of the secondary particles being focused creating a
859 beam of either primarily neutrinos, with positively charged secondary particles, or
860 antineutrinos.

861 Further down the beamline is a concrete collimator which absorbs particles not
862 necessary to the neutrino flux. The collimator is 214 cm long and 30 cm in radius.
863 After the collimator comes a 45 meter long, 1 meter radius, air-filled cylindrical decay
864 region which then ends in a beam-stop made of steel and concrete. The beam-stop
865 contains an array of gas proportional counters to detect muons. The BNB is shown in
866 figure 3.3.

867 **3.5 Event Reconstruction**

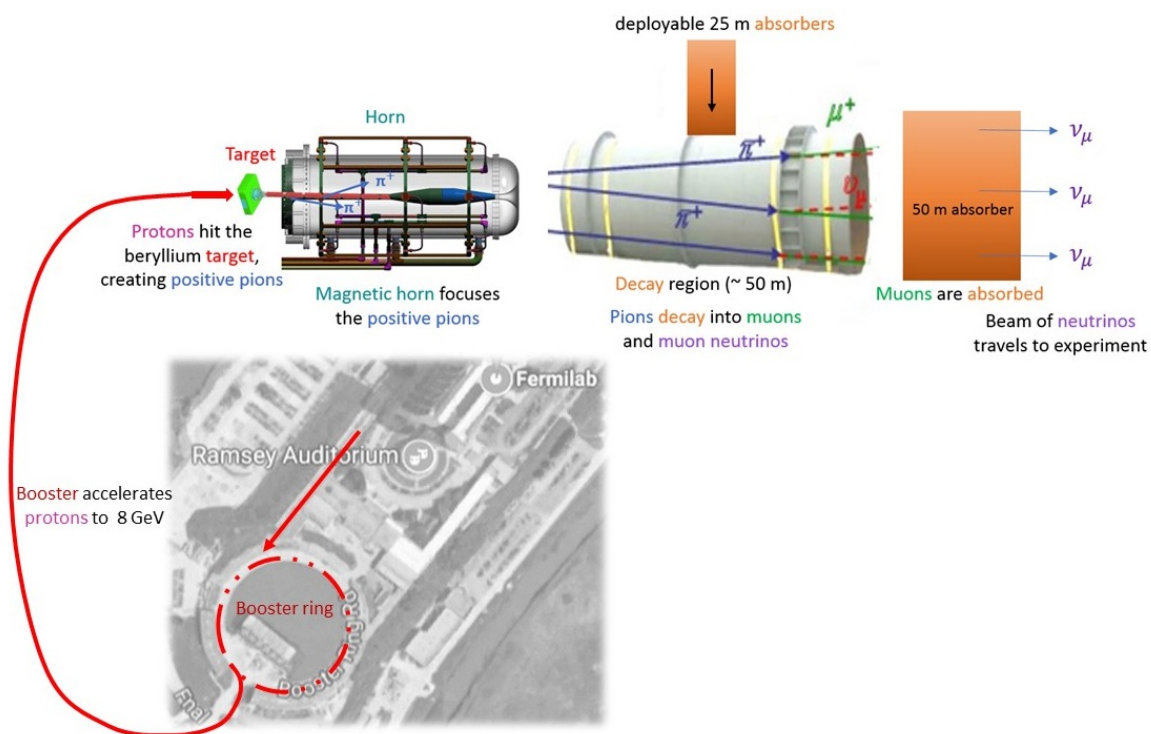


Figure 3.3: Aerial view of the Main Injector and the Booster Neutrino Beam at Fermilab

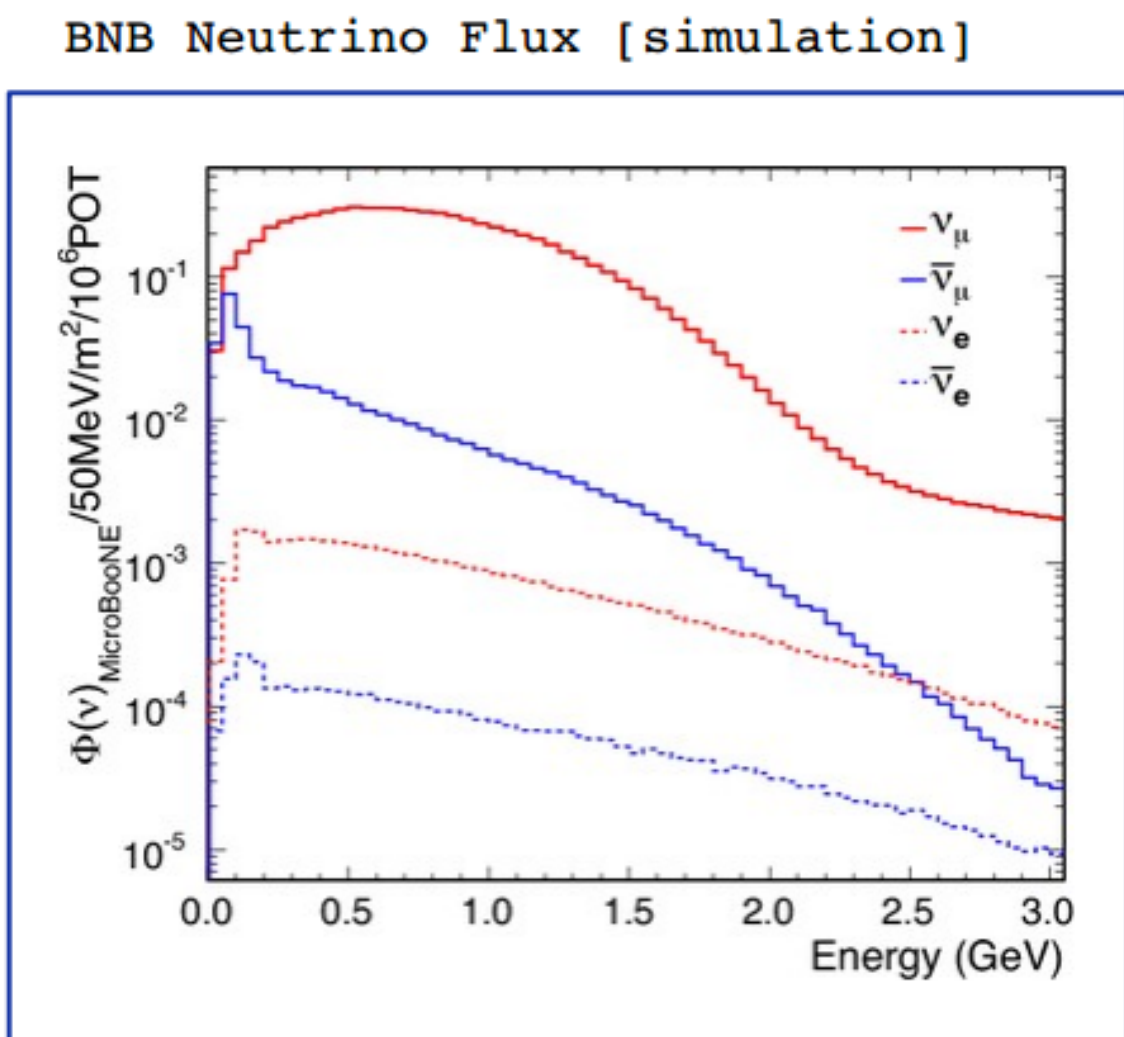


Figure 3.4: Energy spectrum of the Booster Neutrino Beam at Fermi National Laboratories

868 Chapter 4

869 Neutrino Identification: Finding 870 MicroBooNE's first Neutrinos

871 The goal of the Neutrino Identification analysis was to positively identify BNB neutrino
872 interactions in the MicroBooNE detector collected during the first days of running.
873 Neutrino event candidates were identified in part by using a cut on detected flash of
874 scintillation light during the $1.6 \mu\text{s}$ beam-spill length of the BNB as well as identifying
875 reconstructed object from the TPC that are neutrino like. After this selection, 2D
876 and 3D event displays were used for verification of the selection performance. This
877 selection was targeted to reduce the ratio of neutrino events to cosmic-only events from
878 the initial 1 neutrino to 675 cosmics to a ratio of 1 to 0.5 or better which is equivalent to
879 a background reduction by a factor of 1000 or more. These selected events were used
880 for MicroBooNE's public displays of neutrino interactions. A clearly visible neutrino
881 interaction with an identifiable vertex and at least 2 tracks originating from the vertex
882 was what the analysis focused on. This analysis wasn't optimized for high purity
883 or efficiency, but rather for very distinguishable neutrino interactions that could be
884 identified by the public.

885 4.1 Flash Finding

886 Flash finding is the first step used in finding neutrino interactions. This section will
887 detail how optical information is reconstructed as well as analysis scripts and event
888 filters were used.

889 **4.1.1 Flash Reconstruction**

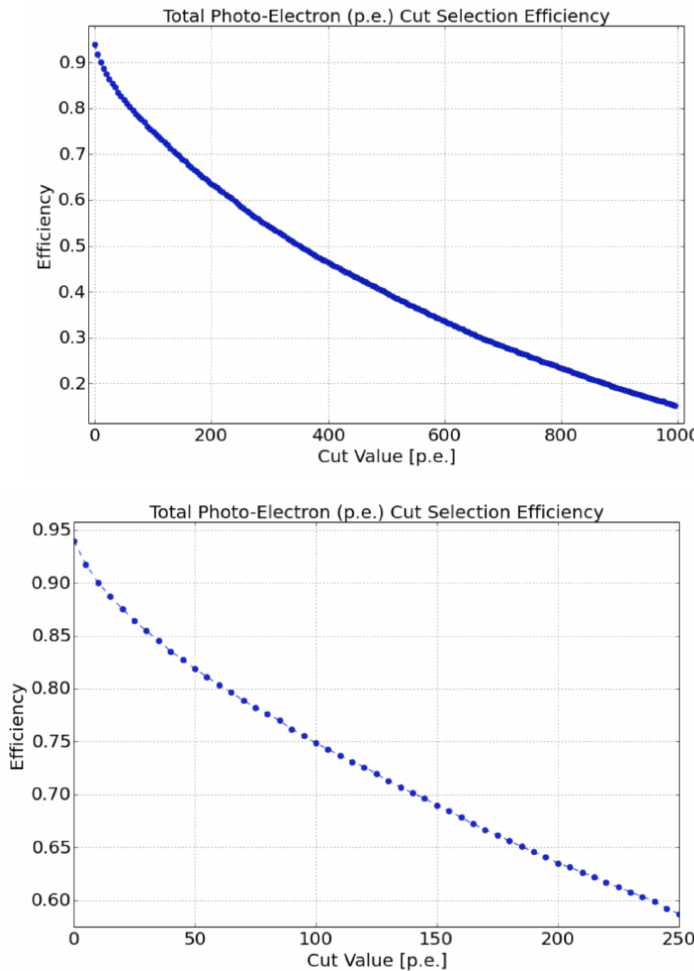
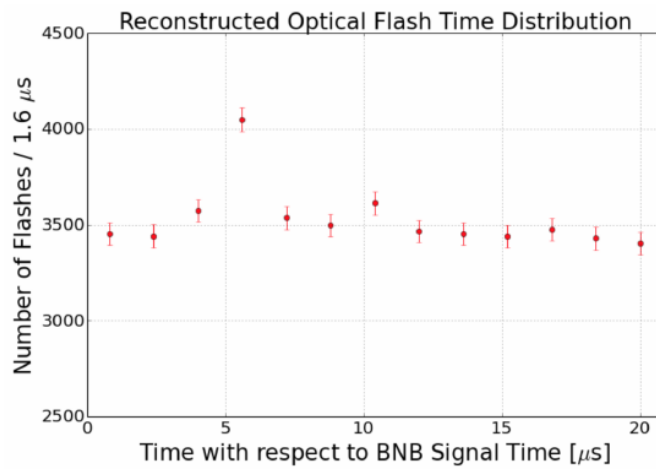


Figure 4.1: Efficiency for selecting beam events as a function of minimum total PE cut for all PE cuts as well as zoomed into interesting region.

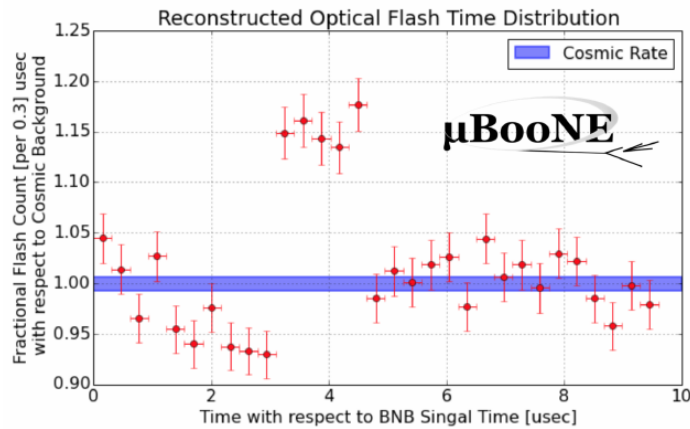
890 A flash is described as a collection of light seen at the same time within the detector.
891 They are then reconstructed by identifying signal from the PMTs above a specific
892 photoelectron (PE) threshold. These signals are called optical hits. Optical hits from
893 all the PMTs are then accumulated into $1\text{ }\mu\text{s}$ bins of time. If a specific bin is above a
894 set PE threshold, then the optical hits that overlap in time are the labeled as the hits
895 from the flash. All flash reconstructed properties like average time and x/y positions
896 are then found via the flash labeled optical hits. The total size of the flash is found by
897 summing up the total number of photoelectrons from all PMTs. Neutrino interactions
898 and cosmic muons will have a larger flash size compared to noise and other low-energy
899 backgrounds, therefore a total PE cut is used to reject these backgrounds. A total PE

⁹⁰⁰ cut of 50 PE was deemed sufficient for this analysis. Figure 4.1 show the total PE
⁹⁰¹ versus the selection efficency of selecting neutrino beam events.

⁹⁰² **4.1.2 Beam Timing**



(a) Predicted distribution of flash times with respect to trigger time for 1 day of data taking at nominal rate and intensity



(b) Measured distribution of flash times with a 50 PE threshold cut, with respect to trigger time. Shown as a ratio to the expected cosmic rate from off-beam data. A clear excess from neutrinos is visible between 3- 5 μ s after the trigger time.

⁹⁰³ It is necessary to get the specific time from flashes if one uses flashes to filter out
⁹⁰⁴ neutrino interactions coincident with the neutrino beam spill period and background.
⁹⁰⁵ Before a filter can be applied, an understanding of the timing of the trigger and PMT

906 readout with respect to the arrival of neutrinos from the BNB. To do this, a $1.6 \mu\text{s}$
 907 window near the expected beamtime was created and verified by finding that the
 908 number of flashes was significantly above the cosmic-ray background flashes. Beam
 909 data during the first week of running, October 16th 2016 through October 22nd 2016
 910 and were used for a timing measurement. The total POT uses corresponds to roughly
 911 24 hours of data taking at nominal intensity ($4 \times 10^{12} \text{ ppp}$) and a 5 Hz repetition rate.
 912 Figure 4.2a shows size of the expected neutrino signal in time using Monte Carlo
 913 predictions and figure 4.2b shows the neutrino signal in data. The intensity in data is
 914 lower, however there can still be seen a significant excess above data.

915 **4.1.3 Event Rates**

916 Applying a 50 PE threshold cut inside a $1.6 \mu\text{s}$ window reduces the cosmic-ray passing
 917 rate to 0.8%. With a 5 Hz beam rate, this corresponds to 135 cosmics passing per
 918 hour. The neutrino passing rate for this filter is about 22 events per hour. To further
 919 increase the neutrino to cosmic ratio, TPC topology cuts were implemented and will
 920 be discussed in the following section.

921 **4.2 TPC Topology Selection**

922 In order to further reduce the background of cosmic events, two independent selection
 923 streams using TPC wire data reconstruction was implemented. The first using 2D
 924 reconstructed clusters, and the second using 3D reconstructed tracks. Both streams
 925 look for neutrino interactions in the active TPC volume which are identifiable by two
 926 or more tracks originating from the same vertex.

927 Both 2D and 3D channels were optimized using monte carlo simulation which
 928 used a 128 kV cathode voltage. Passing rates were calculated using a 0.008 efficiency
 929 factor for cosmic events passing to simulate the flash finding described in section 4.1.
 930 This efficiency factor was an overestimation and was just used to get a general feel of
 931 what signal and background rates we would actually see in data.

932 **4.2.1 Cosmic Tagging**

933 The first step in TPC selection was based on the geometry of cosmic tracks in an event.
934 The cosmic ray muon geometry tagger runs on 3D tracks and assigns a score to each
935 reconstructed track on the likeliness of the track originating from a cosmic. The cosmic
936 scores are detailed below:

- 937 • 1: The track is tagged as entering or exiting the TPC
- 938 • 0.95: The track is a delta ray associated with a tagged track
- 939 • 0.5: The track is either entering or exiting, but not both
- 940 • 0.4: The track is entering or exiting through the Z boundary
- 941 • 0: The track isn't tagged

942 Clusters are assigned either a 0 or 1, 1 being a cosmic. In simulation, 90% of cosmics
943 are tagged as cosmics. These tracks are no longer considered when looking for a
944 neutrino topology. Requiring that the tracks be contained in turn affects the neutrino
945 efficiency by 20%. The algorithm checks that each track is contained within a boundary
946 region of 10 cm from all sides of the TPC. This boundary region was optimized via
947 handscanning of experimental data.

948 As can be expected, cosmic tagging is more efficient in the 3D channel (tracks) than
949 the 2D channel (clusters) because the reconstructed tracks can use the full 3D position
950 information of the entering and exiting points while the 2D channel mainly use the
951 reconstructed x position of the cluster which is associated to timing.

952 Cosmic tagging uses timing information to reject tracks and clusters that are outside
953 of drift window. The drift window for 128 kV is $1.6 \mu\text{s}$ while for 70 kV, the actual
954 voltage MicroBooNE is running at, is $2.3 \mu\text{s}$. Due to this variation between simulation
955 and data, we expect to see $2.3/1.6 = 1.44$ times more cosmic induced tracks or clusters
956 in the drift window.

957 **4.2.2 2D Cluster Selection**

958 This selection was spearheaded by myself and Katherine Woodruff. After looking at
959 experimental cosmics data, 2D clustering performs well, while 3D track reconstruction
960 is affected by more variations in simulation, for example noise filters. This was the

961 motivation for having a selection only on 2D clusters in the collection (Y) plane. As
 962 stated previously, the goal of this analysis was to find identifiable neutrino interactions
 963 for use in public event displays, in future analyses, the 3D track reconstruction has
 964 been modified to further increase the tracking efficiency and has more information
 965 than just the clusters. For this analysis, however, 2D cluster information was sufficient
 966 enough for neutrino selection.

967 **Primary Cuts**

968 The first cuts were used to select which clusters to consider. First the clusters must
 969 have at least ten hits on the collection plane and have a cosmic tagging score < 0.4.
 970 Only events that have at least two clusters that satisfy these primary cuts continue on.

971 After the initial cosmic tagging is applied, the following cuts are used to further
 972 separate identifiable neutrinos from background cosmics.

973 The next cut was to remove long, vertical clusters. This was applied after seeing
 974 that most cosmic induced clusters passing were long with high angles, while neutrino
 975 induced clusters were mainly forward going. We required a good cluster to either
 976 have a projected start angle less than 30 degrees from the z axis or be less than 200
 977 wires long. The length cut was added to make sure we don't cut any short high angle
 978 clusters that can correspond with a proton, or other highly ionizing particle associated
 979 with a long muon cluster. The 200 wire cut roughly equates to 0.6 m in the z direction,
 980 with a 3 mm wire pitch. Also, the projected angle is defined by $\tan \alpha = \Delta T / \Delta W$ where
 981 T is the time ticks and W is the wires.

982 The last cut requires the clusters to be either 30 time ticks or 30 wires. This cut was
 983 applied to reduce small delta rays associated with a cosmic without removing proton
 984 clusters associated with a long muon cluster, which saves ideal neutrino events that
 985 have both a long minimum ionizing muon like cluster and a short highly ionizing
 986 proton like cluster.

987 **Secondary Cuts**

988 The secondary cuts look to match long, low-angle clusters with short, high-charge
 989 clusters. Only clusters that have passed previous cuts are used. First clusters with
 990 length greater than 100 wires are chosen, which is approximately 0.3 m in the z

Cluster set	No Cuts	Primary Cuts	Secondary Cuts
Neutrinos only	570	303	32
Cosmics only (no flash)	308,016	291,879	602
Cosmics only (w/ flash)	2464	2335	5
Neutrinos/Cosmics	0.23	0.13	6.4

Table 4.1: Passing rates for 2D cluster cuts for neutrino on MC set and a cosmic only MC set. First column shows event rates with no cuts applied to both sets. Columns two and three show event rates after primary and secondary cuts are applied. Line three shows the second line scaled with the flash finding factor of 0.008. All events are normalized to per day assuming we are running at 5 Hz.

991 direction. Then we search for any cluster that is within approximately 3 cm (10 wires
 992 and 30 time ticks) away from the low-z end of the long cluster. This cluster must also
 993 be shorter than the first. In our reconstruction, the start and end point of a cluster can
 994 be swapped so both ends of the short cluster are compared to the long cluster.

995 Now that there is a vertex match, cuts based on charge and projected opening angle
 996 are implemented. We require the short cluster to have a higher start charge than the
 997 long cluster or the long cluster be longer than 500 wires. Start charge is defined as
 998 the charge on the first wire in ADC counts. The projected opening angle must also
 999 be between 11 and 90 degrees. This last cut is intended to remove clusters that are
 1000 entirely overlapping or are part of the same long track. The resulting neutrino/cosmic
 1001 event rate per day is shown in table 4.1. Figures 4.3 and 4.4 shows the percentages of
 1002 clusters that pass each primary and secondary cuts.

1003 4.2.3 3D Tracks and vertices Selection

1004 The neutrino selection for the 3D channel was based on a reconstructed vertex and
 1005 two tracks. All vertices and tracks were looped over that had a cosmic tag score < 0.4
 1006 and the distances below were calculated:

- 1007 • d : distance between the start points of the two tracks.
- 1008 • d_1 : distance between vertex and start of track 1.
- 1009 • d_2 : distance between vertex and start of track 2.

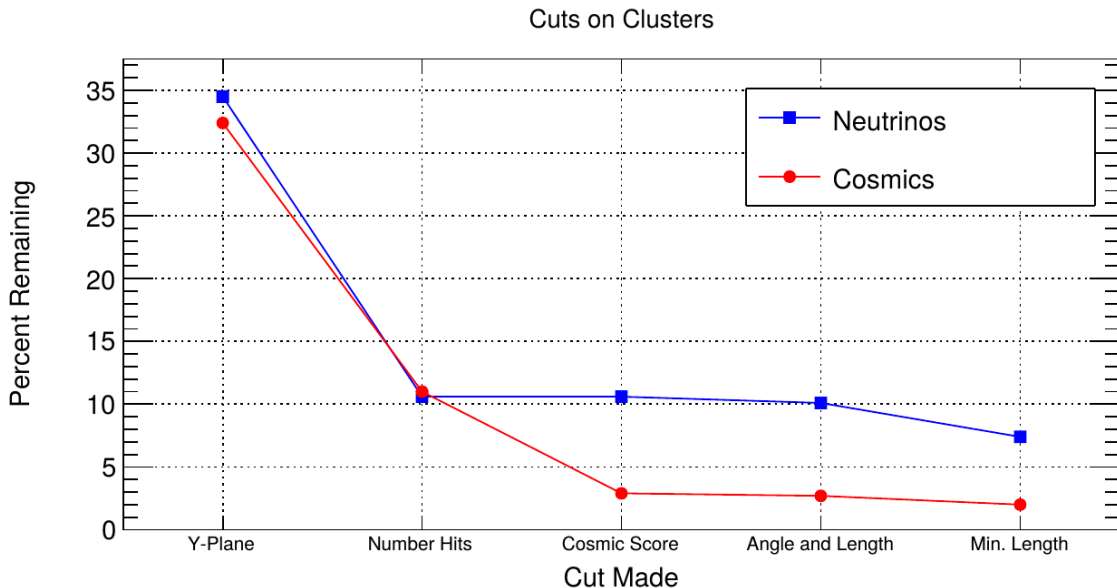


Figure 4.3: Percent of good clusters remaining for neutrinos and cosmics after the primary cuts were applied. This is relative to total number of initial clusters.

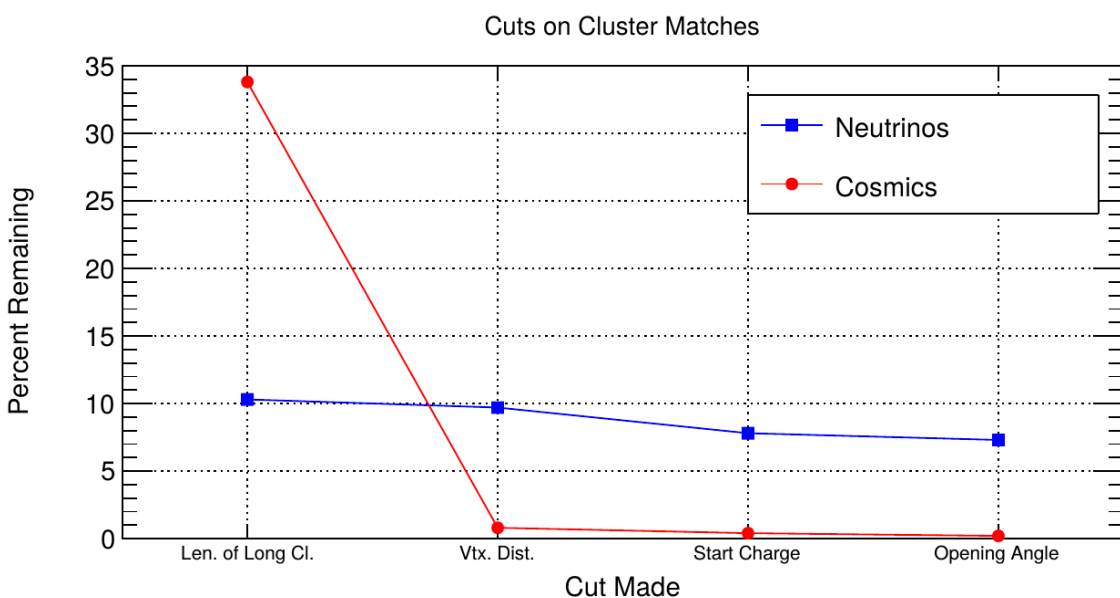


Figure 4.4: Percent matched cluster pairs remaining for neutrinos and cosmics after secondary cuts applied. This is relative to the number of events that contain clusters which pass the primary cuts.

1010 The maximum distance of all three is then selected as the important characteristic per
1011 trio. The best trio is the one that has the smallest maximum distance. The $\min(\max_d)$
1012 for all trios in an event were plotted for BNB neutrino events and for cosmics to
1013 find the best cut value for each tracking algorithm. The distribution of $\min(\max_{d,i})$
1014 is smaller for neutrinos than for cosmics. The cut values for different tracking and
1015 clustering algorithms are shown below. These cut values were chosen to minimize the
1016 cosmic background to 20%.

- 1017 • trackkalmanhit with cccluster $\min(\max_{d,i}) < 3$ cm.
1018 • trackkalmanhit with pandoraNu $\min(\max_{d,i}) < 4.5$ cm.
1019 • pandoraNu with cccluster $\min(\max_{d,i}) < 5$ cm.

1020 **4.2.4 TPC Updates**

1021 After doing a visual hand-scanning of the first beam data processed with the filters
1022 detailed above, the events passing had a larger contamination of background than
1023 expected. This was mainly in part due to the reconstruction performing better on
1024 simulation than on data. Due to this, additional cuts on both streams needed to be
1025 implemented in order to increase signal/background ratio. These cuts were added on
1026 top of the filters described above and further reduce the event count.

1027 **2D Filter Updates**

1028 The main background observed in the 2D filter were Michel events, where the muon
1029 and electron formed two connected clusters. These events were rejected by comparing
1030 the start and end charge deposition of the long cluster (i.e muon particle). The start
1031 charge deposition must be less than the end charge deposition. This cut is implemented
1032 because muons have a higher ionizaiton loss at the end.

1033 **3D Filter Updates**

1034 It was seen that cosmic tracks can often originate or end at the same point, therefore
1035 faking a signal. Cosmic tracks, however, are mostly vertical. By requiring the angle
1036 of the longer track have a cosine greater than 0.85 with respect to the z-axis as well

₁₀₃₇ as requiring the longer track to have a length greater than 10 cm, we can reduce this
₁₀₃₈ background.

₁₀₃₉ **4.3 Conclusion**

₁₀₄₀ After proccesing these filters in parallel, it was shown that the 3D filter had a higher
₁₀₄₁ purity than the 2D filter because of the higher cosmic rejection being used due to 3D
₁₀₄₂ reconstruction. The 2D filter is blind to track entering/exiting from the top or bottom
₁₀₄₃ of the TPC. Although the 3D filter had a higher purity, the 2D filter was still able to
₁₀₄₄ find identifiable events in data that were used as public event displays. A sample of
₁₀₄₅ event displays are shown in figures 4.5 and 4.6.

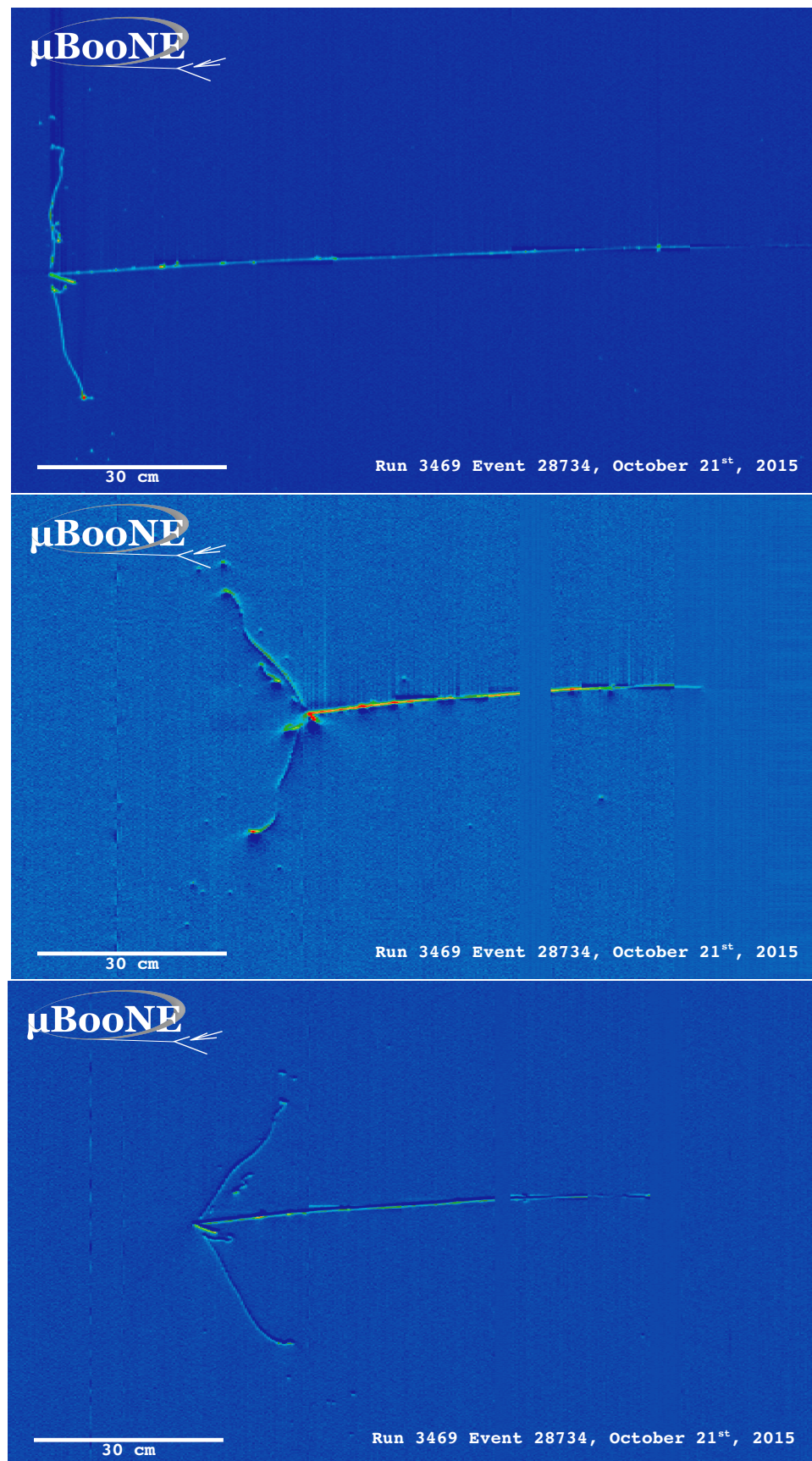


Figure 4.5: First Neutrino Interaction Candidate Events from MicroBooNE

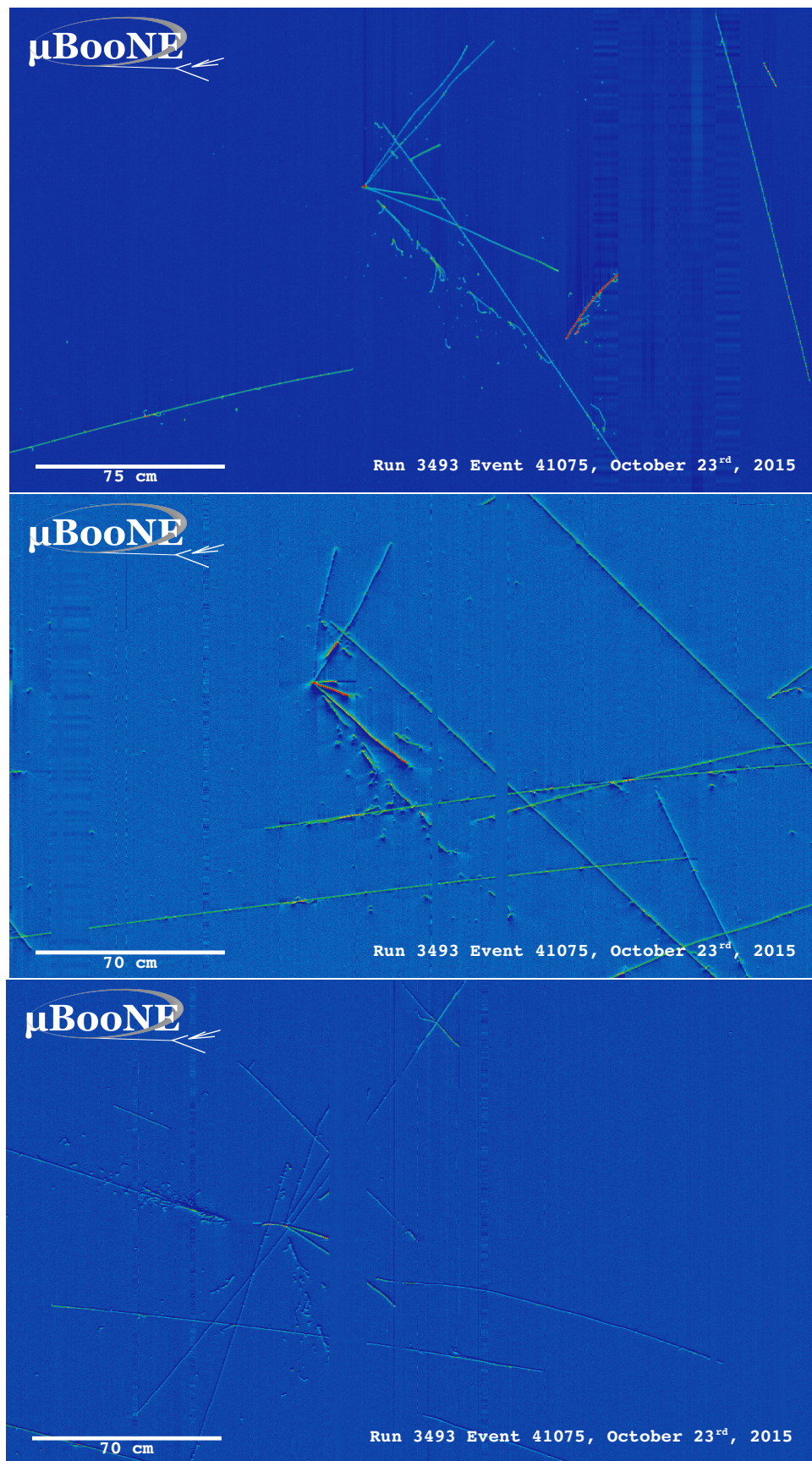


Figure 4.6: First Neutrino Interaction Candidate Events from MicroBooNE

1046 **Chapter 5**

1047 **CC-Inclusive Cross Section Selection**

1048 **Filter**

1049 The CC-Inclusive cross-section selection I and selection I modified filters used in this
1050 analysis will be described in the following sections below. These filters are an expansion
1051 of the Neutrino ID filter. The work done in this thesis was to further improve these
1052 selections by increasing both efficiency and purity as well as increasing acceptance
1053 without further affecting the kinematic distributions of the selected neutrino events.

1054 MicroBooNE requires fully automated event reconstruction and selection algorithms for use in the many physics measurements being worked on to date due to
1055 the large data rate MicroBooNE receives. Being able to automatically pluck out the
1056 neutrino interaction among a sea of cosmics proved to be challenging but was accomplished.
1057 MicroBooNE has developed two complementary and preliminary selection
1058 algorithms to select charged-current $\nu_\mu - Ar$ interactions. Both are fully automated
1059 and cut based. The results of this thesis will focus on selection I and selection I modified
1060 and will focus on further improving these algorithms using Convolutional Neural
1061 Network (CNN) implementations. These selections identify the muon from a neutrino
1062 interaction without biasing towards track multiplicity. To combat cosmic and neutral
1063 current background, the analysis is strongly biased towards forward-going long tracks
1064 which are contained. This limits phase space and reduces acceptance.
1065

1066 5.1 Data and MC Processing Chain

1067 The data used for this analysis were based on hardware and software triggers. Events
1068 used came from the *BNB_INCLUSIVE* and *EXT_BNB_INCLUSIVE* streams and were
1069 used for signal and background. The *BNB_INCLUSIVE* stream is chosen by requiring
1070 that the hardware trigger bit is fired and that the event passed an optical software
1071 trigger within a BNB spill timing window. The *EXT_BNB_INCLUSIVE* stream requires
1072 the EXT hardware trigger to fire as well as pass the same optical software trigger
1073 within a BNB spill size timing window similar to the *BNB_INCLUSIVE*.

1074 The two MC samples used in this analysis and for determining selection efficiencies
1075 and purities were GENIE BNB neutrino interactions with CORSIKA cosmic ray overlay
1076 within the readout window and inTime CORSIKA cosmic rays. The MC samples
1077 generated used *uboonecode v04_36_00* and are based on the following packages:

- 1078 • larsoft v04_36_00
- 1079 • GEANT v04_09_06_p04d
- 1080 • GENIE v02_08_06d
- 1081 • GENIE xsec v02_08_06a
- 1082 • pandora v02_03_0a
- 1083 • CORSIKA v07_4003

1084 Both data and MC samples were processed using the same reconstruction release,
1085 *uboonecode v05_08_00* and the fcl files used for reconstruction are listed below:

- 1086 • MC fcl files
 - 1087 – reco_uboone_mcc7_driver_stage1.fcl
 - 1088 – reco_uboone_mcc7_driver_stage2.fcl
- 1089 • Data fcl files
 - 1090 • reco_uboone_data_Feb2016_driver_stage1.fcl
 - 1091 • reco_uboone_data_Feb2016_driver_stage2.fcl

1092 On top of the hardware and software triggers, the data also had to pass more
1093 criteria to be identified as part of the good run list. The criteria is detailed below.

- 1094 • **Detector conditions:** the detector has to be in a good operating condition. The
 1095 detector conditions are read from the slow monitoring database and are required
 1096 to be within the alarm thresholds. The variables of interest for events passing
 1097 the good run list criteria include DAQ, PMT, HV, Drift HV, wire bias, electron
 1098 lifetime and detector power. These conditions need to be met on a run-by-run
 1099 basis in order to pass the selection.
- 1100 • **Data quality:** normal and stable behavior for basic reconstruction quantities.
 1101 These reconstruction variables include average number of tracks, hits, and flashes
 1102 in each event, the average length of tracks, the average amplitude and area of
 1103 hits, the average PE and the average spread of each one of these quantities.
- 1104 • **Beam Conditions:** the BNB must be on and stable and the POT per spill needs
 1105 to above the intensity threshold. Beam quality conditions include checking the
 1106 fraction of proton beam interacting within the target, the horn current, and the
 1107 intensity of protons per spill. The final sample is $5 * 10^{19}$ and a per-spill intensity
 1108 of $4 * 10^{12}$
- 1109 • **Run processed:** the full run must be processed completely without missing
 1110 subruns or crashes in the data processing.

1111 5.2 Normalization of data and MC

1112 The off-beam sample is used to measure beam unrelated backgrounds. For normalization
 1113 one needs the total number of BNB spills (N_{BNB}) and the total number of external
 1114 triggers. The BNB spills used need to pass the beam quality cuts. The normalization
 1115 factor is then N_{BNB}/N_{EXT} which is 1.23.

1116 To normalize generated BNB MC events to POT, we used the following:

- 1117 • $5 * 10^{19} POT = 41524.3$ generated events

1118 where this scaling factor only applies to mcc7 generated events. The inTime cosmic
 1119 sample is normalized with respect to the open cosmic sample so an understanding
 1120 of both is necessary. The POT per beam spill for mcc7 BNB samples is $5 * 10^{12}$. To
 1121 calculate how many spills are necessary to produce a specific POT one would multiply
 1122 the total POT by the average 1/POT per spill. For a total POT of $5 * 10^{19}$ the amount
 1123 of spills necessary is $\frac{5 * 10^{19}}{5 * 10^{12}} = 1 * 10^7$. This is only one in ~ 241 events therefore each

cosmic event needs to be scaled up by a factor of 240.8 when comparing to BNB MC. For inTime cosmics however, two filters are applied to reduce computing and processing time and only leave cosmics that will interact within the detector. The passing rate after these two filters is 0.02125, therefore the total inTime cosmic scaling factor to compare inTime cosmics to BNB is $0.02125 * 240.8 = 5.12$.

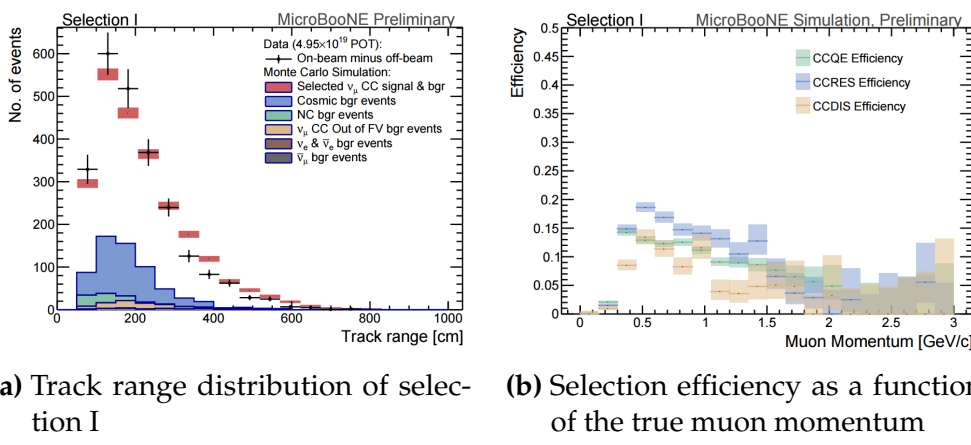


Figure 5.1: 5.1a Track range distribution for selection I. The track range is defined as the 3D distance between the start and end of the muon candidate track. No data is shown below 75 cm due to the track length cut described previously. 5.1b Efficiency of the selected events by process quasi-elastic (QE), resonant (RES), and deep-inelastic (DIS). Statistical uncertainty is shown in the bands and the distributions are a function of true muon momentum. The rise of the efficiency between 0 GeV and 0.5 GeV is due to the minimum track length cut and the decreasing efficiency for higher momentum tracks is caused by the containment requirement.

5.3 Optical Software Trigger and Reconstruction

5.3.1 Software Trigger

Most of the BNB spills from the accelerator do not have a neutrino interaction in MicroBooNE. To save computation resources and reduce data-rates, we require a burst of light in the light collection system in coincidence with the 1.6 μ s beam spill. Requiring light activity in coincidence with the beam spill eliminates the vast majority of triggers with no neutrino interaction in the detector, however, it doesn't guarantee the activity in the detector is a neutrino interaction since a cosmic ray can interact in coincidence with the beam spill as well.

1138 To implement this, a software trigger was used on the PMT waveforms to decide
1139 whether or not to keep that event. The software trigger is implemented after the event
1140 builder combines data from the PMTs and triggers into a single event. The software
1141 trigger uses the digitized output of the 32 PMT channels in the light collection system.
1142 Only the waveform region in coincidence with the beam spill is used to search for
1143 possible triggers. For each PMT, a waveform is found by taking the difference of ADC
1144 values is calculated between t and $t + s$. This waveform is then scanned for ADC
1145 values above a threshold X_0 . Once an ADC is above this threshold, a discriminator
1146 window is opened for a fixed number of time ticks (W_0). If the ADC count within this
1147 window W_0 is greater than a second larger threshold X_3 , a final window of width W_3
1148 is opened. The max ADC value within this final window is set as the peak amplitude
1149 for the PMT and then summed across all 32 PMTs and set to the variable PHMAX. The
1150 software trigger places a final cut on the PHMAX variable to decide whether or not
1151 to keep the event. The thresholds were found by the Trigger task force using Monte
1152 Carlo Studies and are as follows:

- 1153 • $X_0 = 5$ ADC
- 1154 • $X_3 = 10$ ADC
- 1155 • $W_0 = 6$ Ticks
- 1156 • $W_3 = 6$ Ticks
- 1157 • PHMAX cut = 130 ADC

1158 5.3.2 Flash Reconstruction

1159 MicroBooNE collects light from each of the 32 PMTs either in a continuous readout
1160 window of $23.4 \mu\text{s}$ activated by a beam gate signal on the trigger board, or in discrimi-
1161 nated pulses of $\sim 1 \mu\text{s}$ duration activated if the ADC count for any PMT goes above 80
1162 ADC count. These two formats are saved as output waveforms and put onto an event.
1163 Additionally, each PMT can provide two output streams, high-gain (~ 20 ADC/PE)
1164 and low-gain (~ 2 ADC/PE) channels. The first step in the reconstruction is to merge
1165 both these channels into a “saturation corrected waveform” which uses information
1166 from the low-gain waveform to correct for saturating high-gain pulses.

1167 The saturation corrected waveform in the continuous readout window is used to
1168 reconstruct optical hits. Each PMT’s waveform is scanned for hits then a threshold

1169 based hit reconstruction algorithm is applied which requires pulses of a minimum
1170 area in order to be reconstructed. Each reconstructed hit is associated to a PMT, a time
1171 in μs , and a PE count.

1172 Once hits are reconstructed for all 32 PMTs, all PMT information is then combined
1173 into optical flashes which represent optical information seen by the PMTs from interac-
1174 tions in the detector. Each flash has information on total light seen per interaction, the
1175 distribution of the light across all 32 PMTs, the flash time with respect to the trigger
1176 time of the flash, and lastly, the spacial information of the flash in Y-Z plane of the
1177 detector. These flashes are reconstructed by requiring that there is a $\sim 1 \mu\text{s}$ coincidence
1178 between the reconstructed hits in all 32 PMTs. The total PE is summed up among
1179 all coincident hits across the PMTs and if the total PE is greater than 2 PE, a flash is
1180 reconstructed. There are also safe guards in place to take care of late scintillation light.

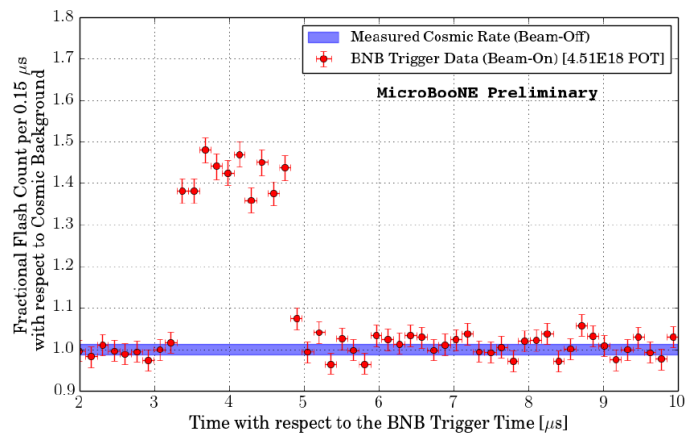


Figure 5.2: Time distribution of reconstructed optical flashes with a PE value of 50 or more for a sample of BNB unbiased triggered events.

1181 Figure 5.2 shows the time distribution of reconstructed optical flashes using the
1182 BNB continuous stream. You can see a clear excess in coincidence with the expected
1183 arrival time of neutrinos. The same flash reconstruction that was used in the cc-
1184 inclusive filter detailed here was used to create this plot in data.

1185 5.3.3 Beam Window

1186 Figure 5.3 shows the distribution of flashes for on-beam, off-beam and various MC
1187 samples. The software trigger has been applied to these samples. The pile-up seen just
1188 after 0 μs is a feature of the flash finding algorithm and consists of low PE flashes and

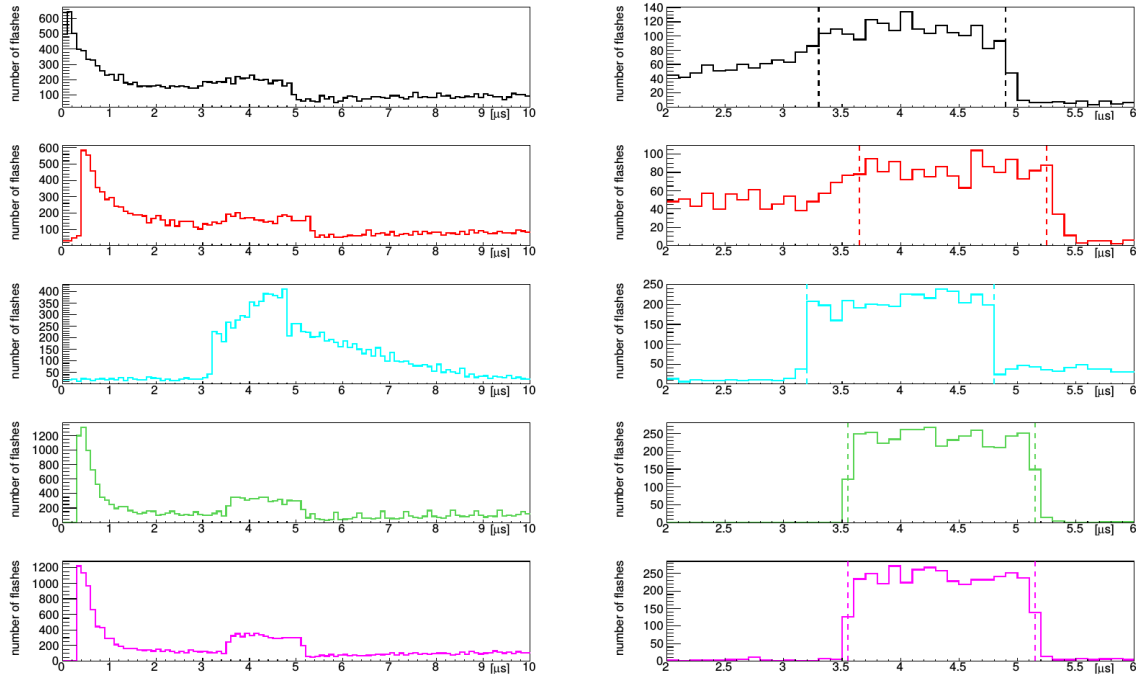


Figure 5.3: Flash time distribution for all flashes (left plot) and flashes $> 20\text{PE}$ (right plot). The different curves are as follows: on-beam data (black), off-beam data (red), CORSIKA inTime MC (light blue), BNB only MC (green), and BNB+Cosmic MC (purple). The dashed vertical lines mark the time window that was chosen for each sample

is removed in the second column of distributions with a low 20 PE threshold cut. The plots show that the time window for the distributions are shifted a small amount from each-other. This is caused by different hardware configurations per sample. Using these distributions, the windows chosen per sample are as follows:

- On-Beam: 3.3 to 4.9 μ s
- Off-Beam: 3.65 to 5.25 μ s
- CORSIKA inTime: 3.2 to 4.8 μ s
- BNB only: 3.55 to 5.15 μ s
- BNB+Cosmic: 3.55 to 5.15 μ s

Each window has a width of 1.6 μ s.

5.4 TPC Reconstruction

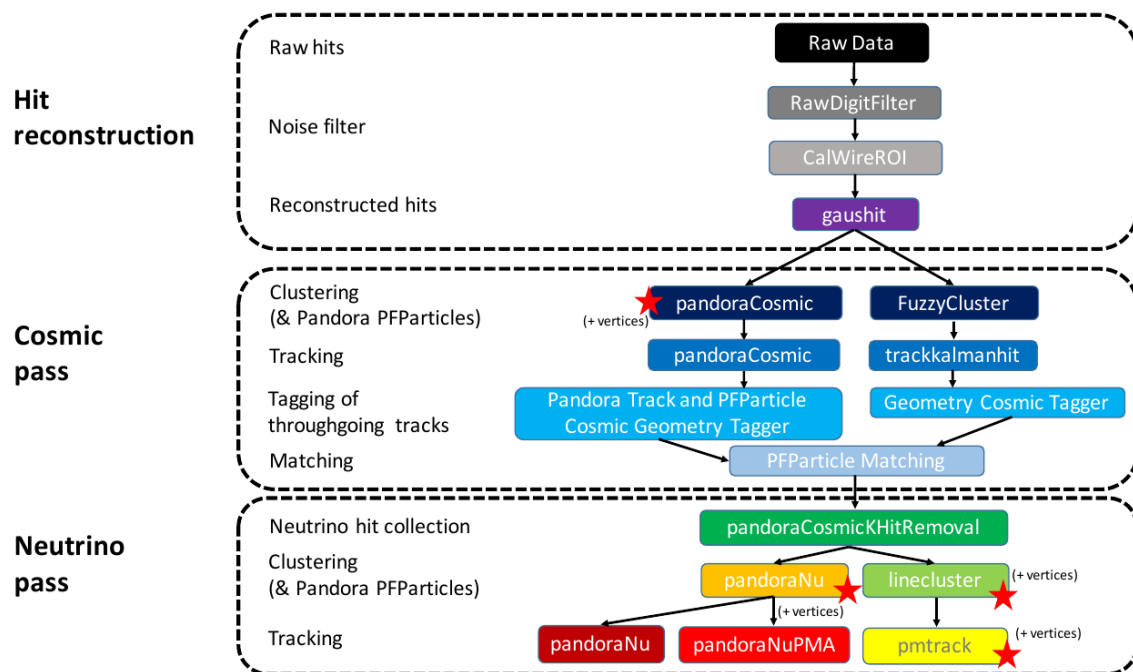


Figure 5.4: Reconstruction chain run on both data and MC. The red stars mean that the algorithm returns reconstructed 3D vertices.

1200 Figure 5.4 summarizes the reconstruction chain applied to both MC and data for
1201 this analysis. After the hit reconstruction, a cosmic pass is applied which removes all
1202 hits associated to through-going tracks. A description of these TPC reconstruction
1203 algorithms will be detailed below.

1204 **5.4.1 Hit Reconstruction**

1205 The waveforms used for hit reconstruction consist of charge deposited on the sense
1206 wire in drift time. The first step in hit reconstruction is to pass the waveforms through
1207 a filtering algorithm to filter out the noise introduced from the electronics. The input
1208 waveforms are also truncated from 9600 time ticks to 6400 time ticks in this first step
1209 to reduce the data footprint of these waveforms.

1210 Once noise filtering is complete, a deconvolution algorithm is applied to the wave-
1211 forms to remove the drift field and electronics response, therefore leaving only the
1212 ionized electrons kicked off the argon atoms by an incident track. During this process,
1213 Region of Interests (ROI) are identified and cut out of the waveforms to further reduce
1214 the data volume.

1215 The hit finding algorithm then finds candidate peaks in these ROI's and fits the
1216 peaks to Gaussian curves. These Gaussian shaped peaks are now called hits and
1217 represent the charge deposition on a wire by the incoming track. These hit objects
1218 have a peak time and width and are the basic object input to further algorithms down
1219 the reconstruction chain.

1220 **5.4.2 Clustering**

1221 There are multiple clustering algorithms used in this analysis. The main purpose of all
1222 the clustering algorithms is to associate hits together in 2D space to create objects like
1223 tracks, vertices and showers. For the fuzzy cluster algorithm, three steps are used to
1224 achieve this. The first step is to associate hits to each-other using a fuzzy clustering
1225 algorithm which gives each hit a degree of belonging to the cluster. Second, a Hough
1226 transform is used to find hits associated to candidate tracks and showers within each
1227 of the clusters found in the first step. The last step merges smaller candidate tracks
1228 and showers into large clusters. The last step also associates unclustered hits into

1229 nearby objects which helps shower reconstruction. The result is a set of clusters made
1230 up of associate hits that represent tracks or showers per plane.

1231 The pandora algorithm utilizes it's own clustering algorithm and will be detailed
1232 in the next section. The last clustering algorithm is called linecluster. The linecluster
1233 algorithm reconstructs 2D linear clusters per plane by fitting a line onto nearby hits
1234 which is then extrapolated to neighboring wires. 2D vertices are found per plane by
1235 using the intersection points of the ends of nearby clusters. These 2D vertices are then
1236 matched in time across all three planes to get a 3D vertex in space.

1237 5.4.3 Pandora

1238 5.4.4 Trackkalmanhit

1239 The trackkalmanhit algorithm takes 2D clusters returned from the fuzzy cluster algo-
1240 rithm and outputs track objects. There are no hierarchy structure as it is in pandora,
1241 each track is independent. There also is no vertex reconstruction with this algorithm
1242 as well.

1243 5.4.5 Cosmic Hit Removal

1244 The Pandora algorithm is applied to the events twice, the first to remove downward
1245 going tracks primarily from cosmic ray muon like particles. The second pass only runs
1246 on a subset of hits that aren't associated with cosmic ray muon tracks.

1247 After the first pass, the output of PFParticle hierarchy is then passed to a cosmic
1248 ray tagger to look through all hits to determine start and end points. If the start or
1249 end point trajectories are consistent with entering or exiting the TPC, then these hits
1250 are removed from the second pass. Hits are considered entering or exiting the TPC
1251 if the drift time are outside of the neutrino drift window or outside of the fiducial
1252 volume of the TPC. The fiducial volume was based on a montecarlo study and is 20
1253 cm from the top or bottom of the TPC and 10 cm from the TPC ends. Hits associated
1254 with candidate cosmic ray tracks are removed from the input hit collection and the
1255 remaining hits are passed to the neutrino optimized pass of Pandora.

1256 5.4.6 Projection Matching Algorithm

1257 The projection matching algorithm (PMA) was inherited from ICARUS and has been
1258 implemented in LArSoft. PMA differs from traditional LArSoft 3D reconstruction
1259 algorithms. Most 3D reconstruction attempts to match 2D objects from all three planes
1260 by drift time, while the PMA algorithm projects a track hypothesis on each plane
1261 then the distance between this projection and the hits on each plane is minimized
1262 simultaneously. More information can be found in [?].

1263 5.5 Event Selection

1264 The first requirement for selecting ν_μ CC events is that the event has at least one
1265 scintillation light flash in the beam trigger window with more than 50 PE on all PMTs
1266 combined. From the flashes that pass, the most intense is chosen and considered to be
1267 originating from a neutrino interaction and will be the only flash used in further cuts.

1268 Vertices are then required to have at least one reconstructed track start or endpoint
1269 within a 5 cm radius. Showers associated with a vertex do not pass this cut. All
1270 tracks associated with a vertex are then used to calculate a track length weighted
1271 average of the θ -angle. Of all the vertices that do pass, only the vertex with the most
1272 forward going θ -angle average of all associated tracks is considered the neutrino vertex
1273 candidate. The most forward going θ -angle average is chosen by picking the largest
1274 track range weighted average of $|\cos(\theta)|$, seeing as $\cos(\theta) = 1$ is the beam direction.
1275 Next, it is required that the reconstructed neutrino vertex candidate be within the
1276 fiducial volume as well as within the drift time starting at t_0 . The fiducial volume
1277 boundaries chosen are 10 cm from the edges of the TPC in x and z which is the drift
1278 direction and beam direction respectively, and 20 cm from the edges of the TPC in y
1279 which is the vertical direction. For all further cuts, only the longest track associated
1280 with the neutrino vertex candidate and this track is assumed to be the muon candidate
1281 of the neutrino event.

1282 The next cut requires the position of the flash in the z-direction and the track z-
1283 projection to be compared. This basic flash matching algorithm is rudimentary and a
1284 placeholder for a more sophisticated algorithm. The z-position of the flash needs to be
1285 within 80 cm to the z-positions of track start or endpoints. If the flash is between the
1286 track start and endpoint, the distance of the flash to the track is considered to be 0 cm.

1287 Lastly, the track needs to be fully contained within the fiducial volume and have a
1288 track range greater than 75 cm. The range is the 3D distance between the track's start
1289 and endpoint. The length cut was optimized to remove NC background that contain
1290 a pion due to the pion interaction rate to be ~ 70 cm. A track that makes all the cuts
1291 is considered to be the muon of a ν_μ CC event. The list of cuts for this selection is
1292 described below:

- 1293 1. At least one flash > 50 PE within the beam gate.
- 1294 2. At least one track within 5 cm around a vertex.
- 1295 3. Vertex with flattest tracks is chosen to be vertex candidate.
- 1296 4. Vertex candidate in fiducial volume.
- 1297 5. Longest track associated with vertex candidate is chosen to be track candidate.
- 1298 6. Longest track is within 80 cm (z-axis only) of the flash.
- 1299 7. Longest track is fully contained.
- 1300 8. Longest track is greater than 75 cm.

1301 The event selection scheme can also be seen in figure 5.5. Table 5.1 lists the passing
1302 rates for MC events for the selection scheme described above. Table 5.2 lists the passing
1303 rates for on-beam and off-beam data for the selection scheme. The normalization
1304 factors applied between on-beam and off-beam data are described in section 5.2.

1305 5.5.1 Expected Backgrounds

1306 Most of the selected background events will be of cosmic origin. There are two types
1307 of cosmic background, one triggered by a cosmic-ray event occurring in the beam
1308 gate time window, the other triggered by a beam induced interaction in the cryostat
1309 followed by a misidentification of a cosmic event as a neutrino event. The first
1310 cosmic background can be subtracted from the selected events using the off-beam
1311 BNBEXT sample normalized to the on-beam. The second cosmic background events
1312 are modeled by MC by using BNB+Cosmic MC sample.

1313 Other backgrounds originate from neutrino beam contaminants. A major contribu-
1314 tion in this sector is by neutral current neutrino events for example a charged pion track
1315 misidentified as a muon. Another contribution are ν_e -like and anti-muon-neutrino

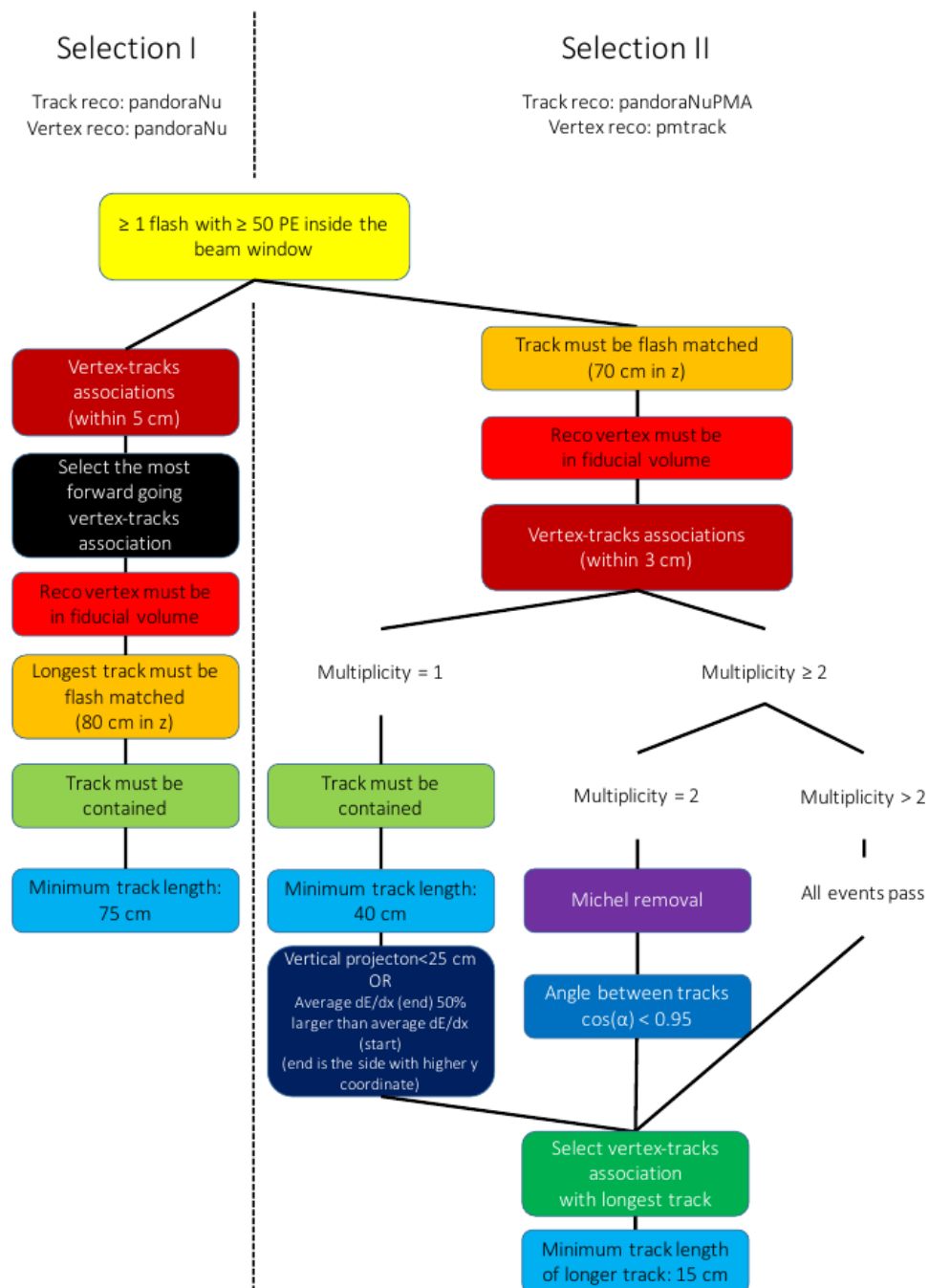


Figure 5.5: Event selection diagram for selection I and selection II. This analysis focused on optimizing selection I. Boxes with the same color across the two selections symbolize similar cuts.

	BNB+Cosmic Selection	BNB+ Cosmic MC-Truth	Cosmic Only	Signal:Cosmic Only
Generated Events	191362	45273	4804	1:22
≥ 1 flash with ≥ 50 PE	136219 (71%/71%)	44002 (97%/97%)	2970 (62%/62%)	1:14
≥ 1 track within 5 cm of vertex	135830 (99%/71%)	43974 (99%/97%)	2975 (99%/62%)	1:14
vertex candidate in FV	79112 (58%/41%)	34891 (79%/77%)	1482 (50%/31%)	1:8.9
flash matching of longest track	40267 (51%/21%)	25891 (74%/57%)	340 (23%/7.1%)	1:2.8
track containment	19391 (48%/10%)	11693 (45%/26%)	129 (38%/2.7%)	1:2.3
track ≥ 75 cm	6920 (36%/3.6%)	5780 (49%/13%)	17 (13%/0.4%)	1:0.6

Table 5.1: Passing rates of Selection I. Numbers are absolute event counts and cosmic background is not scaled. The BNB+Cosmic sample contains all events, not just ν_μ CC inclusive. The numbers in brackets give the passing rate wrt the step before (first percentage) and wrt total generated events (second percentage). The BNB+Cosmic MC-Truth column shows how many true ν_μ CC inclusive events are left in the sample. This number includes mis-identifications where a cosmic track is picked by the selection instead of the neutrino interaction in the same event. The cosmic only sample is used just to illustrate the cut efficiency. The last column Signal:Cosmic only gives an estimate of the ν_μ CC events wrt the cosmic only background at each step. For this number, the cosmic background has been scaled as described in section 5.2.

	on-beam	off-beam
Generated Events	546910	477819
≥ 1 flash with ≥ 50 PE	135923 (25%/25%)	96748 (20%/20%)
≥ 1 track within 5 cm of vertex	134744 (99%/25%)	95778 (99%/20%)
vertex candidate in FV	74827 (55%/14%)	51468 (54%/11%)
flash matching of longest track	22059 (29%/4.0%)	12234 (24%/2.6%)
track containment	10722 (49%/1.9%)	5283 (43%/1.1%)
track ≥ 75 cm	3213 (30%/0.6%)	1328 (25%/0.3%)

Table 5.2: Passing rates for Selection I selection applied to on-beam and off-beam data. The numbers in brackets give the passing rate wrt the step before (first percentage) and wrt the generated events (second percentage). Off-beam data has been scaled with a factor 1.23 to normalize to the on-beam data stream.

1316 events. These beam related backgrounds are an order of magnitude smaller than the
1317 cosmic misidentification backgrounds. These backgrounds can not be subtracted and
1318 are estimated using MC truth.

1319 The efficiency and purity of Selection I are calculated below:

- 1320 • Efficiency: Number of selected true ν_μ CC events divided by the number of
1321 expected true ν_μ CC events with interaction in the FV.

1322 – $(12.3 \pm 3.4) \%$

- 1323 • Purity: Number of selected true ν_μ CC events divided by the sum of itself and
1324 the number of all backgrounds.

1325 – $(53.8 \pm 4.4) \%$

1326 5.5.2 Truth Distributions

1327 The truth distributions of MC truth variables before and after the selection are detailed
1328 in this section. The overall efficiencies are calculated for all ν_μ CC signal events
1329 with a true interaction within the fiducial volume and a fully contained muon track
1330 originating from said vertex. Figures 5.6 through 5.8 detail the truth distributions for
1331 muon momentum, $\cos(\theta)$ and ϕ and figures 5.9 through 5.11 detail the total efficiency
1332 of the selection for charged current quasi elastic (CCQE) events, charged current
1333 resonant (CCRES) events, and charged current deep inelastic (CCDIS) events.

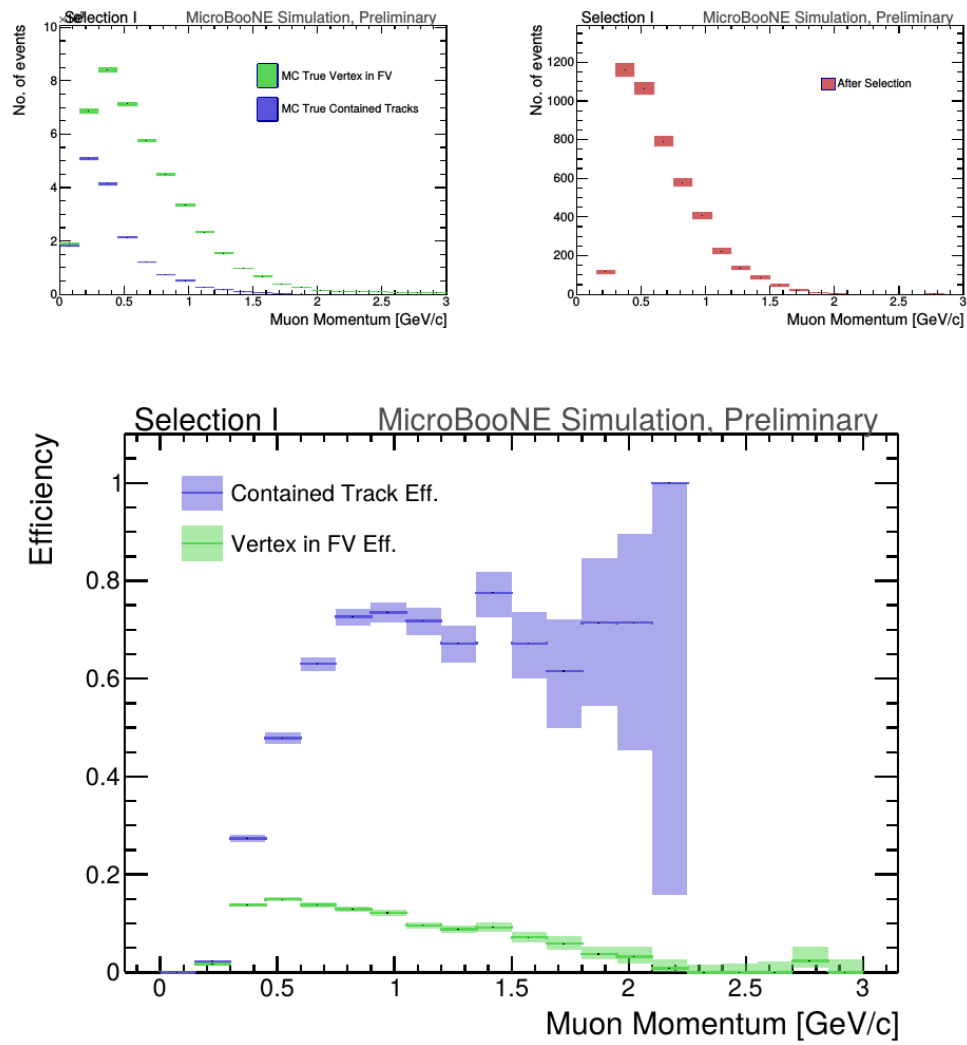


Figure 5.6: MC momentum distributions of the muon originating from a ν_μ CC interaction. Upper left is the momentum distributions of events with a vertex within the FV (green) and the events with a fully contained track (blue) before the selection. The upper right side is the momentum distribution after the selection (red). The lower plot is the selection efficiencies.

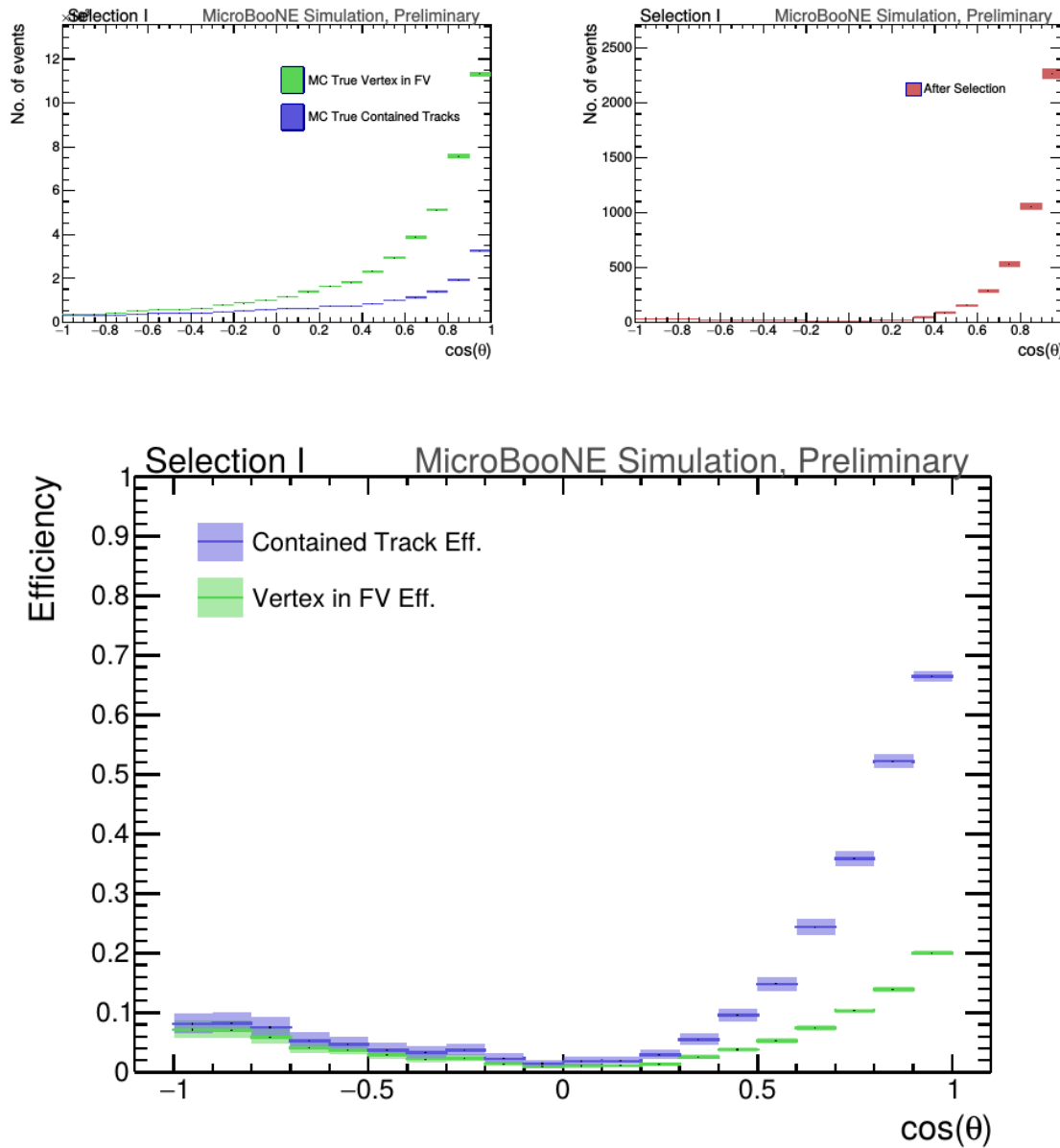


Figure 5.7: MC $\cos(\theta)$ distributions of the muon originating from a ν_μ CC interaction. Upper left is the $\cos(\theta)$ distributions of events with a vertex within the FV (green) and the events with a fully contained track (blue) before the selection. The upper right side is the $\cos(\theta)$ distribution after the selection (red). The lower plot is the selection efficiencies.

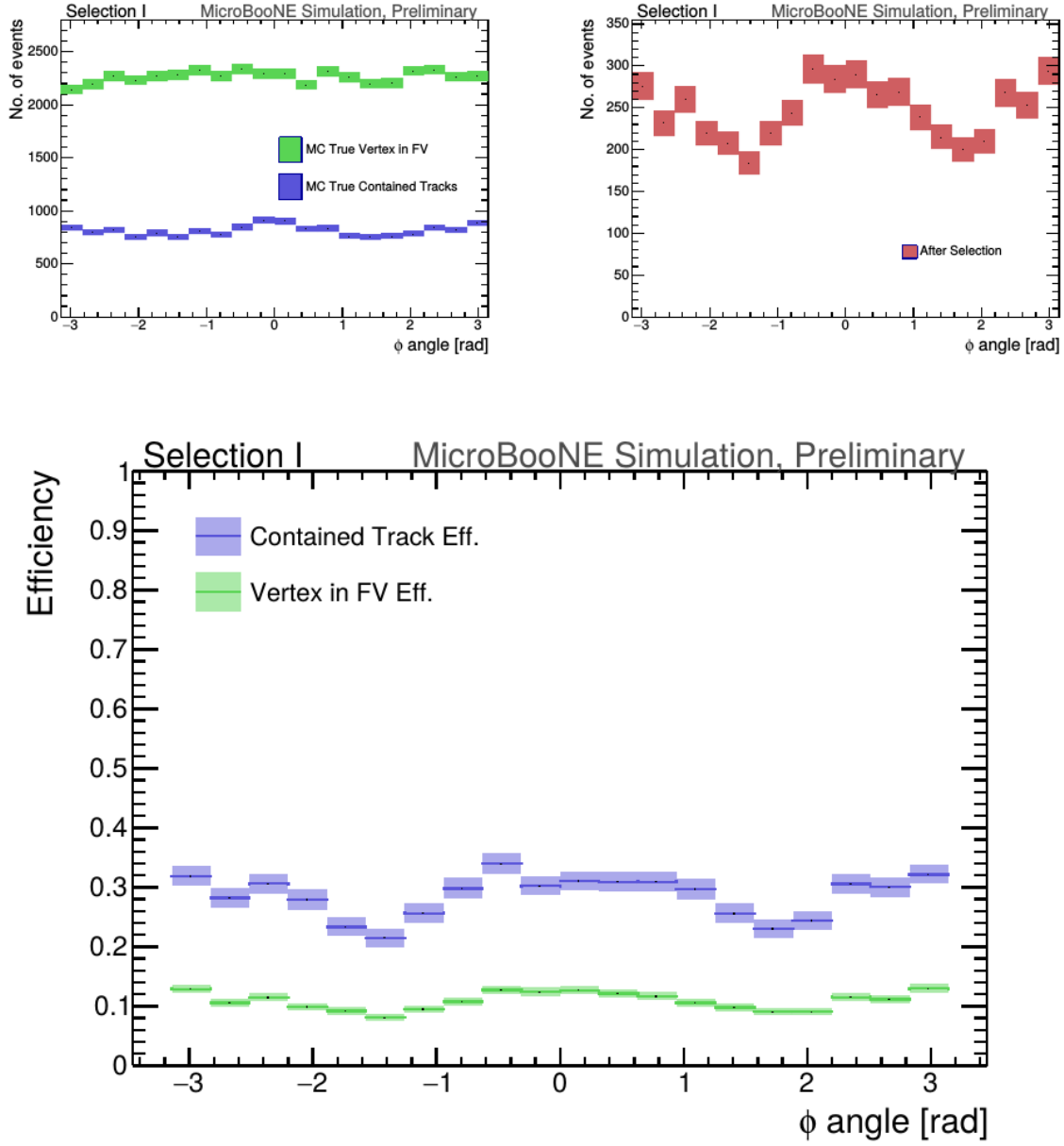


Figure 5.8: MC ϕ distributions of the muon originating from a ν_μ CC interaction. Upper left is the ϕ distributions of events with a vertex within the FV (green) and the events with a fully contained track (blue) before the selection. The upper right side is the ϕ distribution after the selection (red). The lower plot is the selection efficiencies.

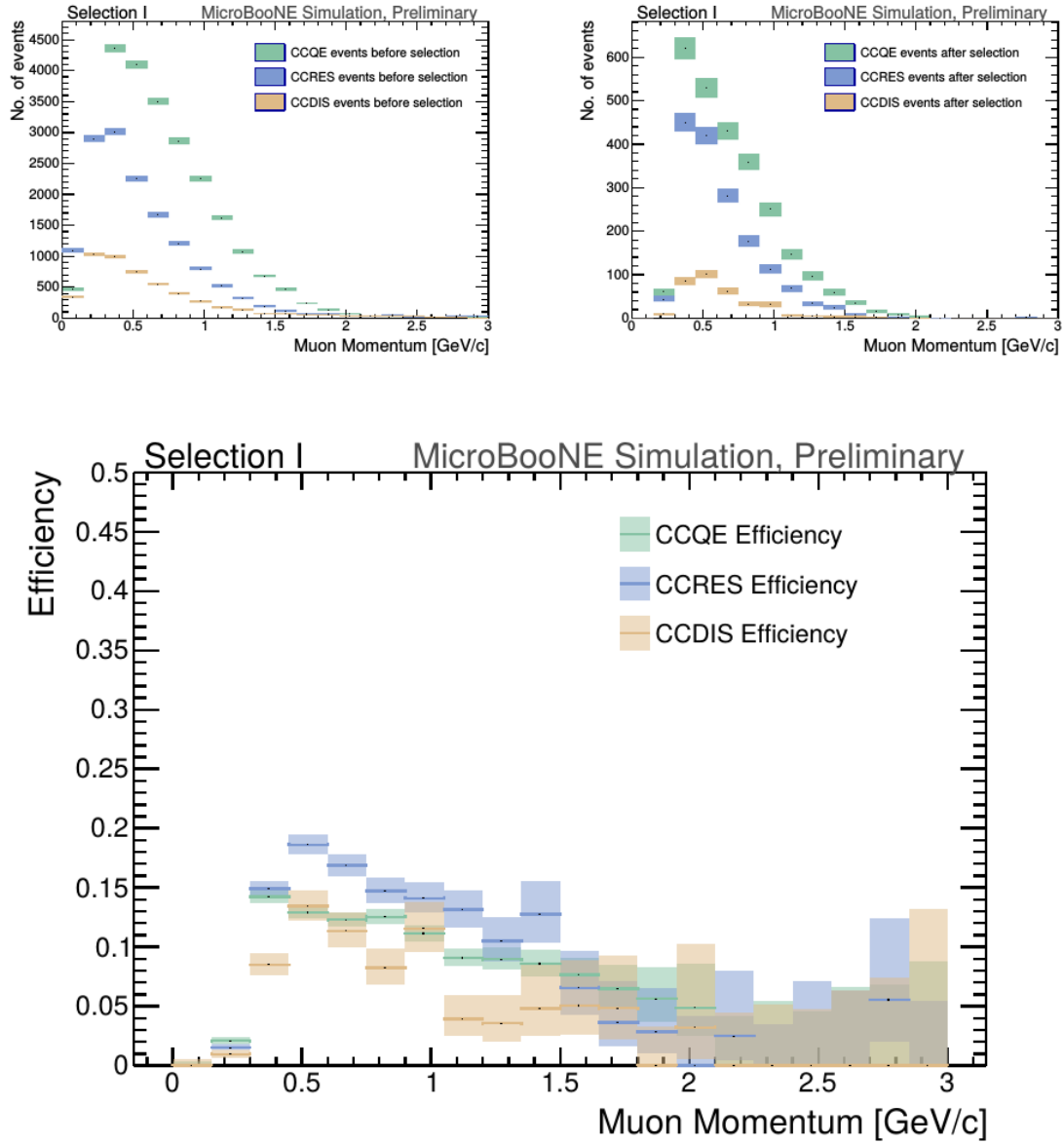


Figure 5.9: MC momentum distributions of the muon originating from a ν_μ CC interaction. Upper left is the momentum distributions of events with a vertex within the FV split up into CCQE (red), CCRES (yellow), and CCDIS (green) before selection. The upper right side is the momentum distribution after the selection with the same color schemes. The lower plot is the selection efficiencies for all three interaction types. The definition of QE, RES, and DIS is based on GENIE.

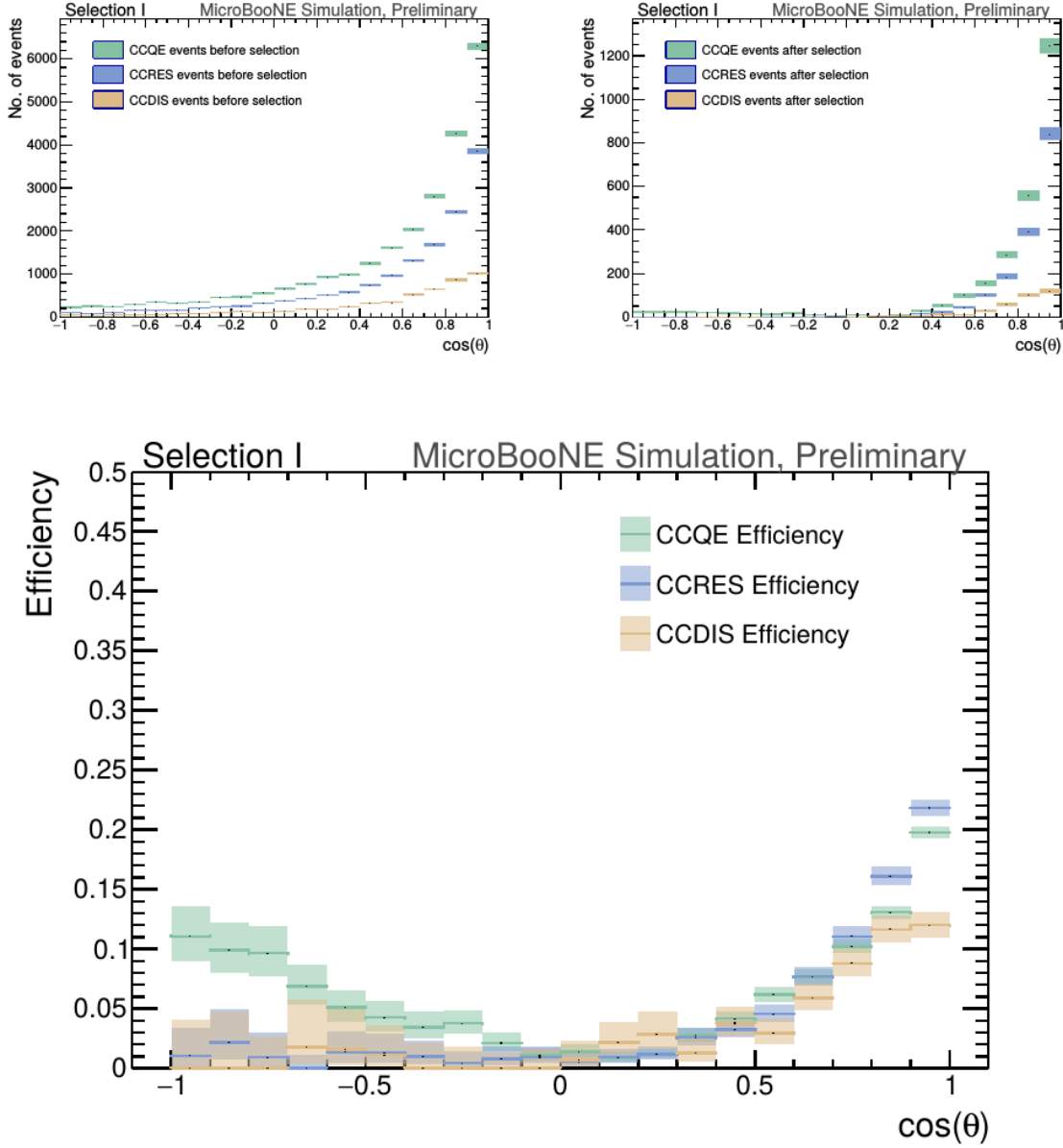


Figure 5.10: MC $\cos(\theta)$ distributions of the muon originating from a ν_μ CC interaction. Upper left is the $\cos(\theta)$ distributions of events with a vertex within the FV split up into CCQE (red), CCRES (yellow), and CCDIS (green) before selection. The upper right side is the $\cos(\theta)$ distribution after the selection with the same color schemes. The lower plot is the selection efficiencies for all three interaction types. The definition of QE, RES, and DIS is based on GENIE.

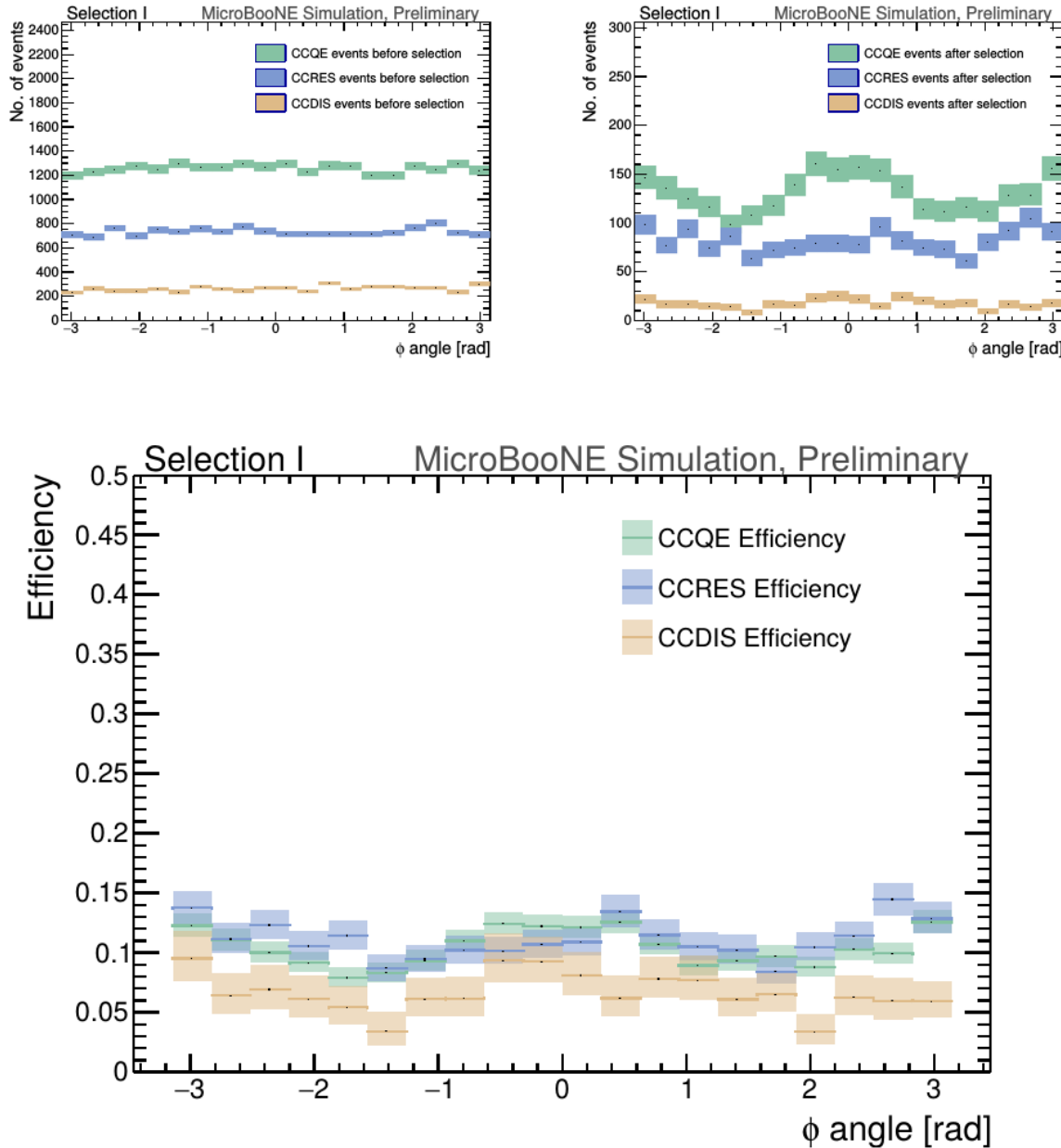


Figure 5.11: MC ϕ distributions of the muon originating from a ν_μ CC interaction. Upper left is the ϕ distributions of events with a vertex within the FV split up into CCQE (red), CCRES (yellow), and CCDIS (green) before selection. The upper right side is the ϕ distribution after the selection with the same color schemes. The lower plot is the selection efficiencies for all three interaction types. The definition of QE, RES, and DIS is based on GENIE.

¹³³⁴ Chapter 6

¹³³⁵ **Background on Convolutional Neural Networks**

¹³³⁷ Convolutional neural networks (CNNs) have been one of the most influential innovations in the field of computer vision. Neural networks became popular in 2012 ¹³³⁸ when Alex Krizhevsky used them to win that year's ImageNet competition [?] by ¹³³⁹ dropping the error from 26% to 15%. Since then, many companies are using deep ¹³⁴⁰ learning including Facebook's tagging algorithms, Google for their photo search and ¹³⁴¹ Amazon for product recommendations. For the purpose of this thesis CNNs were ¹³⁴² used for image classification, specifically, images of varying particles created using ¹³⁴³ LArTPC data.

¹³⁴⁵ **6.1 Image Classification**

¹³⁴⁶ Image classification is the process of inputting an image into the CNN and receiving a ¹³⁴⁷ probability of classes that best describes what is happening in the image. As humans, ¹³⁴⁸ image classification is something that is learned at a very young age and is easy to ¹³⁴⁹ do without much effort. This is also apparent when hand-scanning LArTPC images. ¹³⁵⁰ After learning what a neutrino event looks like in MicroBooNE, it is relatively easy ¹³⁵¹ to recognize simple neutrino events from cosmic ray background as well as highly ¹³⁵² ionizing particles like protons from minimum ionizing particles like muons. The very ¹³⁵³ detailed images LArTPC detectors output are prime candidates for input images into ¹³⁵⁴ a CNN. CNNs mimic a human's ability to classify objects by creating an architecture ¹³⁵⁵ that can learn differences between all the images it's given as well as figure out the

1356 unique features that make up each object. CNNs are modeled after the visual cortex.
1357 Hubel and Wiesel [?] found that there are small regions of neuronal cells in the brain
1358 that respond to specific regions of the visual field. They saw that some neurons fired
1359 when exposed to vertical edges while others fired when shown horizontal or diagonal
1360 edges. They also saw that these neurons were organized in columns. The idea of
1361 specific neurons inside of the brain firing to specific characteristics is the basis behind
1362 CNNs.

1363 6.2 CNN Structure

1364 When used for image recognition, convolutional neural networks consist of multiple
1365 layers that extract different information on small portions of the input image. How
1366 many layers is tunable to increase the accuracy. The output of these collections are
1367 then tiled so that they overlap to gain a better representation of the original image
1368 and allow for translation. The first of these layers is always a convolution layer. To
1369 the CNN, an image is an array of pixel values. For a RGB color image with width
1370 and height equal to 32x32 the corresponding array is 32x32x3. Filters, also known as
1371 neurons, of any size set by the user is then convolved with the receptive field of the
1372 image. If the filter is 5x5, the receptive field will be a patch of 5x5 on the input image.
1373 The filter is also an array of numbers called weights. The convolution of the filter and
1374 image are matrix multiplications of the weights and the pixel values. By stepping the
1375 receptive field by 1 unit, for an input image of 32x32x3 and a filter of 5x5x3 you'd get
1376 an output array of 28x28x1. This output array is called an activation map or feature
1377 map. The use of more filters preserves the spatial dimensions better. The filters can
1378 be described as feature identifiers. Examples of features in an image consist of edges,
1379 curves, and changes in colors. The first filters in a CNN will primarily be straight
1380 line and curve feature identifiers. An example of a curve filter is shown in figure 6.2.
1381 When a curve in the same concavity is found in the input image, the corresponding
1382 pixel in the output feature map will be activated. Going back to our example of a
1383 32x32 input image and a 5x5 filter, if there were to be a curve in the top left corner
1384 of the input image, our output feature map would have a high pixel value in the top
1385 left. Therefore, feature maps tell us where a specific feature is located in the original
1386 image. Figure ?? shows a visualization of filters found in the first layers of many CNN
1387 architectures. These filters in the first layer convolve around the image and activate
1388 when the specific feature it is looking for is in the receptive field.

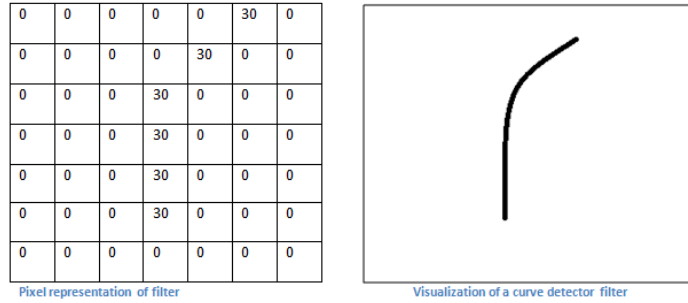


Figure 6.1: Pixel representation and visualization of a curve detector filter. As you can see, in the pixel representation, the weights of this filter are greater along a curve we are trying to find in the input image

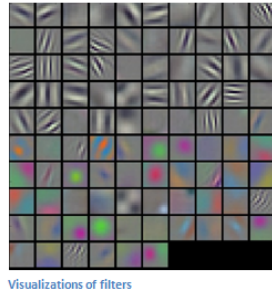


Figure 6.2: Visualization of filters found in first layer of a CNN.

In figure 6.3 you can see how an edge detection filter is used to save only necessary information for recognizing different types of clothes. You can also see by having multiple filters you can get more detail or less detail from an image which can then simplify or complicate the object recognition task. Being able to distinguish between a shirt or a leg garment is as much information you want, having a filter that extracts outline edge or shape information would be all that you need. But if instead you wanted to distinguish between a formal cocktail dress or a summer dress, more information would need to be saved equating to many more filters for one image. Rather than trying to come up with how many filters and what features are important for detection, CNNs do this automatically. CNNs take input parameters, called hyperparameters, for example number of layers, number of filters per layers, number of weights per filter, and uses these to create the output feature maps. The layers build upon each-other, for example if we were creating a CNN for facial recognition the convolutional layers will start learning feature combinations off of the previous layers. The low level features like edges, gradients, and corners of the first layers become high level features like eyes, noses, and hairs. This process is visualized in figure 6.4



Figure 6.3: Applying a feature mask over a set of fashion items to extract necessary information for auto-encoding. Unnecessary information for example color or brand emblems are not saved. This feature map is an edge detection mask that leaves only shape information which helps to distinguish between different types of clothes.

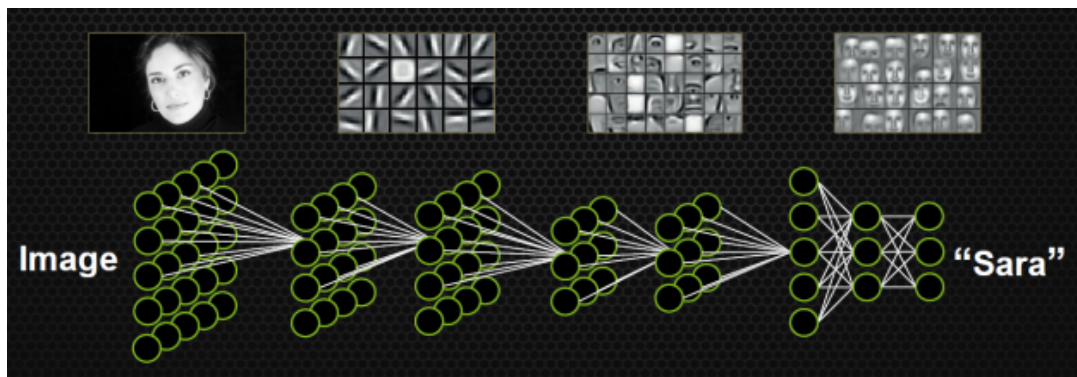


Figure 6.4: Pictorial Representation of Convolutional Neural Networks as well as a visual representation on CNN's complexity of layer feature extraction

1405 There are other layers in a CNN architecture that will not be covered in the scope
 1406 of this thesis but in a general sense, these layers are interspersed between convolution
 1407 layers to preserve dimensionality and control overfitting of the network. The last layer
 1408 is called a fully connected layer and it's job is to output an N dimensional vector where
 1409 N is the number of classes the network has been trained on. Each number in this vector
 1410 represents the probability that the input image is a certain class. Fully connected layers
 1411 use the feature maps of the high level features to compute the products between the
 1412 weights of the previous layer to get the probabilities of each class. These weights are
 1413 then adjusted through the training process using backpropagation.

¹⁴¹⁴ 6.2.1 Backpropagation

¹⁴¹⁵ A CNN at it's onset has weights that are randomized. The filters themselves don't
¹⁴¹⁶ know how to pull out identifying information per class. For a neural network to learn,
¹⁴¹⁷ it must be trained on a training set that is labeled. Backpropagation has four seperate
¹⁴¹⁸ steps: foward pass, loss function, backward pass and updating weights. In the forward
¹⁴¹⁹ pass, a training image is passed through the whole network. All of our weights at this
¹⁴²⁰ time are randomly initialized so the output for the first image will have no preference
¹⁴²¹ to a specific class. A common loss function is mean squared error (MSE):

$$E_{total} = \sum \frac{1}{2} (actualclass - predictedclass)^2 \quad (6.1)$$

¹⁴²² If we assume that the MSE is the loss of our CNN, the goal would be that our
¹⁴²³ predicted label (output of CNN) is the same as our training label. To do this, we need
¹⁴²⁴ to minimize the loss function. To do this, it is necessary to find out which weights most
¹⁴²⁵ directly affect the loss of the network i.e $\frac{dL}{dW}$ where L is our loss function and W are
¹⁴²⁶ the weights of a specific layer. The next step is the backward pass which determines
¹⁴²⁷ which weights contribute the most to the loss and finds ways to adjust these weights
¹⁴²⁸ so that the loss decreases. After the derivative is computed, the last step updates the
¹⁴²⁹ weights in the opposite direction of the gradient.

$$w = w_i - \eta \frac{dL}{dW} \quad (6.2)$$

$$w = \text{Weight} \quad (6.3)$$

$$w_i = \text{Initial Weight} \quad (6.4)$$

$$\eta = \text{Learning Rate} \quad (6.5)$$

¹⁴³⁰ The learning rate is a parameter given to the CNN and it describes the steps the
¹⁴³¹ network takes to update the weights. Higher learning rate equals large steps and a
¹⁴³² lower training time, but a learning rate that is too large can mean the CNN never
¹⁴³³ converges.

¹⁴³⁴ Going through backpropagation consists of one training iteration. Once the net-
¹⁴³⁵ work completes a specific number of iterations, another parameter given, and runs
¹⁴³⁶ over all training images that are split up into batches, the process is considered com-
¹⁴³⁷ plete. User input parameters, called hyperparameters, help the network converge to

₁₄₃₈ optimal weights for each layer. Batch size, learning rate, and training iteration are just
₁₄₃₉ some of the user input hyperparameters that help. Lastly, to check if the network has
₁₄₄₀ learned, a different set of labeled images are fed to the CNN iteratively through the
₁₄₄₁ training process to see how well it's learning. This process is especially important to
₁₄₄₂ make sure the network architecture isn't being affected by overfitting (memorizing
₁₄₄₃ training input rather than learning).

₁₄₄₄ 6.3 Choosing Hyperparameters

₁₄₄₅ Convolutional neural networks are a relatively new tools in computer vision. Choosing
₁₄₄₆ hyperparameters for your specific dataset is a non-trivial task. Hyperparameters can
₁₄₄₇ range from the amount of layers and filters per layer in an CNN architecture to the
₁₄₄₈ stride the receptive field of a filter takes, not to mention training hyperparameters
₁₄₄₉ such as learning rate and batch size described above. They're ways to optimize these
₁₄₅₀ hyperparameters via hyperparameter optimization using Bayesian Optimization [?]
₁₄₅₁ but as you can imagine, optimizing an CNN architecture from scratch can be very
₁₄₅₂ computationally intensive. For the purpose of this thesis, two well known CNN
₁₄₅₃ architectures were used, AlexNet [?], which won the ImageNet Large-Scale Visual
₁₄₅₄ Recognition Challenge (ILSVRC) in 2012 and therefore bringing awareness of CNNs,
₁₄₅₅ and GoogleNet [?], which won the ILSVRC in 2014, giving rise to deep networks. Both
₁₄₅₆ AlexNet and GoogleNet architectures were used to train on LArTPC images and their
₁₄₅₇ low level filter weights. Higher level filter weights were randomly initialized before
₁₄₅₈ training so the network can learn high level features of LArTPC image classes. The
₁₄₅₉ AlexNet architecture is shown in figure 6.5 and the GoogleNet architecture is shown
₁₄₆₀ in figure 6.6

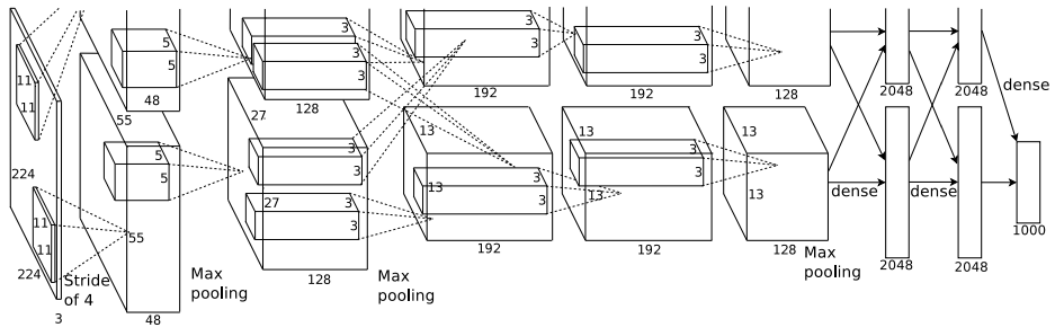


Figure 6.5: Pictoral representation of the AlexNet model. The AlexNet model consists of 5 convolution layers and 3 fully connected layers.

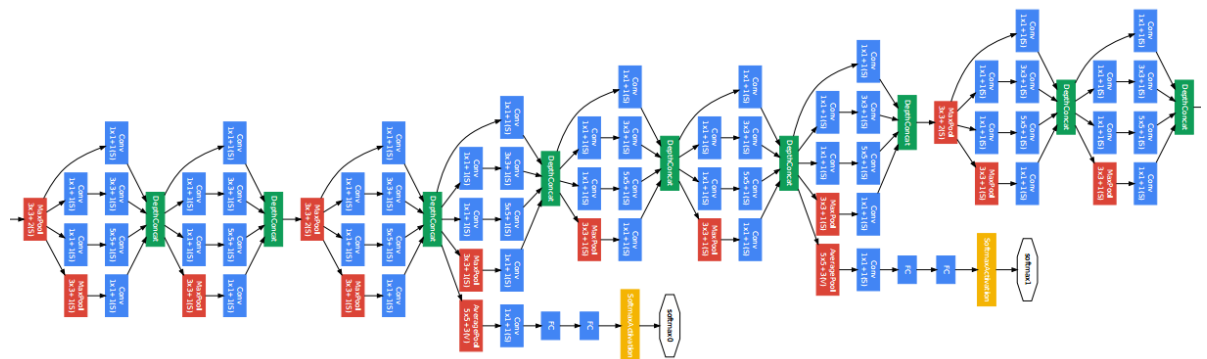


Figure 6.6: Pictoral representation of the GoogleNet model. The GoogleNet model consists of 22 layers. The model implements 9 Inception modules which performs covolution and pooling in parallel and strays away from the basis that CNN layers need to be stacked up sequentially. The GoogleNet model also doesn't use fully connected layers, instead it uses average pooling which greatly reduces the amount of parameters. GoogleNet has 12x fewer parameters than AlexNet.

¹⁴⁶¹ Chapter 7

¹⁴⁶² Training process of Convolutional ¹⁴⁶³ Neural Networks

¹⁴⁶⁴ Three Convolutional Neural Networks (CNNs) were trained throughout this analysis.
¹⁴⁶⁵ There are differences to each CNN and will be described fully in the next sections but
¹⁴⁶⁶ the main difference are the amount of particle images used for training and validation.
¹⁴⁶⁷ CNN1075 used 1,075 muons and 1,075 pions for training and the same amount of
¹⁴⁶⁸ each particle for validation. CNN10000 used 10,000 muons and 10,000 pions split in
¹⁴⁶⁹ half for testing and training. Lastly CNN100000 had muons, pions, protons, electrons,
¹⁴⁷⁰ and gammas in it's training and validation set. Each particle had 20,000 images and
¹⁴⁷¹ training and validation was split 90% training, 10% validation. This chapter will also
¹⁴⁷² describe the different hardware frameworks used for training beginning on a CPU
¹⁴⁷³ and ending on a GPU cluster.

¹⁴⁷⁴ 7.1 Hardware Configurations for Convolutional Neural ¹⁴⁷⁵ Network Training

¹⁴⁷⁶ The first training iteration, CNN1075, was a proof of concept. This CNN was trained
¹⁴⁷⁷ on my local machine for \sim 4-5 weeks. The batch size had to be very small as well as the
¹⁴⁷⁸ image size due to the lack of computation resources. The second iteration of training,
¹⁴⁷⁹ CNN10000, was trained on a Fermilab stationed Syracuse University machine. This
¹⁴⁸⁰ machine had 6 TB of disk space, 6 cores at 2.1 GHz and 32 GB of RAM. The use of
¹⁴⁸¹ this machine allowed me to increase the training sample as well as the batch size and
¹⁴⁸² hence further increase the accuracy of the neural network. Lastly, the CNN100000 was

¹⁴⁸³ trained using two GTX 1080 Ti GPUs with 11GB of memory on a node on the Syracuse
¹⁴⁸⁴ University GPU cluster, SUrge, that has 8 cores and 16GB of memory. This increase in
¹⁴⁸⁵ memory as well as the capability to use 2 GPUs drastically cut down on training time
¹⁴⁸⁶ from \sim 4-5 weeks to \sim 8 hours. SUrge also allowed for hyperparameter optimization
¹⁴⁸⁷ by being able to run multiple training iterations over the two GPUs. Lastly, SUrge
¹⁴⁸⁸ allowed for training over higher resolution images and a larger particle class of 5
¹⁴⁸⁹ particles vs 2 particles.

¹⁴⁹⁰ **7.2 Creating images using LArTPC data for
¹⁴⁹¹ training/validation of CNNs**

¹⁴⁹² The μ/π image dataset used to train and validate CNN1075 was created using single
¹⁴⁹³ generated isotropic muons and pions from 0-2 GeV energy range. 2,150 muons and
¹⁴⁹⁴ 2,150 pions were used for training and testing split 50%. The images were created
¹⁴⁹⁵ using LArSoft, a liquid argon software, and were based on wire number and time
¹⁴⁹⁶ tick in the collection plane. Uboonecode reconstruction version v05_08_00 was used.
¹⁴⁹⁷ The raw ADC value after noise filtering was the wire signal. Each collection plane
¹⁴⁹⁸ greyscale image was 3456x1600x1 where 6 time ticks were pooled into 1 bin.

¹⁴⁹⁹ After the image was created, the region of interest (ROI) in the image was found by
¹⁵⁰⁰ using Open CV, a image processing open source software package, to scan the image
¹⁵⁰¹ starting from the edges and stopping once a bright pixel is encountered. At this step,
¹⁵⁰² the ROI can be larger or smaller than the necessary size of a training image and the XY
¹⁵⁰³ ratio of the image is not kept. This ROI is then resized to an image of 224x224x1.

¹⁵⁰⁴ The greyscale color standard is 8bit therefore the ADC value of wire and time tick
¹⁵⁰⁵ was also downsampled due to the 12bit ADC value MicroBooNE has. To do this,
¹⁵⁰⁶ the highest ADC pixel in the image was found and then this was divided by the rest
¹⁵⁰⁷ placing all pixel values between 0-1. From there, all pixel values are then multiplied
¹⁵⁰⁸ by 255.

¹⁵⁰⁹ The μ/π image dataset used to train and validate the CNN10000 was also created
¹⁵¹⁰ using single generated isotropic muons and pions from 0-2 GeV energy range. 10,000
¹⁵¹¹ muons and 10,000 pions were used for training and testing split 50%. Uboonecode
¹⁵¹² v06_23_00 was used instead of v05_08_00. Each collection plane greyscale image was
¹⁵¹³ 3456x1280x1 where 5 time ticks were pooled into 1 bin which is different than the

1514 previous dataset and was implemented due to the fact that the time ticks of an event
1515 went from 9400 to 6400 with the change of uboonecode version. Issues that arose in
1516 CNN1075 that were fixed in CNN10000 include zero-padding images in X and Y that
1517 are smaller than 224X224 to eliminate over-zooming effect and fixing a bug that shifted
1518 pixels separated by a dead-wire region.

1519 The $\mu/\pi/p/e/\gamma$ image dataset used to train and validate the CNN100000 were
1520 created using single generated isotropic particles with energy range from 0-2 GeV.
1521 20,000 of each particle were used for training and were split 90/10 between training
1522 and testing sets. Uboonecode v06_23_00 was used for these images. The collection
1523 plane greyscale iamge had the same dimensions as CNN10000, 3456x1280x1 and the
1524 ROI algorithm was the same except for resizing these images to 576x576.

1525 A major change other than the higher resolution images was the treatment of the
1526 ADC values. In the first two image making schemes, the highest pixel value was found
1527 per image and the image was then normalized by that. The issue arising from this
1528 ADC normalization wasn't inherent in μ/π training due to the fact that both particles
1529 are minimum ionizing particles in liquid argon, however, when dealing with a larger
1530 particle class, it was necessary to try and make sure energy deposition by each particle
1531 was preserved. The energy deposition in a particle image corresponds to the ADC
1532 value or pixel brightness. To preserve energy deposition, the ADC float value was
1533 passed straight to the image rather than doing any image normalization. This then
1534 makes sure that minimum ionizing particles like muons and pions appear dimmer
1535 than highly ionizing particles like protons.

1536 Images were also made from BNB+Cosmic events that passed the cc-inclusive
1537 selection 1 filter right before the 75 cm track length cut and were classified using
1538 the CNN10000. The dataset used to create these images is the same one used in
1539 [?], *prodgenie_bnb_nu_cosmic_uboone_mcc7_reco2*. These images were created using
1540 information from the track candidate that passed the filter. Only wire number and
1541 time ticks associated to the track candidate were drawn on the image to mimic a single
1542 particle generated image.

1543 These images were then classified using CNN10000. Two approaches were taken
1544 in making these images. The first was using the image normalization above where
1545 the maximum pixel in each image is used as a normalization constant to get all pixels
1546 between 0-1 then multiply all pixels by 255. As described above, this is the incorrect

¹⁵⁴⁷ way to normalize. The second way the images were created was by passing the ADC
¹⁵⁴⁸ float to the image. The results of CNN10000 performance are shown in section [7.1](#).

¹⁵⁴⁹ Lastly, multiple BNB+Cosmic images per event were made for CNN100000 by
¹⁵⁵⁰ reducing many of selection I cuts to try and let the CNN do particle as well as event
¹⁵⁵¹ identification. This image making scheme used for CNN100000 will be described in
¹⁵⁵² more detail in later sections.

¹⁵⁵³ 7.3 Convolutional Neural Network Training

¹⁵⁵⁴ 7.3.1 Training CNN1075

¹⁵⁵⁵ The results of CNN1075 are described in this section. The accuracy is how well
¹⁵⁵⁶ CNN1075 is doing by epoch and was 74.5%. The loss is gradient descent or mini-
¹⁵⁵⁷ mization of the error of the weights and biases used in each neuron of each layer of
¹⁵⁵⁸ CNN1075 and was 58% with a trend sloping downwards on the loss curve as well as a
¹⁵⁵⁹ trend sloping upward in the accuracy curve. The accuracy and loss of CNN1075 are
¹⁵⁶⁰ shown in figure [7.1](#). Due to the depth of the neural network framework, it was neces-
¹⁵⁶¹ sary to train with a larger dataset and for more epochs, however, the downward slope
¹⁵⁶² of the loss curve is an indication that once trained for longer with a higher training
¹⁵⁶³ sample, neural networks can be used for μ/π separation. The hyperparameters used
¹⁵⁶⁴ to train CNN1075 are detailed below:

- ¹⁵⁶⁵ • *train_batch_size*: 50 ¹⁵⁷⁰ • *lr_policy*: "step" ¹⁵⁷⁵ • *momentum*: 0.9
- ¹⁵⁶⁶ • *test_batch_size*: 50 ¹⁵⁷¹ • *gamma*: 0.1 ¹⁵⁷⁶ • *weight_decay*: 0.0005
- ¹⁵⁶⁷ • *test_iter*: 50 ¹⁵⁷² • *stepsize*: 200 ¹⁵⁷⁷ • *snapshot*: 100
- ¹⁵⁶⁸ • *test_interval*: 50 ¹⁵⁷³ • *display*: 50
- ¹⁵⁶⁹ • *base_lr*: 0.01 ¹⁵⁷⁴ • *max_iter*: 5000

¹⁵⁷⁸ The confusion matrices shown in figure [7.2](#) show the accuracy for both the training
¹⁵⁷⁹ and testing datasets. The fact that these two have similar accuracies is important
¹⁵⁸⁰ because if the training dataset had a much higher accuracy, that indicates an over-
¹⁵⁸¹ training of the training sample which means the neural network didn't learn features
¹⁵⁸² to separate muons from pions, it just memorized what was in the training dataset.

Loss/Accuracy of CNN trained on 2150 images

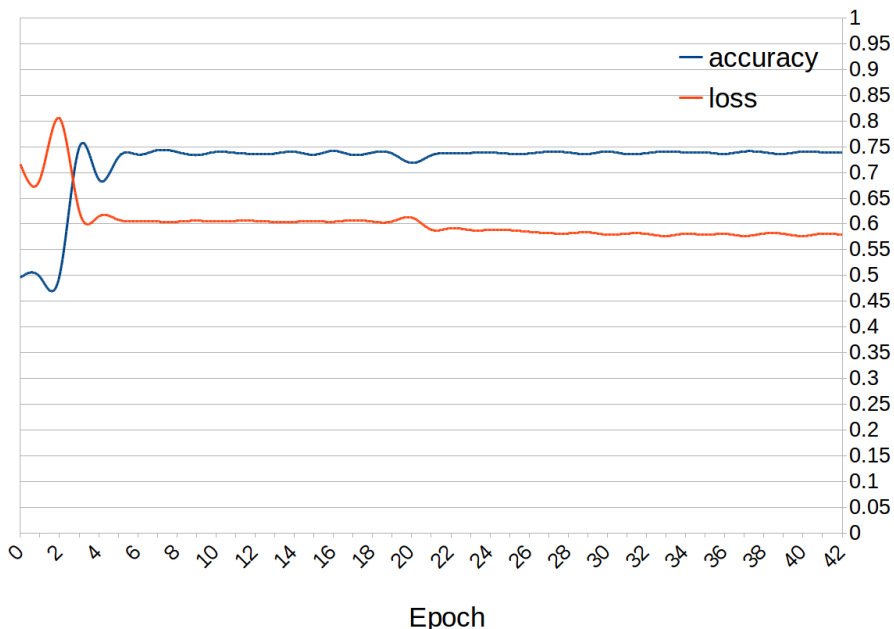
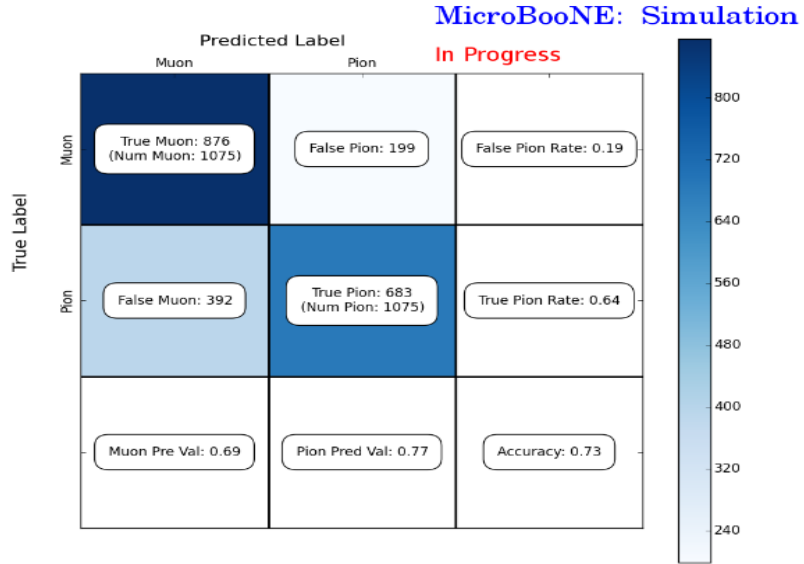
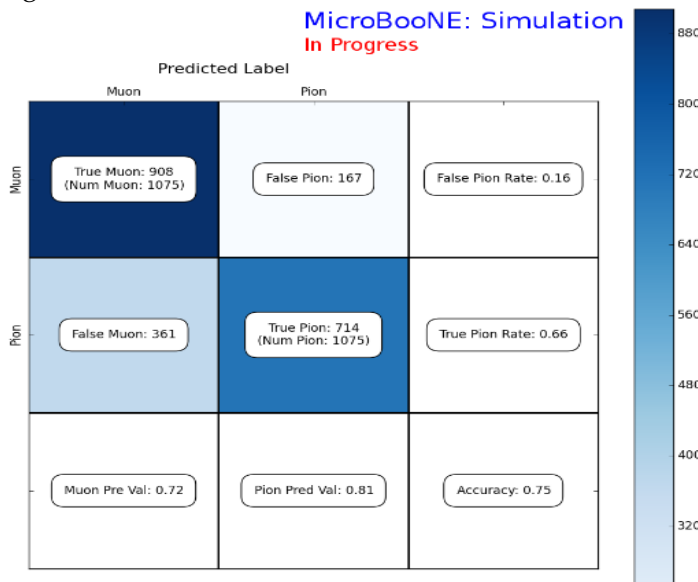


Figure 7.1: Accuracy vs. Loss of AlexNet 2-output μ/π sample consisting of 2,150 images each.



(a) Confusion Matrix showing Accuracy of CNN1075 using training MC data



(b) Confusion Matrix showing Accuracy of CNN1075 using testing MC data

Figure 7.2: Description of confusion matrix variables: False pion rate = $false\pi / total\pi$ True pion rate = $true\pi / total\pi$ Accuracy = $(true\pi rate + true\mu rate) / 2$ Pion prediction value = $true\pi / (true\pi + false\pi)$ Muon prediction value = $true\mu / (true\mu + false\mu)$

1583 Also note that the neural network does a better job of identifying muons than pions.
1584 This can be attributed to the more complex event scenes pions tend to leave in the
1585 detector due to pion interacting more in LAr than muons do. The CNN may do better
1586 at identifying pions with a larger training sample.

1587 7.3.2 Training CNN10000

1588 The hyperparameters used for CNN10000 are shown below. The batch size for the
1589 training and testing as well as the test_iter were chosen to encompass the whole
1590 training/testing image set when doing accuracy/loss calculations. To do this, multi-
1591 pling the test_iter by the test batch size gives you the amount of images used when
1592 calculating accuracy/loss curves.

- 1593 • *train_batch_size*: 100₁₅₉₈ • *lr_policy*: "step"₁₆₀₃ • *momentum*: 0.99
- 1594 • *test_batch_size*: 100₁₅₉₉ • *gamma*: 0.1₁₆₀₄ • *weight_decay*: 0.0005
- 1595 • *test_iter*: 100₁₆₀₀ • *stepsize*: 1000₁₆₀₅ • *snapshot*: 100
- 1596 • *test_interval*: 100₁₆₀₁ • *display*: 100
- 1597 • *base_lr*: 0.001₁₆₀₂ • *max_iter*: 10000

1606 The same architecture that was used to train CNN1075 was employed on CNN10000,
1607 AlexNet. Caffe [?] was the software package used for both CNNs. The differences
1608 include batch size and test_iter and momentum to account for the larger dataset. Fig-
1609 ure 7.3 shows the loss and accuracy of CNN10000. There is around a 10% increase in
1610 accuracy from CNN1075 to CNN10000, 85%, and around a 20% decrease in loss, 36%.

1611 Figure 7.4 show a breakdown of μ/π separation for CNN10000. It also shows
1612 the network is not being over-trained due to the Accuracy of both the training and
1613 testing datasets being within .01% of each-other. Figure 7.5 shows how well the neural
1614 network is doing at μ/π separation with respect to muon probability. The red bins
1615 corresponds to true pions and the blue bins correspond to true muons. There is
1616 still pion contamination in the high muon probability bins but by choosing a muon
1617 probability of $\geq 80\%$ we can reduce this. The CNNs increase in total accuracy can be
1618 attributed to an increase in accurately classifying pions as pions as seen in both the
1619 confusion matrix in figure 7.4 and the large number of events in the zero bin of the
1620 muon probability plot seen in figure 7.5 that corresponds to high probability pions.

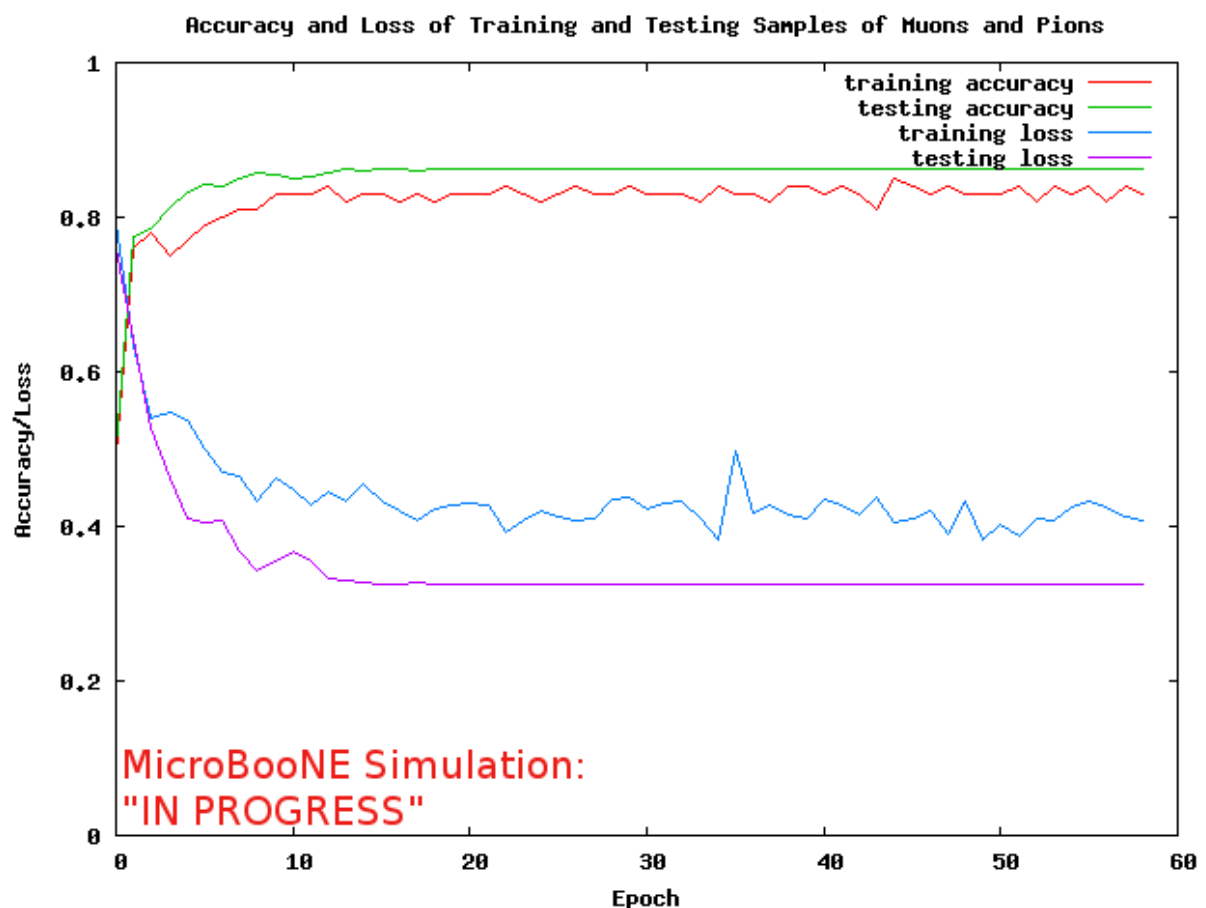
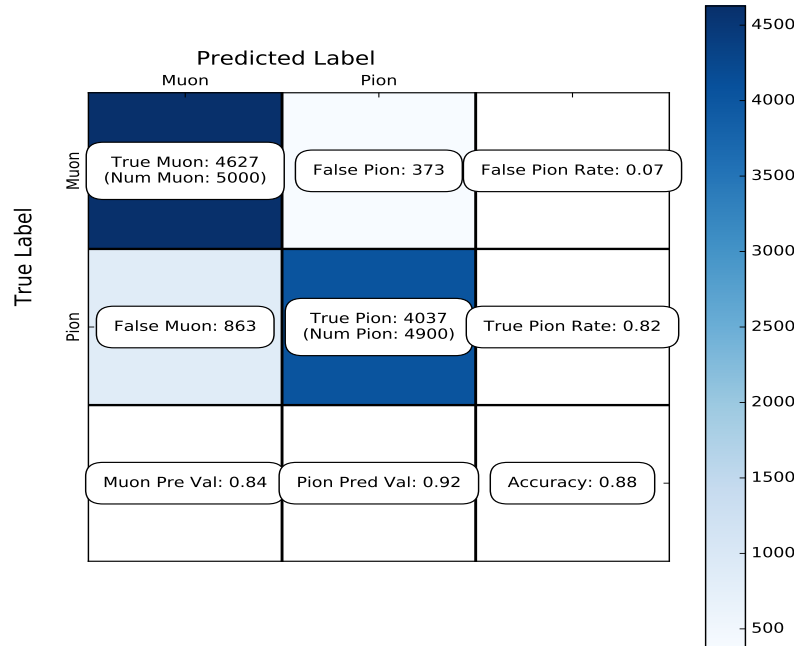
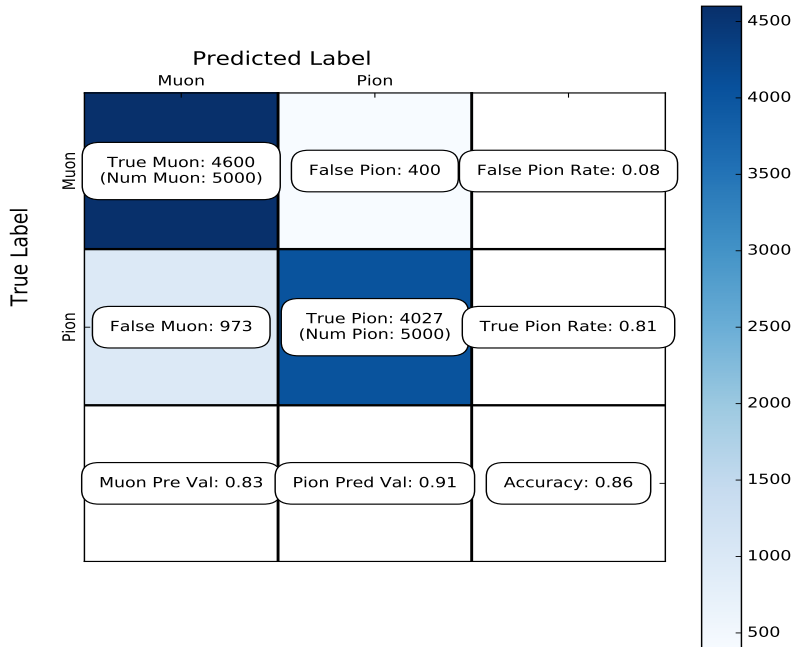


Figure 7.3: Accuracy vs. Loss of AlexNet 2-output μ/π sample consisting of 10,000 images each.



(a) Confusion Matrix showing Accuracy of CNN10000 using training MC data



(b) Confusion Matrix showing Accuracy of CNN10000 using testing MC data

Figure 7.4: Description of confusion matrix variables: False pion rate = $false\pi / total\pi$; True pion rate = $true\pi / total\pi$; Accuracy = $(true\pi rate + true\mu rate) / 2$; Pion prediction value = $true\pi / (true\pi + false\pi)$; Muon prediction value = $true\mu / (true\mu + false\mu)$

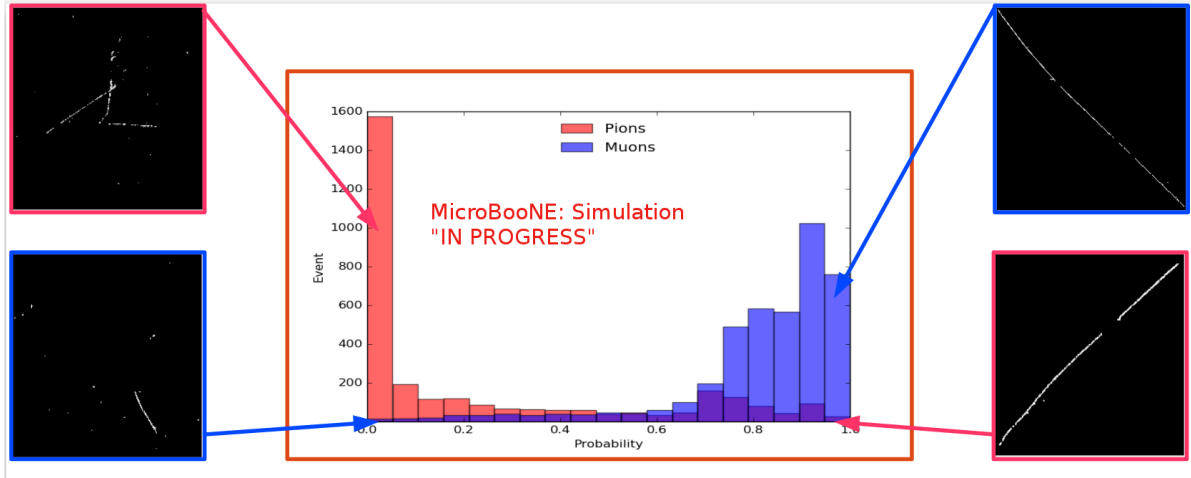


Figure 7.5: Probability plot of muons and pions from testing set. Images surrounding histogram are a random event from lowest bin and highest bin for each particle.

1621 7.3.3 Training CNN100000

1622 CNN100000 used the GoogleNet architecture rather than the AlexNet architecture
 1623 used in the two previous trained CNNs. This is the first time the neural network was
 1624 trained on a larger particle class, $\mu/\pi/p/\gamma/e$, and on higher resolution images. This
 1625 CNN also employed GPUs during the training process. The hyperparameters are
 1626 shown below:

- 1627 • *train_batch_size*: 18 1632 • *lr_policy*: "step" 1637 • *max_iter*: 10000
- 1628 • *test_batch_size*: 2 1633 • *gamma*: 0.96 1638 • *momentum*: 0.99
- 1629 • *test_iter*: 2000 1634 • *stepsize*: 10000 1639 • *weight_decay*: 0.0002
- 1630 • *test_interval*: 2000 1635 • *average_loss*: 40 1640 • *snapshot*: 50000
- 1631 • *base_lr*: 0.001 1636 • *display*: 40

1641 The accuracy and loss for CNN100000 are shown in figures 7.6 and 7.7. The jumps
 1642 shown in both figures are when the training was stopped to fine-tune the weight decay
 1643 and the learning rate. The accuracy leveled off at $\sim 80\%$ and the loss was at ~ 0.48 .

1644 Figure 7.8 shows the confusion matrix of CNN100000. The proton identification of
 1645 the neural network is at 85% and the highest out of all five particles. One thing to note
 1646 is clear separation between particles that leave track like objects in the MicroBooNE
 1647 detector, $\mu/\pi/p$, versus particles that leave shower like objects in MicroBooNE, e/γ .

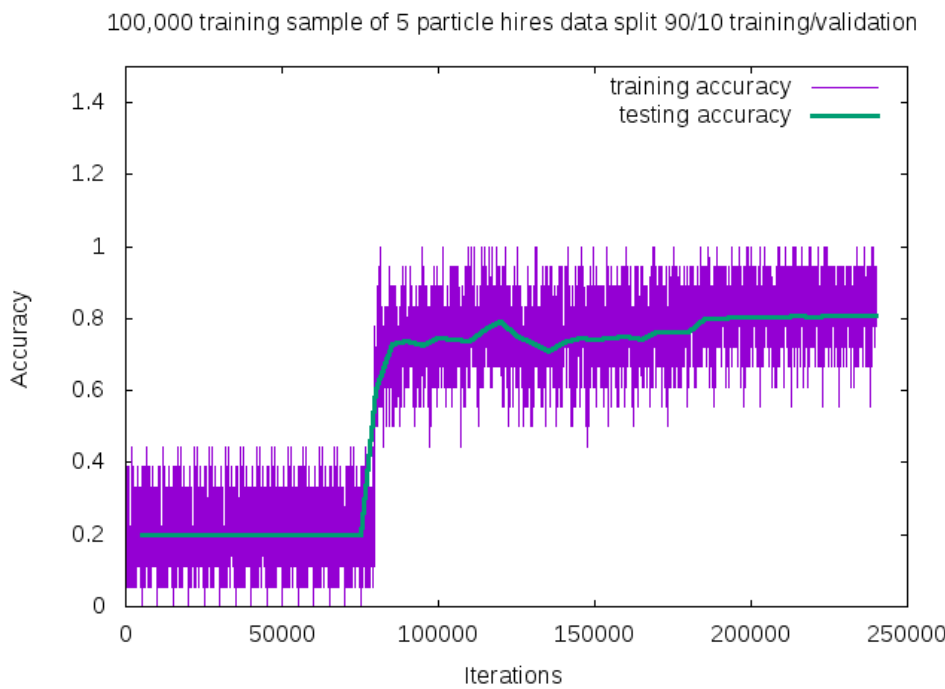


Figure 7.6: Training and testing accuracy of CNN trained on 100,000 images of $\mu/\pi/p/\gamma/e$ with 20,000 images of each particle. Each image was a size of 576x576 and the images per particle were split 90% use for training and 10% used for testing the network

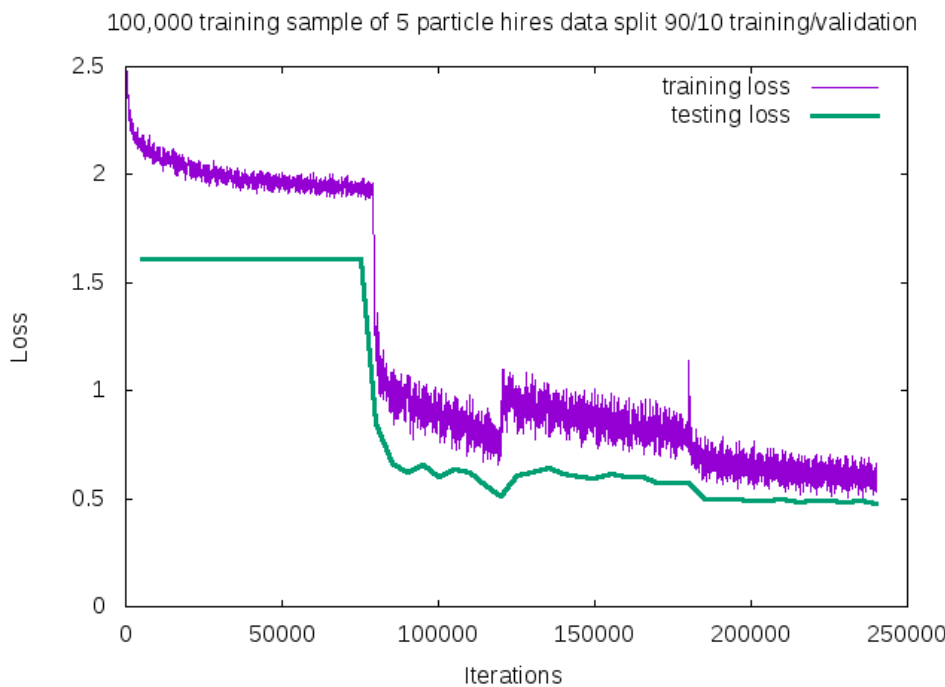


Figure 7.7: Training and testing loss of CNN trained on 100,000 images of $\mu/\pi/p/\gamma/e$

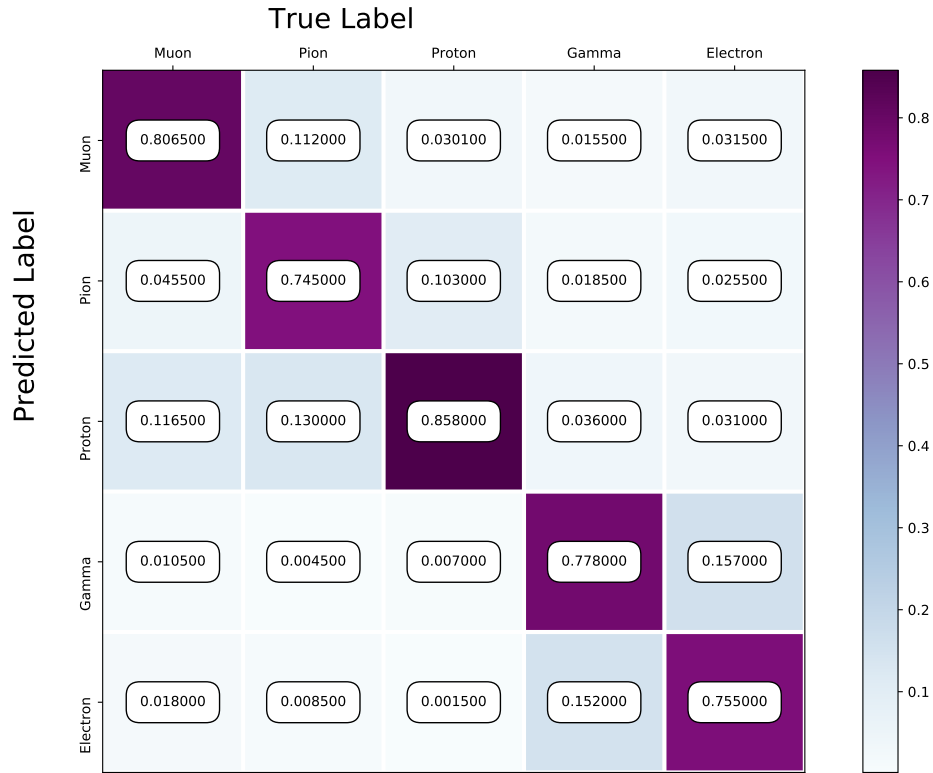


Figure 7.8: Confusion Matrix of all five particles

1648 Another visualization of how the neural network is learning is shown in 7.9. t-
 1649 SNEs [?] is a technique used for dimensionality reduction developed for use in vi-
 1650 sualizing high-dimensional datasets. Each datapoint is given a location in a two
 1651 or three-dimensional map by using stochastic neighbor embedding to convert high-
 1652 dimensional euclidean distances between datapoints into conditional probabilities that
 1653 represent the similarities between these datapoints. For datapoints close together on
 1654 the map, their conditional probabilities are high, for datapoints with a wide separation
 1655 between them, their conditional probabilities are very small. Figure 7.9 is a t-SNE of
 1656 the final training iteration of a subset of the training sample used in CNN100000. You
 1657 can see a clear separation between track like objects and shower like objects. You can
 1658 also see that electrons and gammas are not as separated as muons, pions, and protons.
 1659 For the purpose of this thesis, this isn't an issue but later iterations of training could
 1660 include more images for the gamma and electron classes to help the CNN further
 1661 separate these classes.

1662 Figure 7.10 shows the probability of each particle class and the highest probability
 1663 misidentification for each class. For muons, the largest misidentification is from

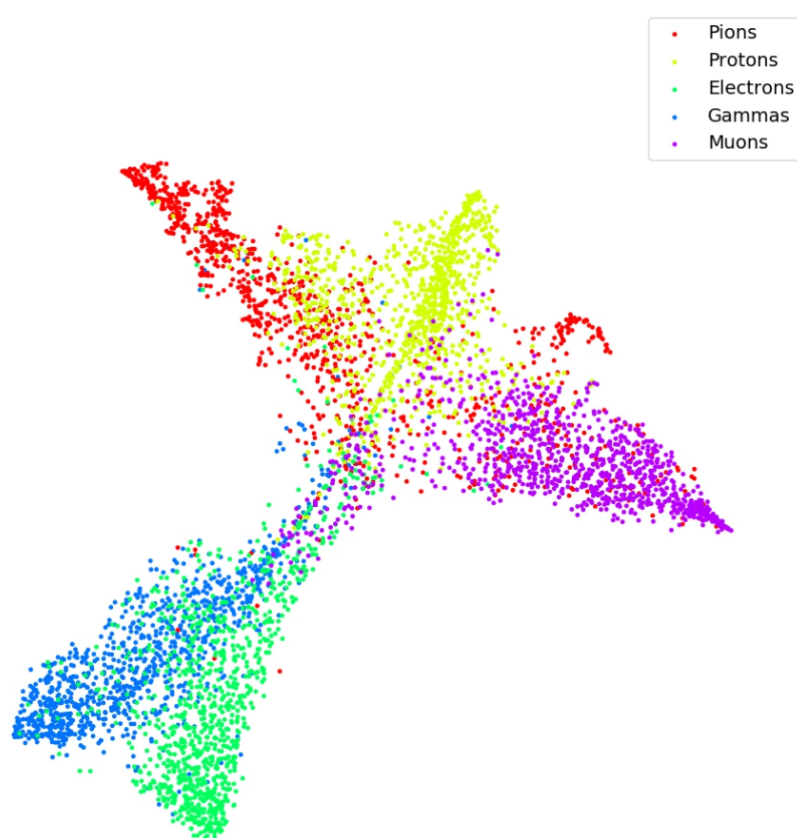


Figure 7.9: t-SNE of CNN

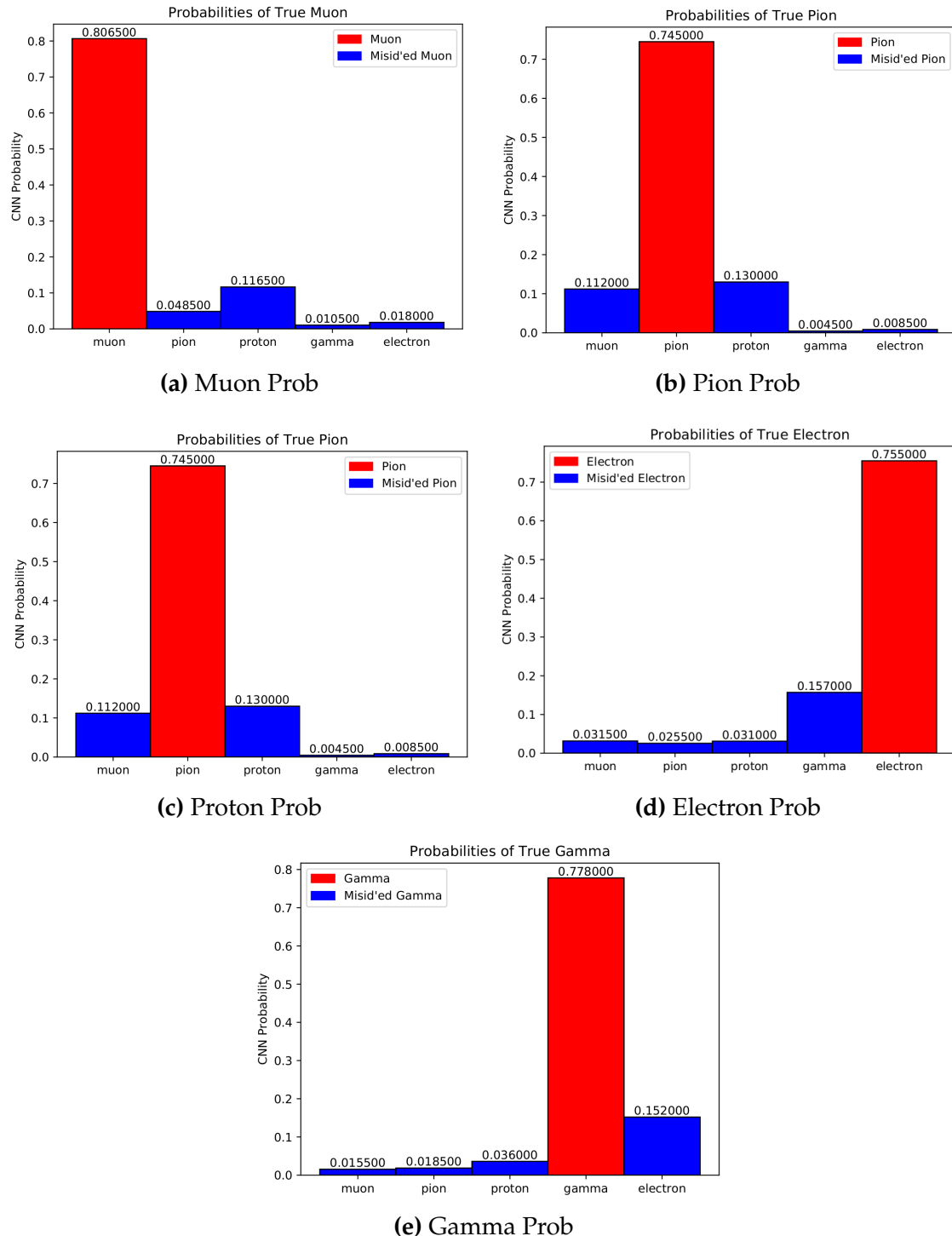


Figure 7.10: Probabilities of different particle classes as well as their contamination from other classes

1664 protons. For pions, both protons and muons get misidentified as pions at around the
1665 same probability. Similar behavior is also seen for proton identification. Electrons and
1666 gammas are misidentified as each-other with similar probabilities.

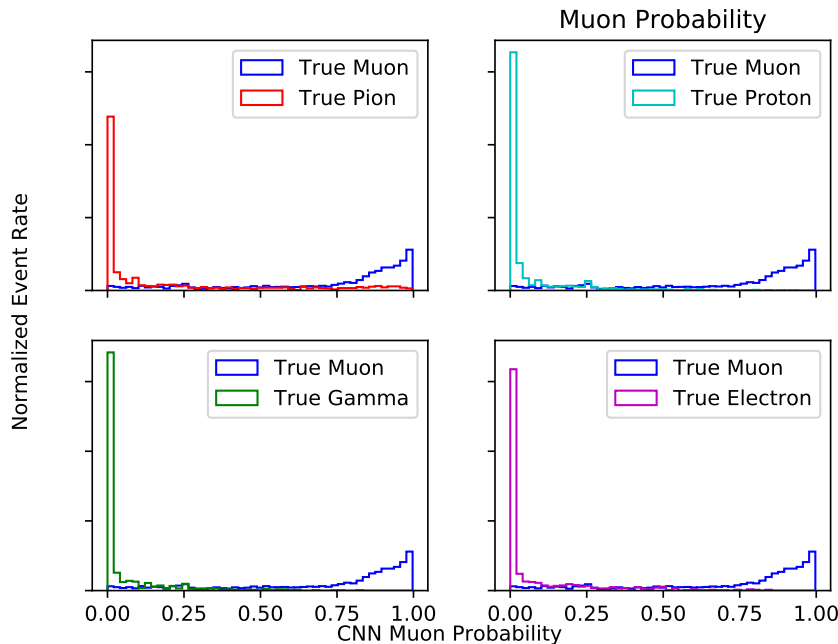
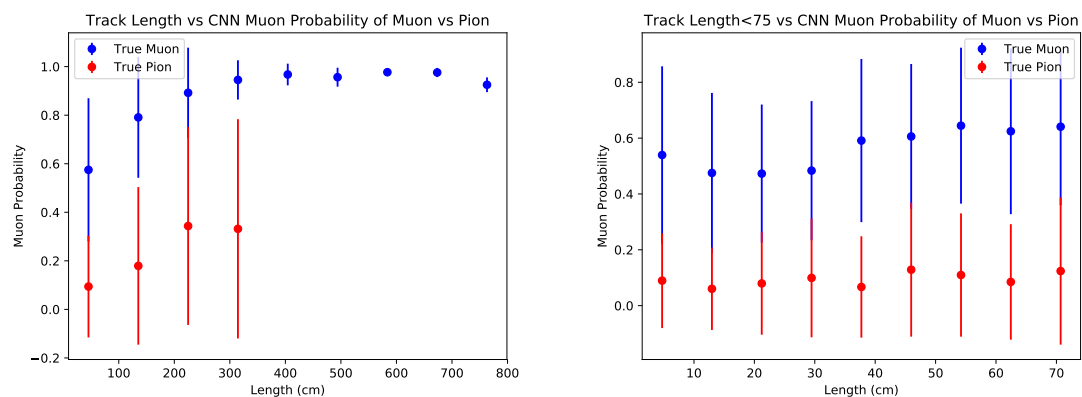


Figure 7.11: Muon probability of true muons (blue) versus pions (red), protons (cyan), gammas (green) and electrons (magenta).

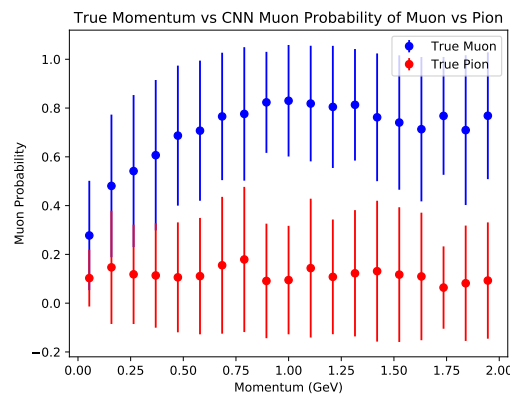
1667 To see what type of background contamination one would be dealing with when
1668 doing muon identification, muon probabilities for each particle class was plotted
1669 against the probability of true muons to see how well muon signal vs other particle
1670 background separation can be done with CNN100000. Figure 7.11 is showing the
1671 true muon probability for true muons, versus the rest of the particle classes. This plot
1672 describes which muon probability value should be chosen for the least amount of
1673 other particle contamination. For electrons and gammas, a muon probability of $\sim 75\%$
1674 would eliminate e/γ contamination. For pions and protons, there is contamination at
1675 all values of muon probability, but the contamination is drastically reduced at a muon
1676 probability $\geq 75\%$.

1677 One of the main concerns with training a neural network was that the features the
1678 network would learn to separate muons from pions would be track range, which is
1679 what was used to begin with in selection I. To make sure that wasn't the case, the next
1680 thing that was looked at was the muon probability versus track range and momentum

of the track. Figures 7.12 through 7.15 show the muon probability in blue for all plots against all other particles. A zoomed in version of track range for all particles was also plotted to make sure there is separation between the particles at low track range. The μ/π separation in track range and momentum is less than for $p/e/\gamma$ but that was to be expected. Although the separation isn't as good as the other particles, there still is separation at low momentum and low track range which cannot be done by using a track range cut like selection I does.

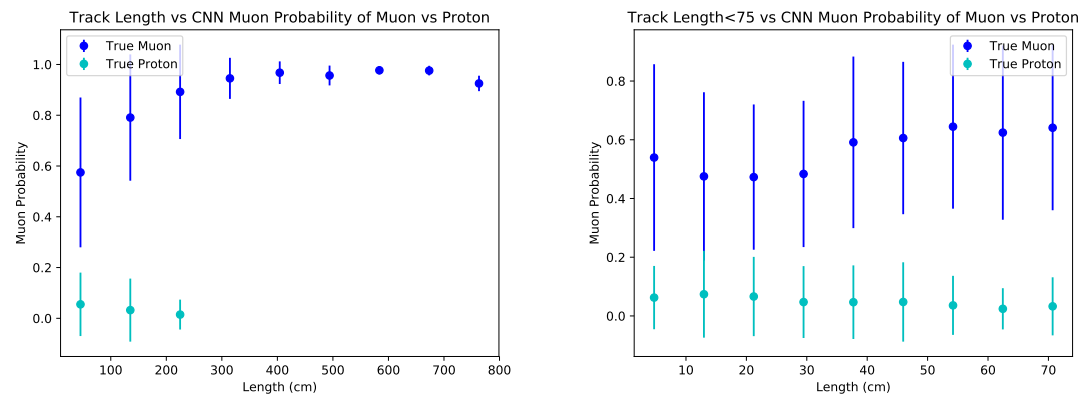


(a) Track range versus muon probability for true muons (blue) and true pions (red). (b) Track range ≤ 75 cm versus muon probability for true muons (blue) and true pions (red).

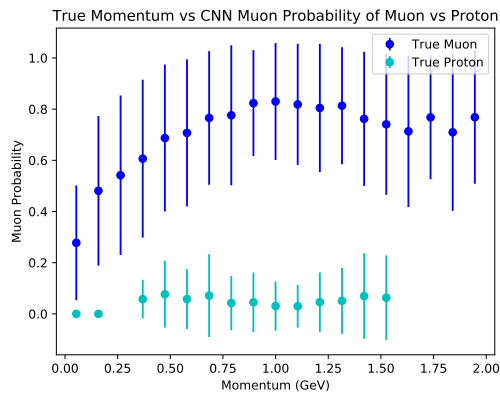


(c) Momentum versus muon probability for true muons (blue) and true pions (red).

Figure 7.12: Kinematic distributions versus muon probability for true muons and true pions.

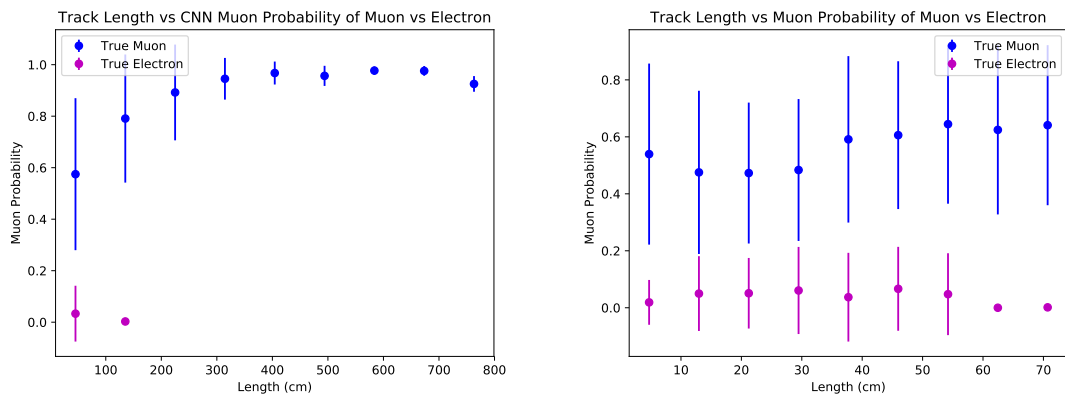


(a) Track range versus muon probability for true muons (blue) and true protons (cyan). (b) Track range ≤ 75 cm versus muon probability for true muons (blue) and true protons (cyan).

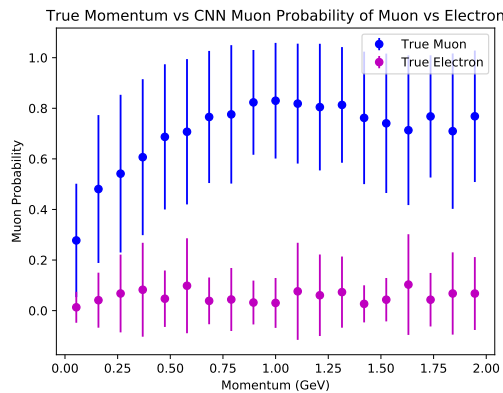


(c) Momentum versus muon probability for true muons (blue) and true protons (cyan).

Figure 7.13: Kinematic distributions versus muon probability for true muons and true protons.



- (a) Track range versus muon probability for true muons (blue) and true electrons (magenta).
- (b) Track range ≤ 75 cm versus muon probability for true muons (blue) and true electrons (magenta).



- (c) Momentum versus muon probability for true muons (blue) and true electrons (magenta).

Figure 7.14: Kinematic distributions versus muon probability for true muons and true electrons.

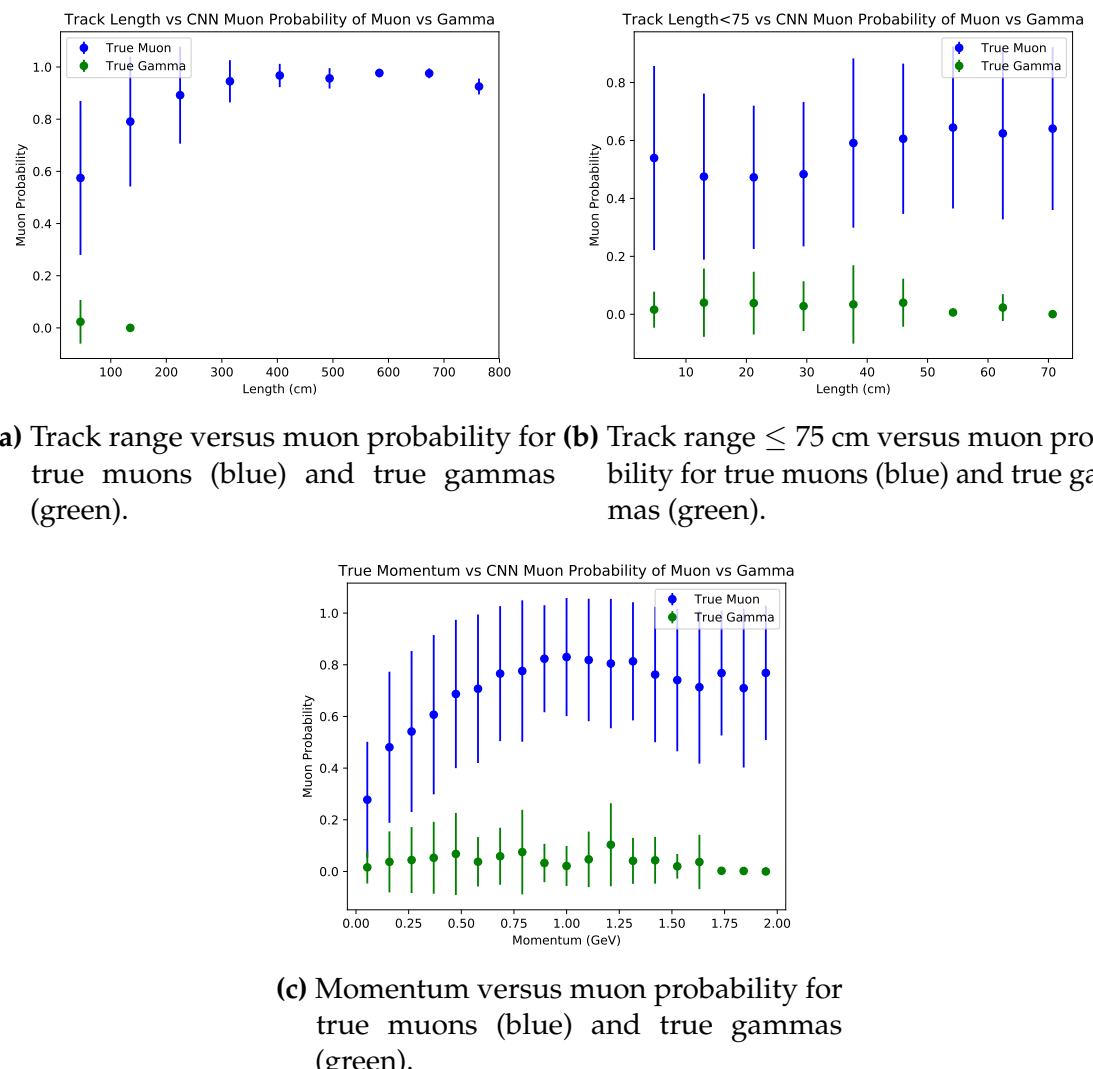


Figure 7.15: Kinematic distributions versus muon probability for true muons and true gammas.

1688 Chapter 8

1689 Using Convolutional Neural Networks 1690 for ν_μ CC event classification

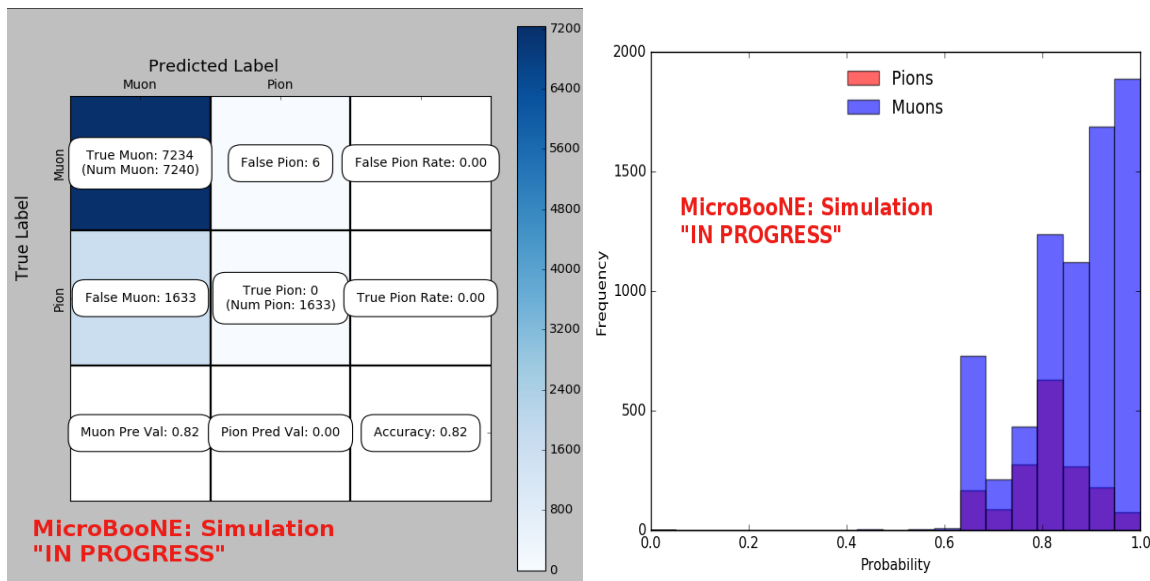
1691 8.1 Classification using CNN10000

1692 8.1.1 Classification of MC data using Selection I CC-Inclusive Filter

1693 After training CNN10000, it was then used to classify track candidate images that
1694 were identified by the selection I cc-inclusive filter described in chapter 5. Passing
1695 rates for each cut in this filter are shown in table 5.1. Out of 188,880 events, 19,112
1696 passed the cut right before the 75 cm track length cut which is a 10.1% passing rate and
1697 comparable to the 10% passing rate shown in table 5.1. In time cosmics were also run
1698 over, out of 14,606 in time cosmics events, 302 passed the cut right before the 75 cm
1699 track length cut which is a 2.1% passing rate comparable to the 2.7% passing rate in the
1700 cc-inclusive tech-note. Figures 8.1a and 8.1b show the accuracy and μ/π separation.
1701 Both plots are only composed of muons and pions due to the focus on μ/π separation
1702 and the fact that CNN10000 was only trained on muons and pions, however, for
1703 reference, all other particles that did pass selection I were mis-id'ed as muons. Muons
1704 are being identified at a very high rate, while pions are all being mis-id'ed as muons.
1705 This is due in part because the pion track candidate that does pass the cc-inclusive
1706 filter right before the 75 cm track length cut has already been identified as a muon
1707 candidate, hence, at a higher muon probability. Another reason for the pion mis'id
1708 can be attributed to the training/classifying dataset difference. For training, the pion
1709 images include the whole pion interaction in argon, including any decays or nucleon
1710 scattering. The image created from a BNB+Cosmic event used for classification only

includes the track candidate that passed the cc-inclusive filter. Figure 8.2a shows the track range distributions of all events from selection I being classified by the CNN as a muon with a probability of 70% regardless of true particle type. We get entries for the CNN curve in the lowest bin and none for the 75 cm curve. To see how many true CC events were identified by CNN10000 breaking down figure 8.2a by event type was necessary. Figures 8.2b and 8.2c show track range distributions separated by signal and various backgrounds. Particle type was not taken into consideration in these plots so true CC event images can be any track candidate particle passing selection I cut right before track length cut including pions and protons.

To gain an even deeper understanding on how CNN10000 is performing, plotting these distributions with only muons and pions was done due to the fact that CNN10000 was trained with only those particles for μ/π separation. Figures 8.2d-8.3d show the stacked histograms of signal and background of the track range distributions with varying CNN probabilities starting from 70% and ending at 90% probability. With higher probabilities we get a purer sample in the lower bin but we end up losing events as well. Momentum distributions for all signal/background events are shown in figure 8.4.



(a) Confusion Matrix for CNN10000 classified events from selection I

(b) Probability plot for CNN10000 classified events from selection I

Figure 8.1: Confusion matrix and probability plot of events passing selection I cc-inclusive cuts right before 75cm track length cut

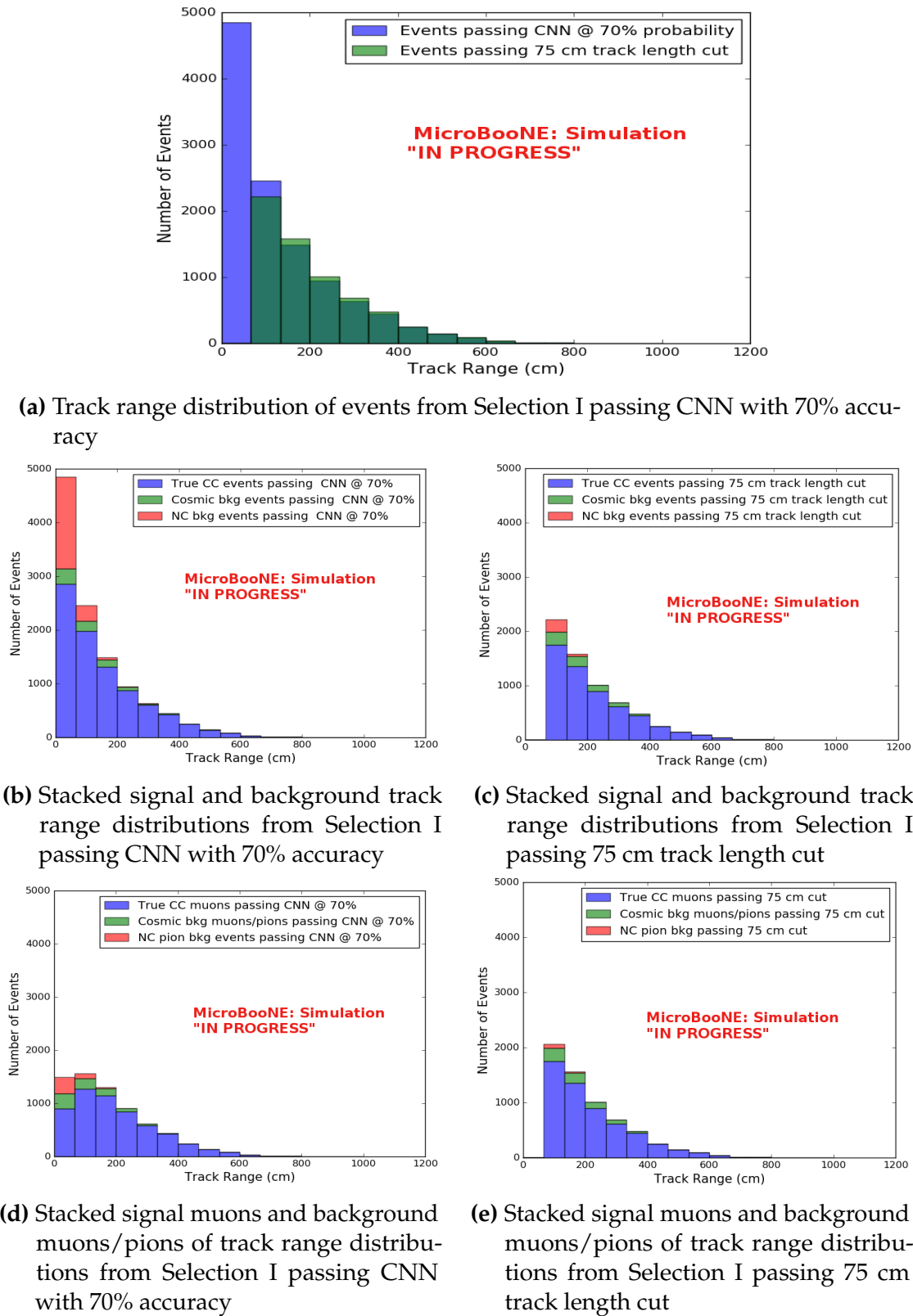


Figure 8.2: CNN10000 distributions of track candidate images output from Selection I cc-inclusive filter

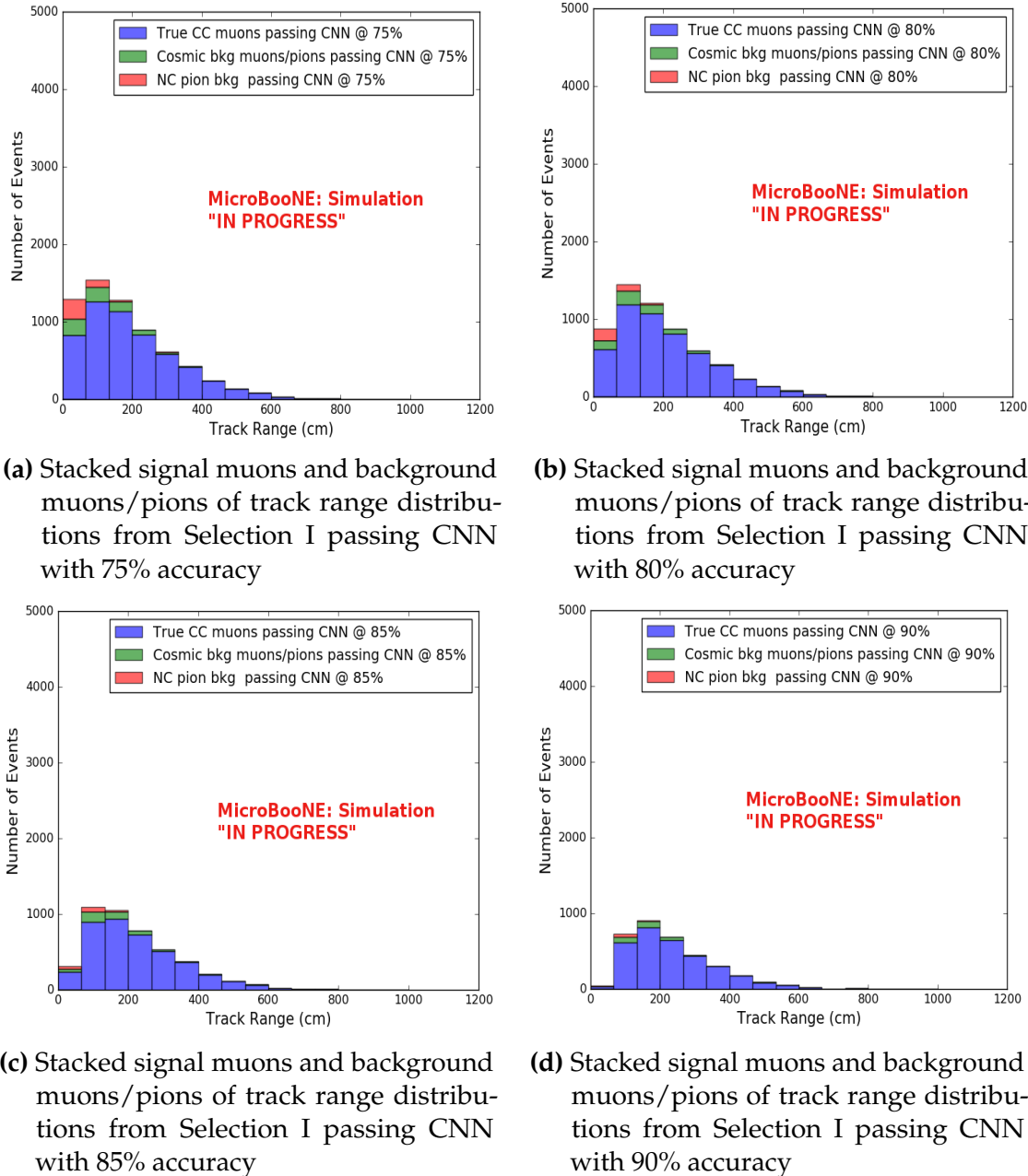
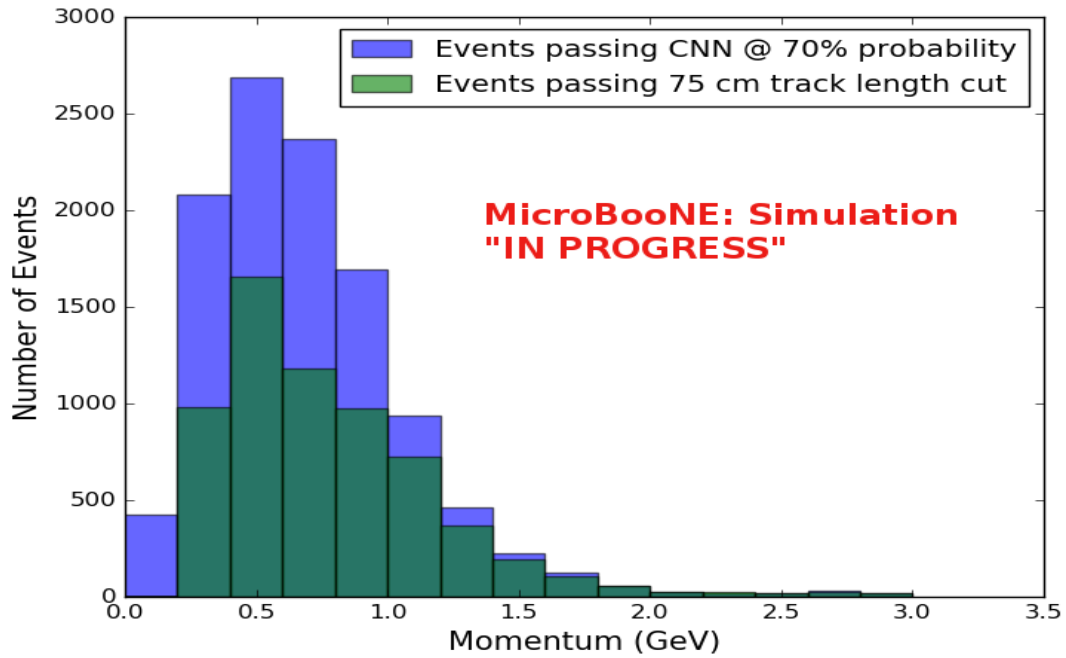
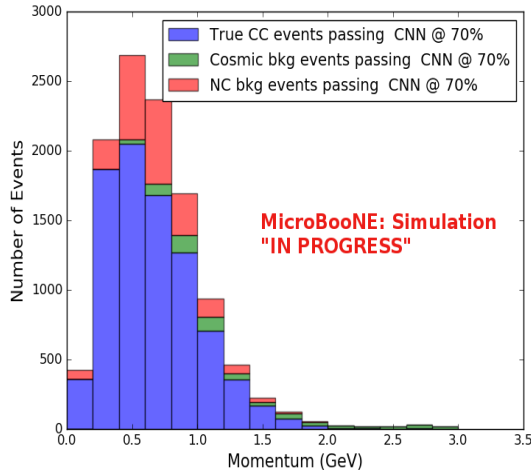


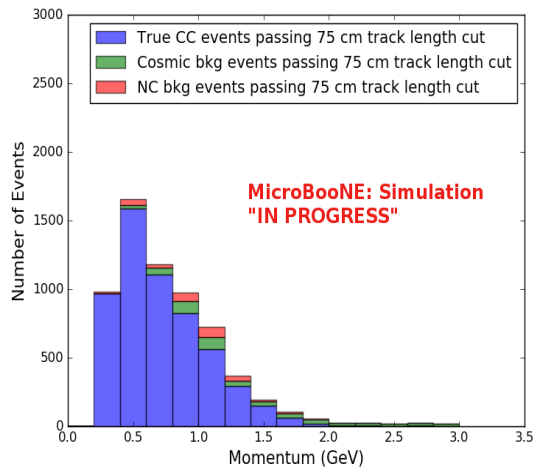
Figure 8.3: CNN10000 stacked signal/background track range distributions of track candidate images output from Selection I cc-inclusive filter



(a) Momentum distribution of events from Selection I passing CNN with 70% accuracy



(b) Stacked signal and background momentum distributions from Selection I passing CNN with 70% accuracy



(c) Stacked signal and background momentum distributions from Selection I passing 75 cm track length cut

Figure 8.4: CNN10000 momentum distributions of track candidate images output from Selection I cc-inclusive filter

Another check was to see if any true CC pions were passing through the cut right before the 75 cm track length cut. Figure 8.5 shows the comparison of the stacked track range distribution with only true CC muon signal versus the stacked distribution with true CC muons and pions signal. As you can see, we gain more events when plotting CC events with a particle type of either muons or pions due to the CNN classifying all pions in this dataset as muons. This is an interesting scenario and a sample of topologies of these images are represented in figure 8.6, at least 3 tracks are coming out of the vertex for these types of events. With the 75 cm track length cut, the selection is cutting event topologies like this where the pion is the tagged track candidate. Figure 8.6a has a defined longer muon track, but because of dead wires through the track, the reconstructed range is 1. less than 75 cm and 2. shorter than the reconstructed pion whose length is also less than 75 cm. This is a very interesting event, but because of issues with the tracking algorithm, the 75 cm cut would get rid of this event. The CNN was able to recover this event only because it has classified all pions as muons. Figure 8.6b shows the second case to think about, the pion, while still less than 75 cm has a reconstructed track length longer than the muon. Again, the CNN recovered this event due to pions being classified as muons. Lastly, figure 8.6c shows a pion with a reconstructed track length greater than 75 cm and the muon. These three cases show that a broader question must be asked when training the network other than is it a muon or pion. There are different routes to recover interesting events like these. One route is to ask the network “Is it a CC event or is it an NC event?” and obtain an image dataset consisting of whole CC/NC events that will train the network to answer this question. The other route is to ask the network “Is this a $\mu/\pi/p/$ from a CC event or NC event and obtain an image dataset consisting of primary particles from a CC/NC event. Both these paths will be explored in future work.

Table 8.1 shows the passing rates for the 75 cm track length cut and the CNN cut at 70% and 83%. The passing rates at the track containment level for the 75 cm track length cut compared to the CNN are comparable with only a 0.6% difference in the in time cosmic bin which may be due in part to the larger in time cosmic statistics used for the CNN dataset. These passing rates need to be comparable to then be able to compare the passing rates after the CNN cut to the 75 cm cut. Again, the same BNB+Cosmic sample was used for both selection I with 75 cm cut and selection I with CNN cut. As it stands, a CNN cut at 83% probability has a MC true CC event passing rate of 14% compared to the 13% passing rate of the 75 cm track length cut. The Signal:Cosmic Only background is also reduced from 1:0.6 to 1:0.4. The total passing rate is also higher than the 75 cm cut, 3.6% vs 4.0%. Table 8.2 shows the breakdown

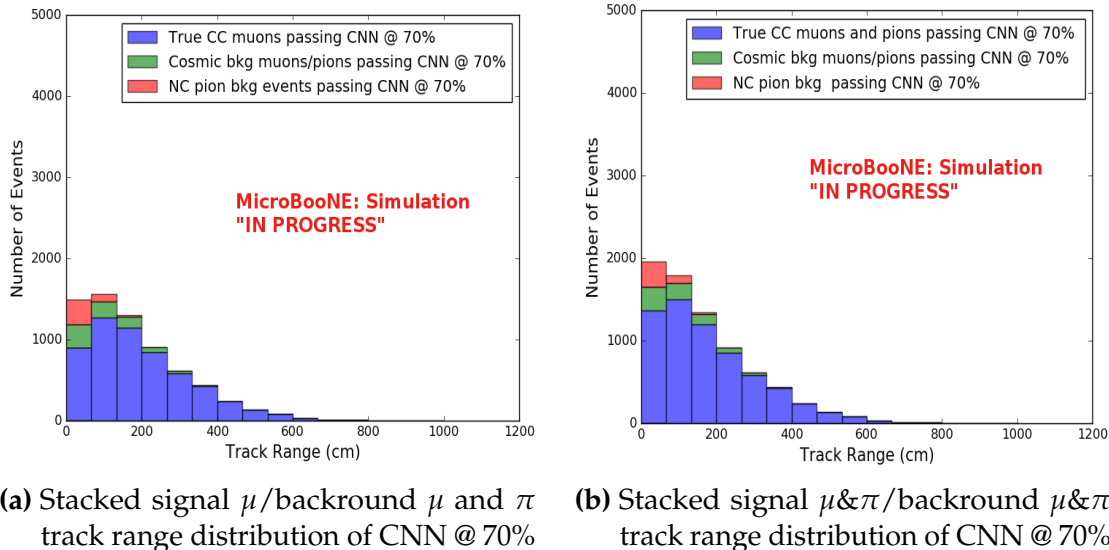


Figure 8.5: Track distribution comparisons of true CC muons plotted vs true CC muons and pions plotted

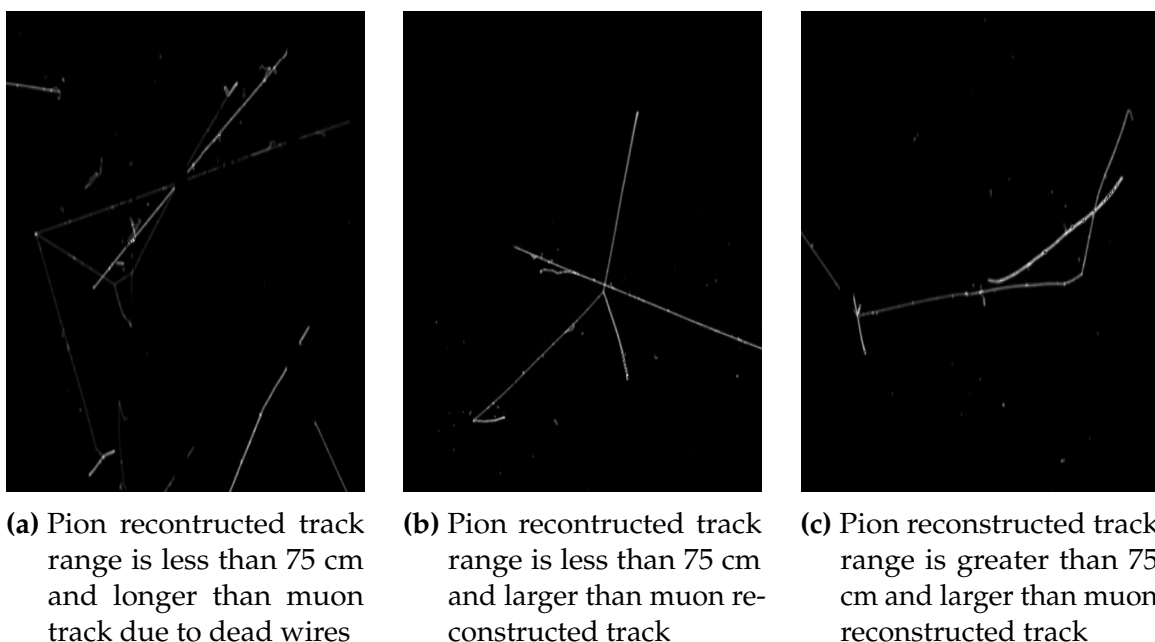


Figure 8.6: Images of true CC events where the pion was the tagged track candidate

		BNB + Cosmics		Cosmic Only	Signal: Cosmic Only
		Selection	MC Truth		
75 cm Cut passing rates	Generated Events	191362	45723	4804	1:22
	Track Containment	19391 (48%/10%)	11693 (45%/26%)	129 (38%/2.7%)	1:2.3
	track \geq 75 cm	6920 (36%/3.6%)	5780 (49%/13%)	17 (13%/0.4%)	1:0.6
CNN passing rates	Generated Events	188880	44689	14606	1:21
	Track Containment	19112 (/10%)	11554 (/26%)	302 (/2.1%)	1:1.73
	CNN cut @ 70% Probability	16502 (86%/8.7%)	10605 (92%/23%)	205 (68%/14%)	1:1.28
	CNN cut @ 83% Probability	7511 (46%/4.0%)	6142 (58%/14%)	32 (16%/0.2%)	1:0.4

Table 8.1: Comparing passing rates of CNN at different probabilities versus 75 cm track length cut: Numbers are absolute event counts and Cosmic background is not scaled appropriately. The BNB+Cosmic sample contains all events. The numbers in brackets give the passing rate wrt the step before (first percentage) and wrt the generated events (second percentage). In the BNB+Cosmic MC Truth column shows how many true ν_μ CC-inclusive events (in FV) are left in the sample. This number includes possible mis-identifications where a cosmic track is picked by the selection instead of the neutrino interaction in the same event. The CNN MC True generated events were scaled wrt the MC True generated events for the 75 cm cut passing rates due to only running over 188,880 generated events versus the 191362 generated events. The last column Signal:Cosmic only gives an estimate of the ν_μ CC events wrt the cosmic only background at each step. For this number, the cosmic background has been scaled as described in [?]. Note that these numbers are not a purity, since other backgrounds can't be determined at this step.

Signal	ν_μ CC events with true vertex in FV	#Events(Fraction)	#Events(Fraction)
		passing Sel I	passing CNN @ 83% Probability
		1168(53.8%)	6142(61%)
Backgrounds	Cosmics Only Events	725(33.4%)	2582(26%)
	Cosmics in BNB Events	144(6.6%)	492(4.9%)
	NC Events	75(3.5%)	778(7.7%)
	ν_e and $\bar{\nu}_e$ Events	4(0.2%)	32(0.3%)
	$\bar{\nu}_\mu$ Events	40(1.8%)	67(0.7%)

Table 8.2: Signal and background event numbers of selection I and selection I with CNN cut estimated from a BNB+Cosmic sample and Cosmic only sample normalized to $5 * 10^{19}$ PoT. The last column gives the fraction of this signal or background type to the total selected events per CNN probability.

¹⁷⁶⁴ of signal and backgrounds for the CNN at the different probabilities. We have a 61%
¹⁷⁶⁵ signal passing rate with the CNN cut @ 83% versus the 53.8% signal passing rate of
¹⁷⁶⁶ the 75 cm cut.

¹⁷⁶⁷ Based on these numbers, the following performance values of the selection with 75
¹⁷⁶⁸ cm cut versus selection with CNN @ 83% probability cut were calculated:

- ¹⁷⁶⁹ • Efficiency: Number of selected true ν_μ CC events divided by the number of
¹⁷⁷⁰ expected true ν_μ CC events with interaction in the FV.
 - ¹⁷⁷¹ – Selection I: 12.3%
 - ¹⁷⁷² – Selection I with CNN10000 cut @ 83% probability: 14%
- ¹⁷⁷³ • Purity: Number of selected true ν_μ CC events divided by sum of itself and the
¹⁷⁷⁴ number of all backgrounds.
 - ¹⁷⁷⁵ – Selection I: 53.8%
 - ¹⁷⁷⁶ – Selection I with CNN10000 cut @ 83% probability: 61%

¹⁷⁷⁷ Lastly, figure 8.7 shows a more representative performance of the CNN. Due to the
¹⁷⁷⁸ fact that the CNN was trained on muons and pions, showing the performance of CC
¹⁷⁷⁹ muon events versus NC pion events with respect to CNN probability gives a better
¹⁷⁸⁰ picture of how the network is performing. Figure 8.7 shows that at 83% we are below
¹⁷⁸¹ the 75 cm cut NC pion threshold and still above the CC muon threshold. Using 83%
¹⁷⁸² probability not only reduced the NC pion background, it also dramatically reduced
¹⁷⁸³ the in time cosmics and cosmics in the BNB.

¹⁷⁸⁴ 8.1.2 Conclusions of CNN10000 classification of MC data

¹⁷⁸⁵ It was shown that even though CNN10000 was trained with single particle generated
¹⁷⁸⁶ muons and pions, it performs fairly well at classifying track candidate images from
¹⁷⁸⁷ BNB+Cosmic events. Events have been regained below the 75 cm track length cut and
¹⁷⁸⁸ the momentum and track range distributions have similar shapes to the distributions
¹⁷⁸⁹ of Selection I. Efficiencies and purities were calculated for selection I events before 75
¹⁷⁹⁰ cm track length cut with the CNN at 83% probability and are 14% and 62% respectively.
¹⁷⁹¹ Although the CNN doesn't have separation between muons and pions and although
¹⁷⁹² all particles passing CNN are classified as muon, increasing CNN probability allows
¹⁷⁹³ us to increase the purity as well as maintain an efficiency comparable to the 75 cm track

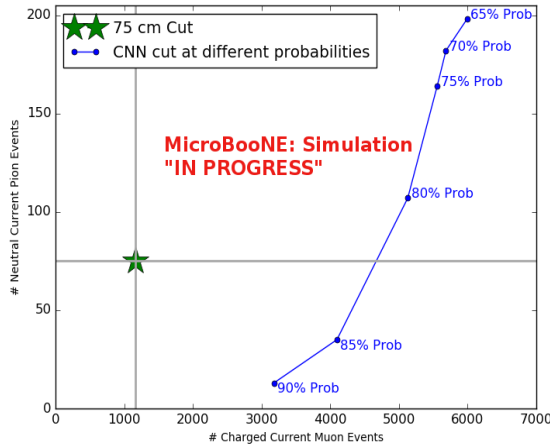


Figure 8.7: CNN performance of classified muons and pions compared to the already implemented 75 cm track length cut

length cut all while recovering events below that 75 cm cut. Out of the 6142 events that passed the CNN @ 83% 1470 events were below the 75 cm cut, a recovery of 3.3% of data with an purity of 15%. Although these numbers are low, it is an improvement from the selection I in both total efficiency and purity and an increase in phase space by recovering these events.

8.2 Classification using CNN100000

For classification of BNB+Cosmics and data using CNN100000, images were made from track candidates that passed the Selection I filter, however, unlike for classifying BNB+Cosmics using CNN10000, the classification of CNN100000 went further up Selection I's cut chain. For CNN100000, steps 5 through 8 seen in section 5.5 were removed. The image making algorithm would then create multiple images per event of pixels corresponding to each track associated to the flattest vertex candidate in the fiducial volume. One of the findings of CNN10000 was the possibility of recovering interesting events in which a pion from a cc-inclusive event is tagged as the track candidate of interest. This was the reason for trying to expand on what a convolutional neural network could accomplish. By allowing the CNN to particle ID all track associated with the vertex candidate, we allow the selection to contain the interesting events that were cut out in selection I due to the cc pion track being chosen as the track candidate. Figure 8.8 shows the image making algorithm for BNB+Cosmic images.

1813 The results of using CNN100000 to classify BNB+Cosmics will be discussed in the next
1814 sections.

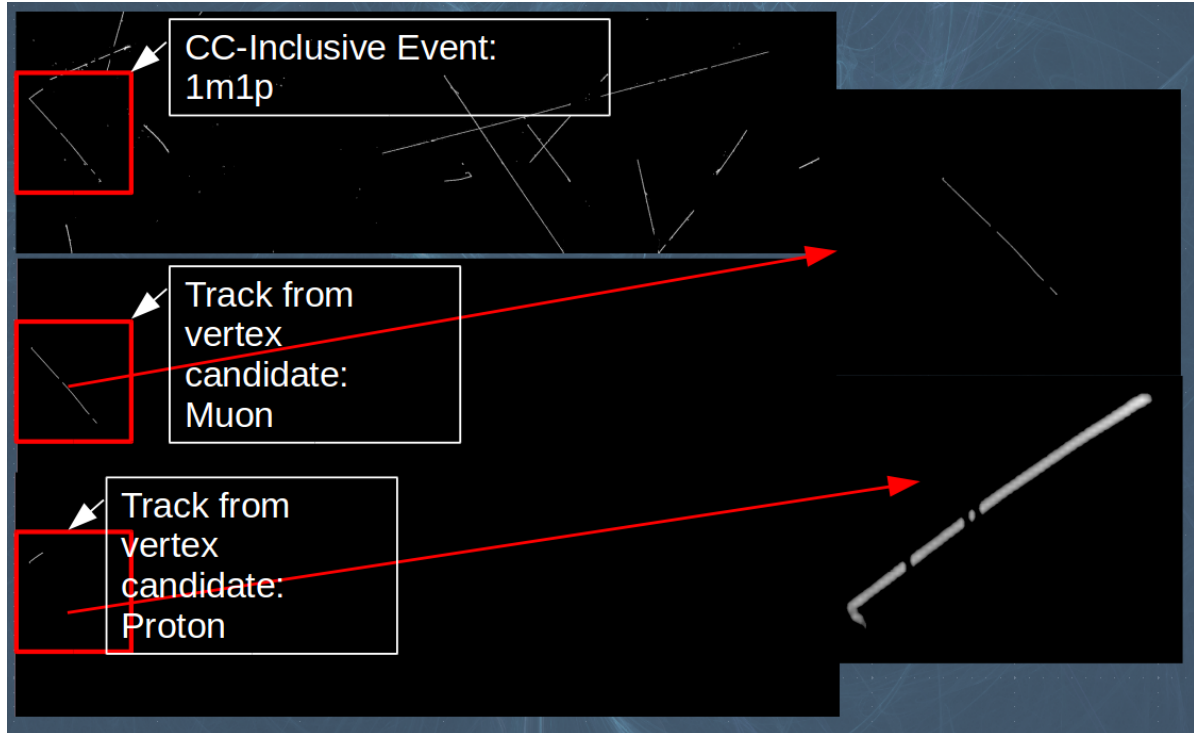


Figure 8.8: Image making steps used for classifying BNB+Cosmic events using CNN100000

1815 8.2.1 Classification of MC data using Selection I CC-Inclusive Filter

1816 After classifying all BNB+Cosmic and in time cosmic events, an efficiency vs purity
1817 curve was created for various muon probabilities to choose a probability that would
1818 increase both efficiency and purity of Selection I. This is shown in figure 8.9. Selection I
1819 and Selection II are also shown on this curve. At 85% probability, both the efficiency
1820 and purity is better than both Selection I and Selection II therefore is the chosen muon
1821 probability.

1822 Kinematic truth distributions of BNB+Cosmic events passing Selection 1823 I+CNN10000

1824 To classify cc-inclusive events, all images of a certain event were id'ed using CNN100000,
1825 if one image in an event was classified as a muon, that event would then be classified

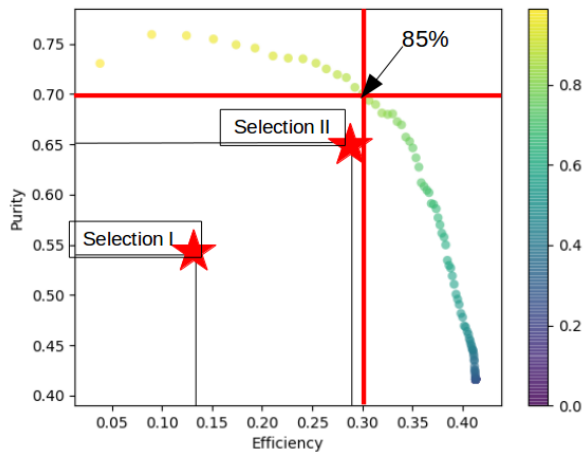


Figure 8.9: Efficiency vs Purity curve for various CNN100000 muon probabilities. At 85% muon probability, the efficiency is 30% and the purity is 70%

as a cc-inclusive event. If after running over all images in an event and none were id'd as a muon, that event would then be classified as background. Figure 8.10 are the true kinematic distributions for the true cc-inclusive events that passed the CNN100000 (blue) at 85% muon probability as well as the cc-inclusive events that passed the selection I filter (red).

The shapes of the true kinematic distributions are mostly comparable for CNN100000 and Selection I, however the CNN100000 curve has more events passing at muon probability 85% compared to the Selection I filter. This is due to the removal of the containment cut. You can also see entries for cc-inclusive events at the lowest track range bin for CNN100000 that isn't there for the Selection I filter. Although the muon probability is high, we are still able to recover events with low track candidate track range. Another thing to note in the track range plot is that the peak for CNN100000 is shifted to a higher track range compared to Selection I. This peak shift can also be seen in the momentum distribution plot. Again, a hypothesis for this shift is due to the lack of containment for the tracks, this has been explored and will be discussed.

Figures 8.11 through 8.14 compare the stacked event type distributions between the Selection I filter and the CNN100000. The percentage of CCQE events that passed Selection I is 51% compared to 62% for CNN100000. For CCRES, Selection I had a passing rate of 37% compared to 29% for CNN100000. The CCDIS passing rate was 11% and 9% for Selection I and CNN100000 respectively. Lastly, the CCCOH rate was 1% and 0.9% for Selection I and CNN100000 respectively. A larger percentage of CCQE

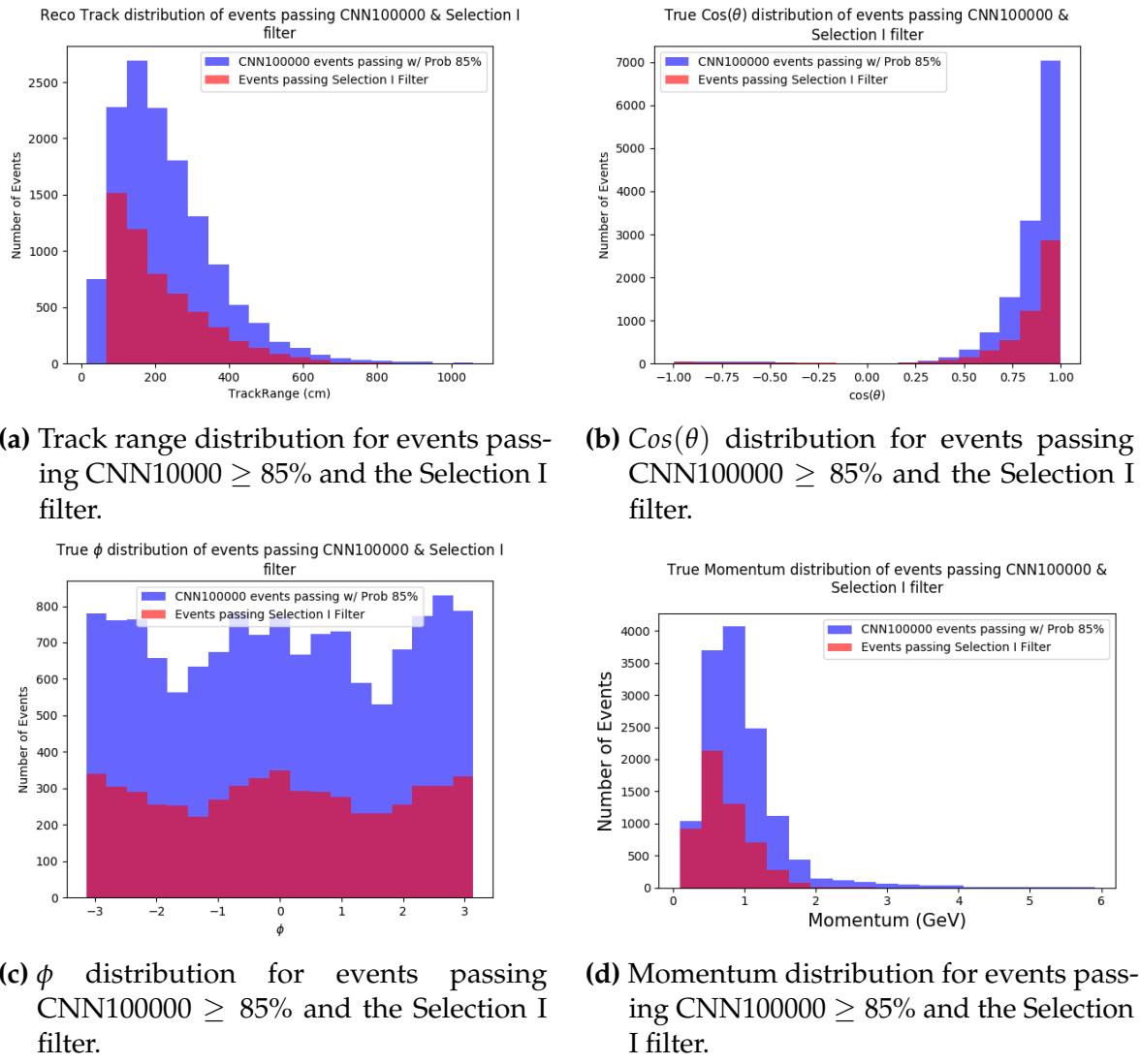


Figure 8.10: Truth kinematic distributions of events passing CNN100000 and Selection I. The red corresponds to the Selection I passing events and blue to the CNN100000 passing events.

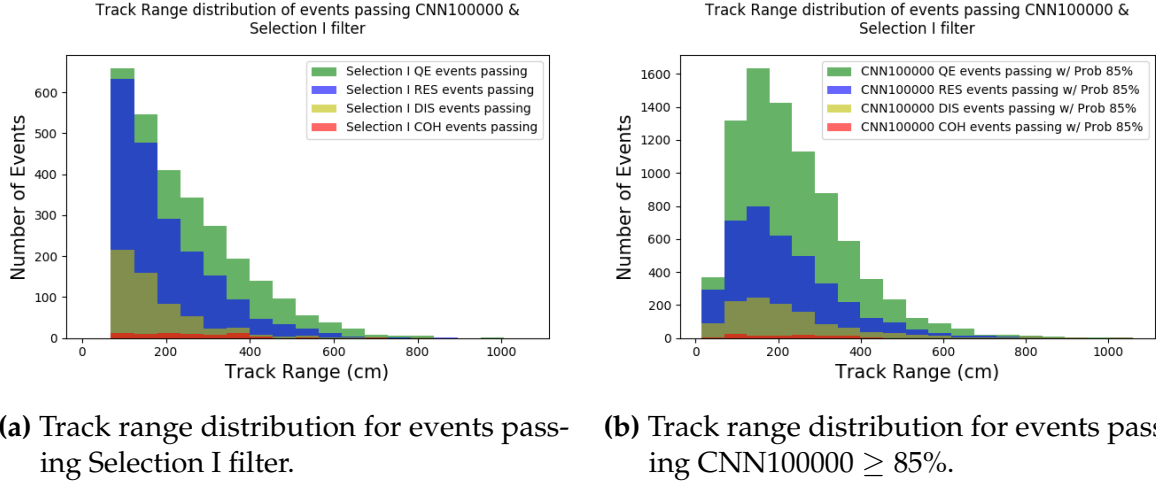


Figure 8.11: Truth stacked event type track range distribution of events passing Selection I (left) and CNN100000 (right). Different event types are CCQE (green), CCRES (blue), CCDIS (yellow), CCCOH (red).

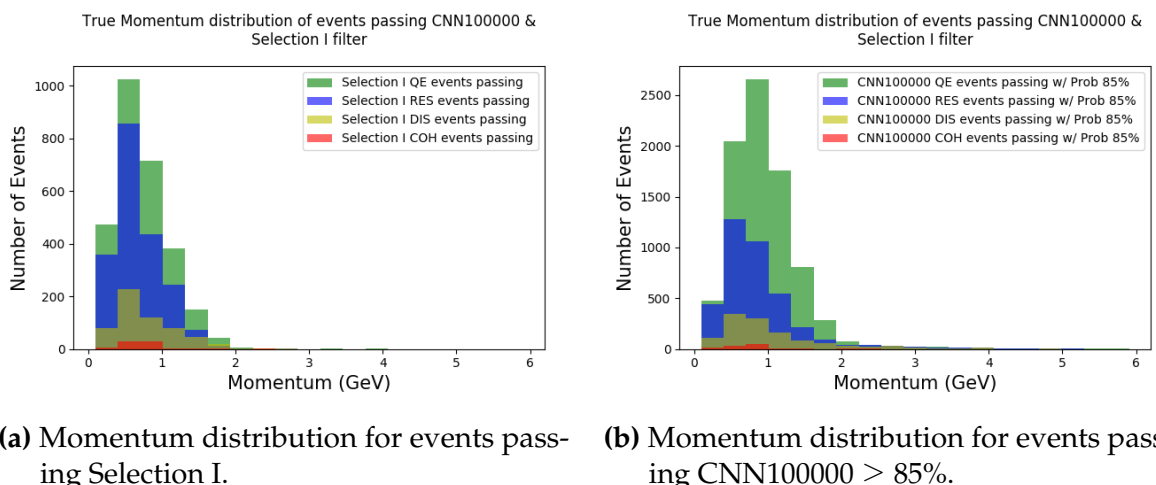


Figure 8.12: Truth stacked event type momentum distribution of events passing Selection I (left) and CNN100000 (right). Different event types are CCQE (green), CCRES (blue), CCDIS (yellow), CCCOH (red).

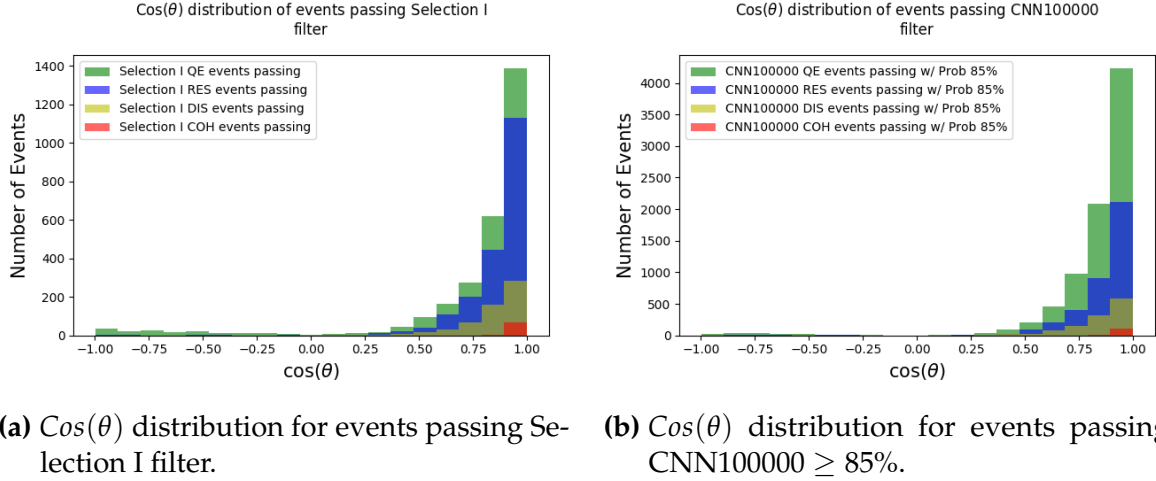


Figure 8.13: Truth stacked event type $\cos(\theta)$ distribution of events passing Selection I (left) and CNN100000 (right). Different event types are CCQE (green), CCRES (blue), CCDIS (yellow), CCCOH (red).

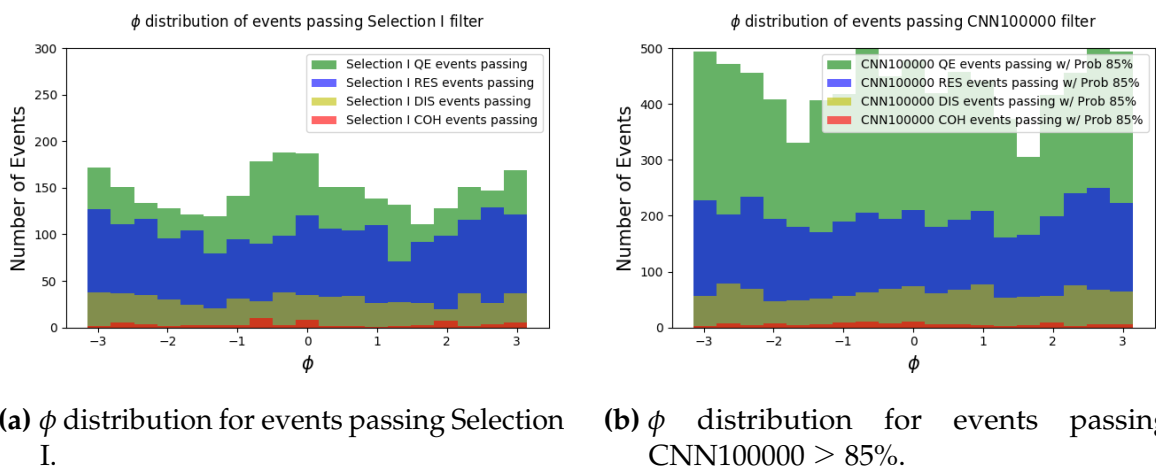


Figure 8.14: Truth stacked event type phi distribution of events passing Selection I (left) and CNN100000 (right). Different event types are CCQE (green), CCRES (blue), CCDIS (yellow), CCCOH (red).

¹⁸⁴⁷ events are passing the CNN100000 compared to Selection I, an increase of 9%. CCQE
¹⁸⁴⁸ is the dominant interaction for ν_μ events with neutrino energy < 1 GeV, so being able
¹⁸⁴⁹ to recover events below the 75 cm track range cut may be the reason for the increase in
¹⁸⁵⁰ CCQE events.

¹⁸⁵¹ Figure 8.15 shows the vertex positions for the true cc-inclusive events passing the
¹⁸⁵² CNN100000 (blue) and the Selection I (red) filter. Again, the shape distributions are
¹⁸⁵³ comparable among the two selections other than a higher passing rate due to the lack
¹⁸⁵⁴ of track containment for CNN100000.

¹⁸⁵⁵ **8.2.2 Classification of MicroBooNE data using Selection I**
¹⁸⁵⁶ **CC-Inclusive Filter**

¹⁸⁵⁷ **8.2.3 Comparing two CC-Inclusive Cross Section Selection Filters**

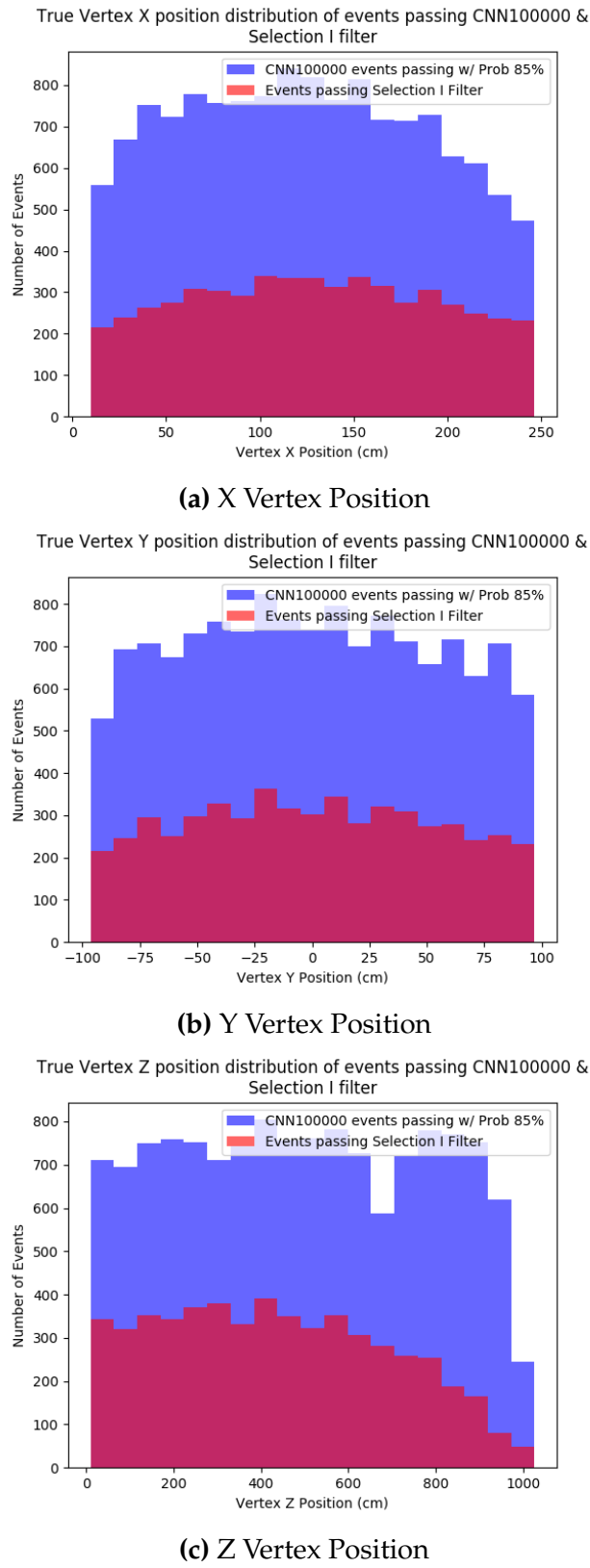


Figure 8.15: Vertex position for X, Y and Z of true cc-inclusive events passing CNN100000 and Selection I

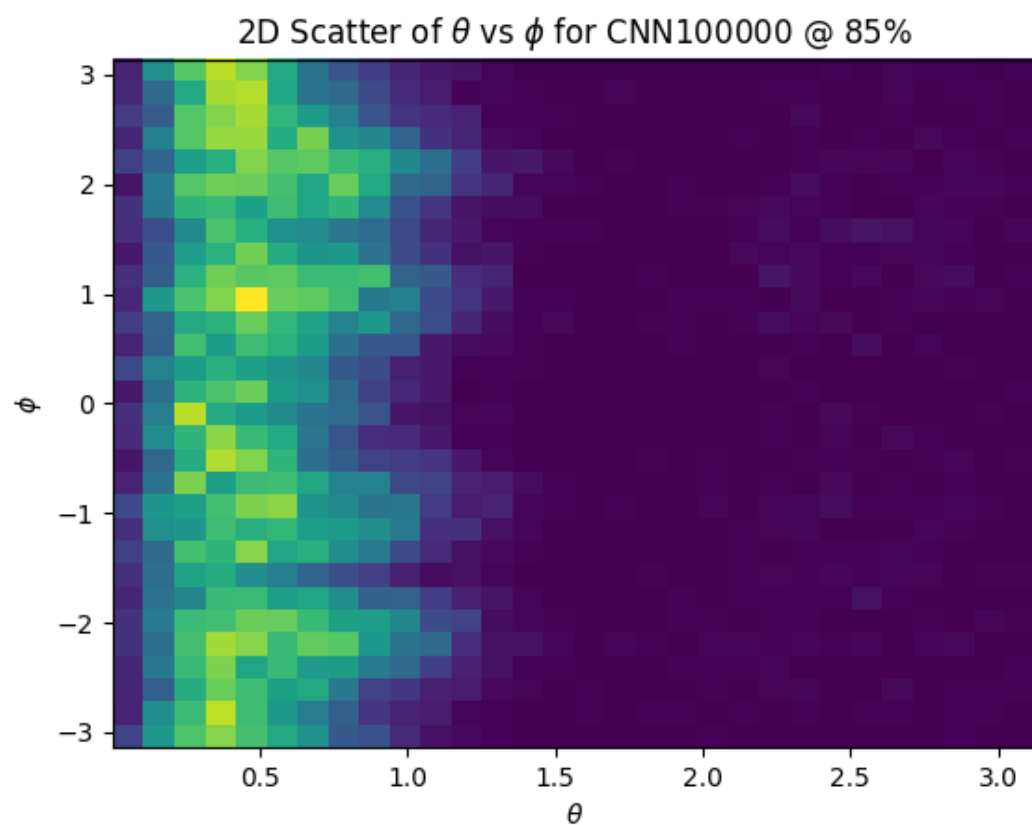


Figure 8.16: $\cos(\theta)$ distribution at $\text{CNN10000} \geq 85\%$

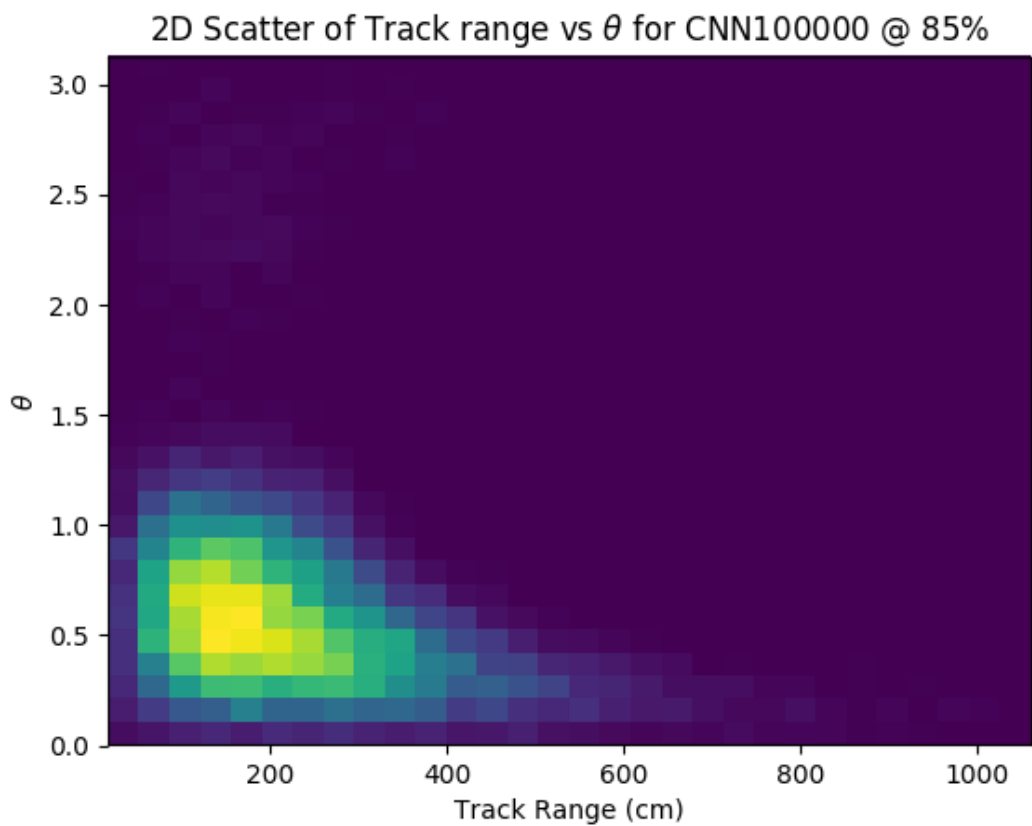


Figure 8.17: $\text{Cos}(\theta)$ distribution at $\text{CNN10000} \geq 85\%$

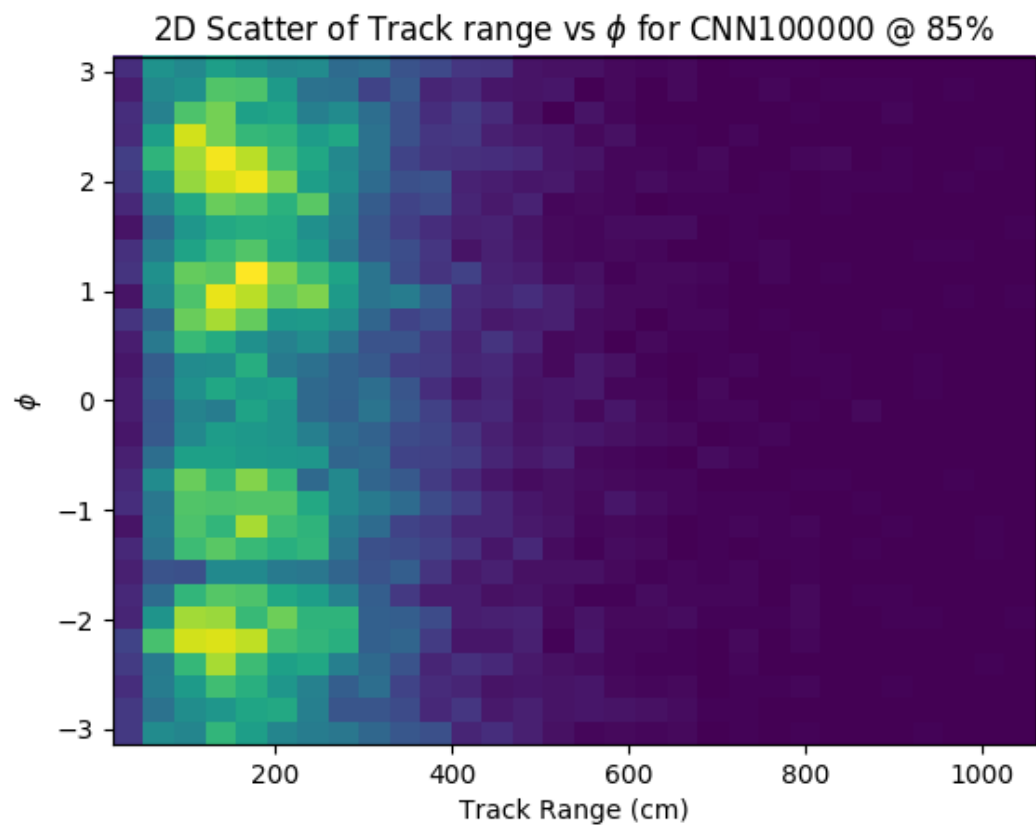


Figure 8.18: $\text{Cos}(\theta)$ distribution at $\text{CNN10000} \geq 85\%$

¹⁸⁵⁸ **Chapter 9**

¹⁸⁵⁹ **Conclusion**

¹⁸⁶⁰ Your Conclusions here.

¹⁸⁶¹

¹⁸⁶² Bibliography

- ¹⁸⁶³ [1] Wikipedia, Neutrino, <http://wikipedia.org/wiki/Neutrino>, 2013.
- ¹⁸⁶⁴ [2] Wikipedia, Neutrino oscillation, http://en.wikipedia.org/wiki/Neutrino_oscillation, 2013.
- ¹⁸⁶⁵
- ¹⁸⁶⁶ [3] B. N. Laboratory, Neutrinos and nuclear chemistry, <http://www.chemistry.bnl.gov/sciandtech/sn/default.htm>, 2010.
- ¹⁸⁶⁷
- ¹⁸⁶⁸ [4] K. Heeger, Big world of small neutrinos, <http://conferences.fnal.gov/lp2003/forthepublic/neutrinos/>.
- ¹⁸⁶⁹
- ¹⁸⁷⁰ [5] A. Y. Smirnov, p. 23 (2003), hep-ph/0305106.
- ¹⁸⁷¹ [6] The MicroBooNE Collaboration, R. e. a. Acciari, (2015), arXiv:1512.06148.
- ¹⁸⁷² [7] The MicroBooNE Collaboration, R. e. a. Acciari, (2016), arXiv:1705.07341.
- ¹⁸⁷³ [8] The MicroBooNE Collaboration, R. e. a. Acciari, (2017), arXiv:1704.02927.
- ¹⁸⁷⁴ [9] The MicroBooNE Collaboration, R. e. a. Acciari, JINST **12** (2017).